Kerstin Hummer

On the Electro-optical Properties of Oligo-acenes

An Ab-initio Study

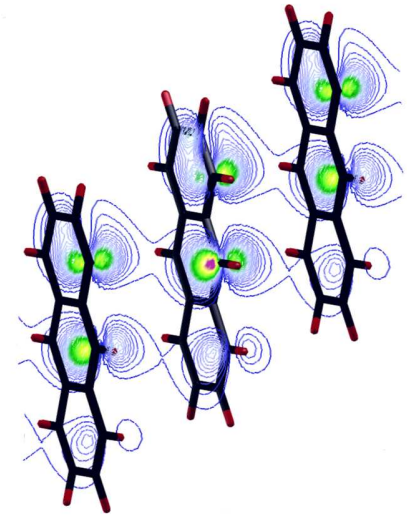

DISSERTATION

written at the Institute of Theoretical Physics
submitted to the Faculty of Natural Sciences
Karl–Franzens–Universität Graz

under supervision of
ao. Univ.–Prof. Dr. Dr. h.c. C. Ambrosch–Draxl

Graz, November 2003

Title page:
2D crystalline charge density of anthracene depicted as isolines. The plot has been generated with XCrySDen [1].

To Jürgen

Discovery is seeing what everyone sees and thinking what no one has thought.

Albert Szent-Györgyi

Preface

The research work presented in this thesis has been accomplished during the years 2001-2003 in the solid state physics group of Prof. C. Ambrosch-Draxl at the Institute of Theoretical Physics, Karl-Franzens-University of Graz. Until mid December 2002 I have been involved in the collaborative project with Prof. Roland Resel's group at the Graz University of Technology for the combined experimental and theoretical investigation of the physical properties of electro-optically active organic materials under high pressure. This cooperation enabled the pressure study of the structural and electronic properties of anthracene, in particular, the importance of the intermolecular interactions present in the crystal. Up to the final stage of this work I have been employed at the University of Graz and focused on the optical properties of naphthalene, anthracene, tetracene and pentacene, which are the first four members of the oligo-acene family.

During my scientific studies I have been supported by many persons in different ways. I would like to thank all of them, particularly I am sincerely grateful to:

Claudia Ambrosch-Draxl, my supervisor for giving me the opportunity to work in her excellent research group, for her guidance and her efforts to acquire additional project money and thus enabling my PhD studies in Graz. Furthermore, she takes care of such a pleasant atmosphere in her group, so that it has been much easier for me to leave behind my husband and our home during the weeks over the past 3 years.

co-workers from the TU Graz: Roland Resel, Georg Heimel, and Martin Oehzelt for their collaboration and providing the experimental data prior to publication, which have been essential for a major part of this work. I particularly acknowledge the creative discussions with Georg and Martin that resulted in many useful ideas.

Jürgen, my husband. My deepest gratitude goes to him for his understanding of my attempts to attain a PhD in Graz and accepting our nomadic life since I worked in Graz. In particular, his confidence has highly encouraged me to work in natural sciences research. Besides, he patiently

keeps his ears open to my reports on research results as well as problems and he always manages it to let me temporary forget these problems at least during our shared weekends.

August & Gertrude, my parents, for supporting me during all the years of my studies and encouraging me to accomplish what I wish to do.

Lisa Maria, Florian, and Michael, my sister and brothers, for reminding me from time to time, that solid state physics is not the only important thing in life and for many exciting and funny weekends in my family.

Alfred & Margareta, my parents-in-law for all the relaxing weekends we have spent together. Margareta serves homemade delicious *Fischlaberl* and Alfred the excellent schnapps afterwards.

Sandra & Peter, my friends in Graz. They are making Graz for me not only a working place, but also a living place. I really enjoyed the evening we spent together watching movies, playing games, listening to Jazz, having pizza at Girardi-Keller, etc. In particular, I want to thank Peter for his computational support, fruitful discussions, his meaningful interpretations and helpfully providing all his useful FORTRAN and MATHEMATICA programs.

Joachim for *selling* me to Claudia's group in Graz, although he never was payed!

all the group members, who are responsible for the enjoyable climate in the working group too and for the amusing tea (coffee) and lunch breaks.

Finally, I kindly acknowledge the financial support indispensable for this thesis by the following institutions:

- Fonds zur Förderung Wissenschaftlicher Forschung (FWF)
  Projects P14237, P14004, and P16227, Vienna, Austria
- European Union
  EU Research and Training Network *EXCiT!NG*
  contract number HPRN-CT-2002-00317, Brussels, Belgium
- Karl-Franzens-University of Graz, Austria

Graz, November 2003 Kerstin Hummer

Contents

1 Introduction 1
1.1 Overview . . . 1
1.2 Motivation . . . 2
1.3 Aims . . . 3
1.4 Outline . . . 4

I Theoretical Toolbox 7

2 Density Functional Theory 9
2.1 Key Concepts of DFT . . . 10
2.2 Approximations for the xc Energy Functional . . . 12
2.2.1 The Local Density Approximation (LDA) . . . 12
2.2.2 The Generalized Gradient Approximation (GGA) . . . 13
2.3 Limitations of the LDA and the GGA . . . 14
2.3.1 Applicability for molecular crystals? . . . 14
2.3.2 Physical interpretation of the KS eigenvalues . . . 15

3 Band Structure Methods 17
3.1 The Rayleigh-Ritz Variational Principle . . . 18
3.2 The APW Basis Set . . . 19
3.3 The LAPW Method . . . 21
3.3.1 The LAPW basis set . . . 21
3.3.2 Charge density and crystalline potential . . . 22
3.3.3 Local orbitals . . . 23
3.4 The APW+lo Method . . . 23

4 Linear Optical Response 25
4.1 The Random Phase Approximation . . . 25
4.2 Excitonic Effects via the BSE . . . 27
4.2.1 Dielectric response including e-h interactions . . . 27
4.2.2 Screened Coulomb interaction . . . 29
4.2.3 Back to the RPA . . . 29

5 Structural Optimization 31
5.1 Structural Properties of the Oligo-acenes 32
5.1.1 Lattice parameters at ambient pressure 33
5.1.2 Lattice parameters of anthracene up to 10 GPa 34
5.2 Internal Geometry 35

II Results and Discussion 37

6 Pressure Studies on Anthracene 39
6.1 Internal Geometry Optimization 39
6.1.1 Molecular orientation 39
6.1.2 Bond lengths and intermolecular distances 42
6.1.3 LDA results compared to GGA findings 43
6.1.4 Isothermal bulk modulus 43
6.1.5 Discussion 45
6.1.6 Summary 47
6.2 Electronic Properties 47
6.2.1 Band structure and DOS 48
6.2.2 The band gap 54
6.2.3 Electron densities 56
6.2.4 Conclusions 58
6.3 Optical Properties 58
6.3.1 Optical Spectra within the RPA 60
6.3.2 Optical spectra including e-h interactions 62
6.3.3 The optical gap 65
6.3.4 Spin singlet exciton wavefunctions 67
6.3.5 Conclusions 70

7 Properties of the Oligo-Acenes 71
7.1 Electronic Properties 71
7.1.1 Band structures 71
7.1.2 Band gaps 75
7.2 Optical Properties 77
7.3 Conclusions 82

8 Summing Up and Looking Ahead 83

III Appendix 89

A Computational Details 91
A.1 (L)APW Specific Parameters 91

A.2 The Dielectric Tensor 92
A.2.1 Within the RPA 92
A.2.2 By solving the BSE 94

B Convergence Tests 97
B.1 Brillouin Zone Sampling 97
B.2 The Number of Valence and Conduction Bands 97
B.3 Coulomb Screening 99

C More Structural Information 101
C.1 Experimental Data Sets 101
C.2 Enlarged Anthracene Structures 101

Bibliography 105

List of Figures 111

List of Tables 117

List of Publications 119

1 Introduction

We especially need imagination in science. It is not all mathematics, nor all logic, but is somewhat beauty and poetry.

Maria Mitchell

1.1 Overview

In 1977 the new field of research on *plastic electronics* was born by the discovery of conducting poly-acetylene $(CH)_x$ by A. J. HEEGER, A. G. MCDIARMID, and H. SHIRAKAWA [2, 3]. They found out that doping of $(CH)_x$ with halogens enables to increase the electrical conductivity by eleven orders of magnitude and thus changing its behavior from typical insulating to semiconducting or even to metallic. Its impact on modern science and technology has been recognized by The Nobel Foundation, which honored this work with the Nobel Prize in Chemistry 2000. Up to now, this forward-looking field of research enjoys a great interest of scientists and technicians all over the world, who contribute to its substantial progress [4, 5].

Besides the electrical conductivity, organic polymers based on π-conjugated molecules exhibit outstanding optical features in the UV/Vis region. This combination of high charge carrier mobility with high luminescence quantum yield makes such materials potential candidates for electro-optical devices, e.g., organic field effect transistors (OFETs) [6–9], photo-voltaic cells [10, 11], and organic light emitting diodes (OLEDs) [12–14]. Compared to conventional semiconductors used for such applications, the organic semiconducting polymers are advantageous in terms of mechanical flexibility, low molecular weight and low cost manufacturing.

A prerequisite for electro-optical device design is the detailed knowledge of the physical properties of these materials and the thorough understanding of the mechanism involved in their photophysics. The processes that govern the

charge carrier generation and recombination resulting in high electroluminescence yields are of particular interest. In order to gain insight into their physics, a huge variety of such polymers has been investigated experimentally as well as theoretically [15].

More than two decades, the scientists have concentrated on organic polymers. Doped poly-acetylene (PA) [16–18], poly-*para*-phenylene (PPP) [19–21], and poly-*para*-phenylene vinylene (PPV) [22–26] have been among the most prominent polymers of interest. Apart from conducting polymers, organic materials consisting of small π-conjugated molecules, which form well defined molecular crystals, experience their renaissance in this field of research. In particular, oligo-phenylenes [27–29], oligo-thiophenes [30–32], as well as pentacene [33–36] are also suitable for innovative opto-electronic devices. In contrast to organic polymers, where the building blocks are *infinite* chains, the oligomers form well defined molecular crystals containing finite molecules. For this reason, differences in the photophysical mechanisms underlying the electro-optical properties are expected. In this thesis, an ab-initio study of the physical properties of naphthalene, anthracene, tetracene, and pentacene is presented. These compounds are the first four members in the group of oligoacenes and prime examples for organic molecular crystals.

1.2 Motivation

Much effort has been placed into the experimental investigation of the electro-optical properties of organic semiconducting materials and still open problems remained. For instance, studies on the optical absorption processes of such compounds give controversial answers to the question, whether the lowest energy transition is due to free charge carriers (direct interband transitions) or the absorption of tightly bound excitons (Frenkel exciton model) [37–39]. In this context the experimentally determined exciton binding energies published for PPV range from 0.1 to 0.9 eV [40].

In general, the electro-optical properties strongly depend on the crystalline structure of such materials, which in turn is governed by the intermolecular (interchain) interactions inherently present in the three-dimensional (3D) environment. Typically, the intramolecular bonds in these materials are rather rigid, whereas the intermolecular interactions are believed to be weak long-range van der Waals type. Thus it is in general assumed that the molecules in the crystal do not influence each other very strongly. For this reason, it is usually argued, that the optical properties of organic molecular crystals are similar to those of the single molecule and the intermolecular interactions are often neglected. However, the importance of considering these interactions

in theoretical models to correctly describe organic semiconducting polymers has been pointed out recently [18, 26, 41]. One possibility to study the role of the intermolecular interactions is the application of hydrostatic pressure, which enhances them due to the reduction of the unit cell volume.

The oligo-acenes exhibit a specific feature that is very common for organic molecular crystals built of planar rod-like molecules [42]: the so-called *herringbone* arrangement. Due to this stacking, two inequivalent oligomers are present in the unit cell. Therefore, the oligo-acenes are computationally demanding examples for ab-initio calculations based on the DFT and investigations, which take into account the full 3D environment are rare so far. Nevertheless, the interesting facts given above that concern organic molecular crystals in general, have motivated the density functional theory (DFT) [43, 44] study on the first four members of the oligo-acenes. To this extent, highly reliable 3D methods based on DFT allow to clarify the role of the intermolecular interactions and gain insight in the material-dependent electro-optical activity.

1.3 Aims

Regarding the problems outlined before, several questions remained, which are formulated below. The corresponding answers could be given during the work presented in this thesis.

- **How do the intermolecular interactions affect the structural properties, in particular, the herringbone stacking in organic molecular crystals?**
  This question could be answered by optimizing the internal and molecular geometry of anthracene as a function of pressure up to 10 GPa in comparison to experimental results.

- **Are the common approximations for the exchange-correlation potential within the DFT applicable to correctly describe the physical properties of organic molecular crystals?**
  To tackle this problem, the total energy of anthracene has been calculated as a function of volume utilizing the local density (LDA) and the generalized gradient (GGA) approximation. Furthermore, the pressure dependence of the band structure and electron density has been thoroughly analyzed.

- **What is the nature of the lowest optical transitions in anthracene?**
  This puzzle has been lifted by computing the dielectric function accounting for electron-hole interactions, i.e., solving the Bethe-Salpeter equa-

tion (BSE) for the two-particle Green's function within an ab-initio framework.

- **How are the lowest optical transitions in anthracene affected by the intermolecular interactions?**
  In order to find an answer for this question, the BSE has been solved for the structurally optimized anthracene at several pressure values between ambient pressure and 10 GPa.

- **What is the influence of the oligomer length on the electronic and optical properties?**
  An answer to this question has been obtained by calculating band structures and dielectric tensors for the series of oligo-acenes at ambient pressure.

1.4 Outline

This thesis is organized as follows:

- The first part summarizes the basic theoretical concepts concerning ab-initio solid state theory. The key ideas of DFT, the widely used LDA and GGA for treating the exchange-correlation effects within this theory and their limitations are given in Chapter 2. Chapter 3 is dedicated to band structure methods, in particular the full-potential (linearized) augmented plane wave method FP-(L)APW as implemented in the **WIEN2k** program [45]. Chapter 4 deals with the description of optical properties of solids. Within this chapter, Sec. 4.1 is devoted to the random phase approximation (RPA), whereas Sec. 4.2 introduces the Bethe-Salpeter equation for the two-particle Green's function, which accounts for the electron-hole interactions not considered in the RPA. Chapter 5 addresses the concepts of the internal geometry optimization and summarizes the structural data of the oligo-acenes.

- In the second part, the results of the FP-(L)APW calculations performed with the **WIEN2k** code using the LDA and the GGA are presented. In Chapter 6 the structural, electronic and optical properties of anthracene as a function of pressure are discussed in detail. Chapter 7 deals with the electronic and optical properties of the investigated series of oligo-acenes. Chapter 8 summarizes the conclusions and points out some interesting aspects for future investigations.

- The last part includes the computational details regarding program specific input parameters in Appendix A. Some convergence tests concerning the linear optical response calculations are given in Appendix B. More details about structural parameters are summarized in Appendix C. These are the experimental data sets of anthracene under pressure obtained from different diffraction measurements as well as extrapolated lattice parameters required for the computation of the total energy as a function of volume. The thesis is completed with the bibliography, the list of figures and tables as well as the list of publications related to this work.

Part I

Theoretical Toolbox

2 Density Functional Theory

Es gibt nichts Praktischeres als eine gute Theorie.

Immanuel Kant

The goal of ab-initio solid state theory is to calculate the physical properties of solids without adjustable parameters. Among different approaches DFT has become one of the most powerful ab-initio methods. Before the density functional method is further described, the prerequisites of ab-initio solid state theory are recalled.

When examining the physics of solids, one has to deal with many-electron systems and with the infinite periodic array of atoms in the crystal. Thus some idealizations and approximations have been introduced:

- The idealized crystal is described by its unit cell, from which the whole infinite crystal can be constructed by translation. The unit cell and thus the crystal lattice are determined by three lattice vectors.
- The reciprocal lattice with lattice vectors orthonormal to those of the direct lattice is introduced. The crystalline many body wavefunction, for which the Schrödinger equation is solved, is a *Bloch function* $\Psi_{\mathbf{k}}$. The wave vector $\mathbf{k}$ represents a quantum number and can be restricted to the reciprocal unit cell (Brillouin zone). If the symmetry of the crystal is considered, $\mathbf{k}$ can be further confined within the irreducible wedge of the Brillouin zone (IBZ).
- Since the nuclear mass is much larger than the electron mass, the electrons can respond almost instantaneously to any change in the nuclear positions. Therefore, to a good approximation, the nuclei can be regarded as stationary particles, in which potential the electrons move. This is the well-known *Born-Oppenheimer approximation*. Within this approximation, the nuclear kinetic energy term and the nuclear-nuclear

repulsion term can be both removed from the full Hamiltonian. The resulting Hamiltonian concerns the electrons only and is suitable to solve the electronic part of the Schrödinger equation that reads $\hat{H}_{\mathrm{elec}}\Psi_{\mathrm{elec}}(\mathbf{r}_i;\mathbf{R}) = E_{\mathrm{elec}}\Psi_{\mathrm{elec}}(\mathbf{r}_i;\mathbf{R})$. The notation $\Psi_{\mathrm{elec}}(\mathbf{r}_i;\mathbf{R})$ implies that the electronic wavefunction depends on the nuclear positions parametrically only.

The remaining electronic problem is still very complex. In order to treat the electron-electron interactions in many electron systems several methodologies have been established. One of them is the HARTREE-FOCK (HF) scheme, where the many body wavefunction is described by a Slater determinant. An alternative approach to scale down the many body problem to a set of single-particle equations is the density functional scheme, which is outlined in the following section.

2.1 Key Concepts of DFT

In 1964 HOHENBERG and KOHN [43] formulated the two famous theorems of DFT and thereby gave the foundation for the breakthrough in ab-initio solid state theory.

- Every observable of a stationary quantum mechanical system is determined by the ground state density alone. The ground state energy of an interacting inhomogeneous electron system $E_{\mathrm{tot}}[n(\mathbf{r})]$ in the presence of some external potential $V_{\mathrm{ext}}(\mathbf{r})$[1] is a *functional* F of the charge density $n(\mathbf{r})$:

$$E_{\mathrm{tot}}[n(\mathbf{r})] = \int V_{\mathrm{ext}}(\mathbf{r})n(\mathbf{r})\mathrm{d}\mathbf{r} \; + \; F[n(\mathbf{r})] \tag{2.1}$$

- The exact ground state density of a system in a particular external potential $V_{\mathrm{ext}}(\mathbf{r})$ is the density that minimizes $E_{\mathrm{tot}}[n(\mathbf{r})]$.

According to this formulation it is important to point out:

- The charge density $n(\mathbf{r})$ is the basic variable in the DFT.
- The functional $F[n(\mathbf{r})]$, which is independent of $V_{\mathrm{ext}}(\mathbf{r})$, is a *universal* density functional, i.e., applicable to any arbitrary system.
- The form of $F[n(\mathbf{r})]$ is not known explicitly. Therefore, some approximation for this functional is required.

[1] the potential that is caused by the nuclei

In 1965 KOHN and SHAM [44] suggested that the ground state density of the interacting system (solution of Eq. (2.1)) can be obtained, if the real system is replaced by an auxiliary system of non-interacting electrons, which has exactly the same charge density as the real system. Thereby the total ground state energy is split in different contributions:

$$E_{\mathrm{tot}}[n(\mathbf{r})] = T_{\mathrm{s}}(n(\mathbf{r})) + E_{\mathrm{ee}}(n(\mathbf{r})) + E_{\mathrm{NN}} + E_{\mathrm{Ne}}(n(\mathbf{r})) + E_{\mathrm{x}}(n(\mathbf{r})) + E_{\mathrm{c}}[n(\mathbf{r})]. \quad (2.2)$$

Therein, T_{s} represents the kinetic energy of non-interacting electrons. The sum of E_{ee} and E_{NN} denotes the Coulomb energy, i.e., the electron-electron plus the nucleus-nucleus repulsion, respectively. E_{Ne} marks the electrostatic attraction between electrons and nuclei. E_{x} stands for the exchange energy, which is manifested in the PAULI principle. Except the correlation energy E_{c} that arises from the interaction between electrons with the same spin, all the contributions to $E_{\mathrm{tot}}[n(\mathbf{r})]$ are known explicitely. The correlation energy is defined as the energy difference between the exact ground state energy and the sum of the first five energy terms considered in Eq. (2.2). Since the exact kinetic energy T is replaced by the kinetic energy of the non-interacting system T_{s}, the E_{c} also accounts for $T - T_{\mathrm{s}}$. In contrast to the HF method, which includes E_{x} exactly, but completely omits correlations, the DFT combines the exchange and correlation energy in a single term $E_{\mathrm{xc}}[n(\mathbf{r})] = E_{\mathrm{x}}(n(\mathbf{r})) + E_{\mathrm{c}}[n(\mathbf{r})]$, which is then treated in an approximate way.

In the next step, KOHN and SHAM introduced orbitals $\phi_i(\mathbf{r})$, which define the density by

$$n(\mathbf{r}) = \sum_{i=1}^{N} |\phi_i(\mathbf{r})|^2 \quad (2.3)$$

and applied the second HOHENBERG-KOHN theorem, i.e., minimizing the total energy with respect to the density according to the Rayleigh-Ritz variational principle, which will be further explained in Sec. 3.1. By working out this ansatz they could conclude that the minimizing density $n(\mathbf{r})$ can be obtained by solving single-particle Schrödinger equations

$$\hat{H}\phi_i(\mathbf{r}) = \epsilon_i \phi_i(\mathbf{r}), \quad (2.4)$$

with the KOHN-SHAM Hamiltonian $\hat{H}$ and the exchange-correlation (xc) potential $V_{\mathrm{xc}}(\mathbf{r})$ defined as:

$$\hat{H} = \big[-\frac{1}{2}\nabla^2 + V_{\mathrm{C}}(\mathbf{r}) + V_{\mathrm{xc}}(\mathbf{r}) \big] \quad (2.5)$$

$$V_{\mathrm{C}}(\mathbf{r}) = V_{\mathrm{ext}}(\mathbf{r}) + V_{\mathrm{H}}(\mathbf{r}) \quad (2.6)$$

$$V_{\mathrm{xc}}(\mathbf{r}) = \frac{\partial E_{\mathrm{xc}}[n(\mathbf{r})]}{\partial n(\mathbf{r})}. \quad (2.7)$$

The first term $-\frac{1}{2}\nabla^2$ in Eq. (2.5) corresponds to the single-particle kinetic energy, whereas $V_{\mathrm{C}}(\mathbf{r})$ denotes the Coulomb potential. The latter is the sum of the external potential $V_{\mathrm{ext}}(\mathbf{r})$ and the Hartree potential $V_{\mathrm{H}}(\mathbf{r})$. The index i counts the occupied orbitals $\phi_i(\mathbf{r})$, which are the Bloch functions of a single electron in the i-th orbital with the energy ϵ_i. The xc potential $V_{\mathrm{xc}}(\mathbf{r})$ is obtained as the derivative of the xc energy with respect to the charge density. Equations (2.3), (2.4), and (2.7) are known as the KOHN-SHAM (KS) equations. These equations can only be iteratively solved for the following reason: All terms included in the KS Hamiltonian $\hat{H}$ depend on the charge density $n(\mathbf{r})$, which in turn is calculated from the wavefunction using (2.3). However, in order to define the Hamiltonian, the knowledge of the charge density is required. In practice, this iterative scheme is known as the self-consistent field (SCF).

Up to now, the many body problem has been reduced to a set of single-particle KS equations that can be solved self-consistently to yield the ground state energy of an extended system. There remains one crucial point, which decides on the success of the DFT: a good approximation for the xc energy functional $E_{\mathrm{xc}}[n(\mathbf{r})]$.

2.2 Approximations for the xc Energy Functional

In this section, two widely used approximations for the xc energy functional are briefly explained.

2.2.1 The Local Density Approximation (LDA)

In the LDA, $E_{\mathrm{xc}}[n(\mathbf{r})]$ is approximated by a function, which is valid for the homogeneous electron gas:

$$E_{\mathrm{xc}}^{\mathrm{LDA}}[n] = \int n(\mathbf{r})\varepsilon_{\mathrm{xc}}^{\mathrm{LDA}}(n(\mathbf{r}))\mathrm{d}\mathbf{r}. \tag{2.8}$$

The expression $\varepsilon_{\mathrm{xc}}^{\mathrm{LDA}}$ denotes the xc energy per particle of an uniform electron gas, i.e., the local xc energy density [44]. Further, the $E_{\mathrm{xc}}^{\mathrm{LDA}}$ is split into its contributions:

$$E_{\mathrm{xc}}^{\mathrm{LDA}} = E_{\mathrm{x}}^{\mathrm{LDA}} + E_{\mathrm{c}}^{\mathrm{LDA}}. \tag{2.9}$$

The exchange energy is calculated analytically by replacing the $E_{\mathrm{x}}^{\mathrm{LDA}}$ of an inhomogeneous electron gas by that of a homogeneous electron gas with the same charge density at each position by

$$E_{\mathrm{x}}^{\mathrm{LDA}} \propto n(\mathbf{r})^{4/3}. \tag{2.10}$$

According to Eq. (2.7) the corresponding exchange potential $V_{\mathrm{x}}^{\mathrm{LDA}}$ is

$$V_{\mathrm{x}}^{\mathrm{LDA}} \propto n(\mathbf{r})^{1/3}. \tag{2.11}$$

The exchange contribution remains the same in all LDA functionals available. They are only distinguished by the type of parameterization used for the correlation energy $E_{\mathrm{c}}^{\mathrm{LDA}}$ resulting in a particular form of $\varepsilon_{\mathrm{xc}}^{\mathrm{LDA}}$. CEPERLEY and ALDER obtained the $E_{\mathrm{c}}^{\mathrm{LDA}}$ for the homogeneous electron gas by *Quantum Monte Carlo* simulations [46]. Throughout this work the very common PERDEW-WANG parameterization [47] of these CEPERLEY and ALDER data is meant whenever the LDA is stated.

Despite this simple approximation of the xc potential, the LDA has been able to yield very satisfying results for the ground state properties of systems, which are even not homogeneous. However, the LDA has shortcomings. In particular, one of them had to be faced in this thesis: Concerning the structural properties of solids, the LDA tends to underestimate the bond length by 1-5% compared to experimental values. Other insufficiencies will be discussed below.

2.2.2 The Generalized Gradient Approximation (GGA)

As stated above, the LDA uses the xc energy density $\varepsilon_{\mathrm{xc}}^{\mathrm{LDA}}$ for the uniform electron gas at every point in the system regardless of the homogeneity of the real charge density. For non-uniform charge densities the xc energy can deviate significantly from the uniform result. The GGA utilizes a functional f_{xc} that is a function of the density and its gradient to correct for this deviation. The resulting xc functional has the following form:

$$E_{\mathrm{xc}}^{\mathrm{GGA}}[n(\mathbf{r})] = \int f_{\mathrm{xc}}(n(\mathbf{r}), |\nabla n(\mathbf{r})|) n(\mathbf{r}) \mathrm{d}\mathbf{r}, \tag{2.12}$$

As the $\varepsilon_{\mathrm{xc}}^{\mathrm{LDA}}$ in LDA, this f_{xc} must be parameterized by analytic functions to facilitate practical calculations.

From a historically viewpoint, a fairly simple approach to $E_{\mathrm{xc}}[n(\mathbf{r})]$ has already been suggested by KOHN and SHAM [44], who proposed to express the xc energy in a gradient expansion of the charge density and include the second order terms $|\nabla n(\mathbf{r})|^2$. This is the gradient expansion approximation (GEA). However, such a xc functional has not been able to rigorously improve over the LDA functional and even did often worse than the LDA [48]. One step further is to construct a first-principles numerical GGA by starting form this second-order gradient expansion for the xc hole surrounding the electron in a system of slowly varying density and than cutting off its spurious long-range parts.

Thereby unphysical contributions to the GEA hole are removed. An analytic fit to this numerical GGA is the PERDEW-WANG functional GGA-PW91 [49]. This xc functionals has also its problems, which can be overcome by an efficient scheme proposed by PERDEW, BURKE and ERNZERHOF [50]. The so-called GGA-PBE [50] has proven to be very successful for systems, where the charge density is slowly varying. Throughout this thesis it is referred to as GGA.

2.3 Limitations of the LDA and the GGA

2.3.1 Applicability for molecular crystals?

One of the major problems of the LDA is the well-known overbinding effect [51]. It is responsible for the underestimation of the bond lengths and thus the equilibrium volume as well as the overestimation of the bulk modulus. In particular, it has been argued that the strength of the hydrogen bond is seriously overestimated in the LDA [52], but the gradient corrected functionals (GGA's) successfully compensate for this effect [50, 53, 54]. However, both types of functionals have shortcomings in the description of weak long-range interactions such as the *van der Waals* (vdW) force [52, 53, 55–57], which are commonly believed to be the main bonding forces in organic molecular crystals. In Ref. [54], the equilibrium bond lengths, atomization energies and vibrational frequencies of a variety of rare-gas dimers obtained by DFT calculations utilizing three xc functionals, the LDA-PW91 [58], the GGA-PW91 [49], and the GGA-PBE [50] are reported. This study allows to conclude that the GGA functionals significantly improve over the LDA values. Moreover, they found that the GGA-PBE functional leads to bound dimers.

In contrast, a similar study of a benzene dimer and orthorhombic benzene using the LDA and the GGA functionals [52] revealed that the GGA's give a mechanically unstable crystal. Therefore it could be argued that the well-known overbinding of the LDA potential compensates for the missing vdW force and for that reason reasonable results concerning the internal geometry of molecular crystals are expected.

Summarizing these controversial findings there is no consensus on the applicability of different xc functionals for materials, which are considered to be vdW bond. For this reason, both, the LDA and the GGA-PBE xc potentials have been utilized for the ab-initio study of anthracene. The corresponding results presented in the second part of this thesis will help to validate the ab-initio description using the LDA and the GGA-PBE of organic molecular crystals.

2.3.2 Physical interpretation of the KS eigenvalues

In many cases, not only the ground state properties of solids, but also the band structure and excited state properties, e.g., the linear optical response, are of interest. In order to extract such quantities from DFT, one step further has been made by relating the KS eigenvalues ϵ_i to the band structure and thus interpreting the excitation spectrum of the solid in terms of ϵ_i. However, the KS eigenvalues enter the DFT formalism as Langrange multipliers and thus do not have any physical meaning. Since the band structures of many materials obtained by this procedure agree well with experimental findings, such an interpretation of the ϵ_i has been generally accepted, but is in principle an *illegitimate child of DFT* [59]. Therefore, when the band gaps of insulators and semiconductors are calculated under this assumption, they are underestimated by approximately 50%, in particular, if the LDA is used for the xc effects.

In order to overcome this *band gap problem* [60–62], which is related to the discontinuity of the xc potential of the $(N+1)$-particle system, basically two methods have been established in the past. One possibility is to go *beyond DFT* to many body perturbation theory [63] and introduce quasi-particles, which are approximate eigenstates of the many body Hamiltonian including the non-local energy dependent self-energy operator $\Sigma(\mathbf{r}, \mathbf{r}'; E)$. Therein the Green's function[2] turned out to properly describe electron addition and removal processes and therefore gives access to the excitation spectrum of extended systems. The calculation of the Green's function requires the knowledge of the self-energy operator $\Sigma(\mathbf{r}, \mathbf{r}'; E)$, which rigorously contains exchange and correlation effects and can be calculated using the GW approximation introduced by HEDIN [64, 65]:

$$\Sigma(\mathbf{r}, \mathbf{r}'; E) = \frac{i}{2\pi} \int e^{iE'\eta} G(\mathbf{r}, \mathbf{r}'; E + E') W(\mathbf{r}, \mathbf{r}'; E) \mathrm{d}E', \tag{2.13}$$

where $G(\mathbf{r}, \mathbf{r}'; E + E')$ denotes the single-particle propagator of the interacting system and $W(\mathbf{r}, \mathbf{r}'; E)$ represents the dynamically screened electron-electron interaction. Eq. (2.13) is the first term in an expansion of the self-energy in powers of $W(\mathbf{r}, \mathbf{r}'; E)$. Up to now, the GW approximation has been successfully employed to many systems [66] and yields good quasi-particle energies, i.e., band structures and excited state properties. Nevertheless, GW computations are a fairly demanding task in case of large extended systems.

A completely different approach is time-dependent density functional theory (TD-DFT) [67], which is an extended density functional formalism for excited many body systems. In the TD-DFT framework the excitation energies are calculated from the poles of the linear response function and provide good

[2] The Green's function is defined as the expectation value of the time-ordered product of creation and annihilation field operators and is also called *propagator*.

spectra in case of atoms and molecules. However, its application to extended systems is not yet completely validated [68].

Despite these sophisticated methods the ϵ_i are still usually used as an approximation to the single particle energies. Since in many semiconductors the self-energy turned out to be independent of $\mathbf{k}$, a rigid upward shift Δ_c of the KS conduction band energies turned out to be sufficient for correcting the band gaps [69]. This is the widely applied *scissors operator approximation*.

3 Band Structure Methods

Be less curious about people and more curious about ideas.

Marie Curie

In Chapter 2, it has already been pointed out that the KS equations require an iterative procedure to be solved. This can be achieved by choosing a proper set of basis functions and by making advantage of the Rayleigh-Ritz variational principle. In this chapter, we focus on the procedure for generating a good basis set for crystalline wavefunctions. The corresponding approaches, are known as *band structure methods*. They can be distinguished according to the type of basis set they are using and what form of the potential is chosen. Concerning basis sets, plane waves, muffin tin orbitals, and Gaussian or Slater type orbitals are widely used. Regarding the potential, the atomic sphere approximation, the muffin tin approximation, pseudopotentials, and full potential methods have been established. The band structure methods can now be grouped with respect to different features:

- LCAO-methods: The Bloch functions are constructed by a linear combination of atomic orbitals, which are commonly expressed as atom-centered Gaussian type orbitals (GTOs).
- The muffin-tin methods: The common feature in these methods is the division of the unit cell into atomic spheres and an interstitial region. For both regions an appropriate basis set is chosen and combined to form an efficient basis. This group includes the (L)APW method, the linear combination of muffin tin orbitals (LMTO) method and the KORRINGA-KOHN-ROSTOCKER (KKR) method. With these basis functions a completely general potential without any shape approximation (full-potential) can in principle be treated. Within the LMTO scheme, for example, the potential can be treated spherically symmetric inside the sphere and constant outside the sphere. This approach is called the muffin tin approximation.

- The atomic sphere approximation (ASA) methods: The ASA approximates the unit cell with overlapping atomic spheres. The sum of the volumes of these atomic spheres is constrained to be equal to the unit cell volume. The interstitial region is not treated explicitly, but is compensated by the overlapping regions. Inside each atomic sphere both, the charge density and the potential are assumed to be spherically symmetric. Those methods work well for closely packed systems, but are not very accurate for layered structures or open structures. This scheme is utilized in the augmented spherical wave (ASW) method and also realized in the LMTO-ASA method.
- The pseudopotential (PP) methods: In a sphere around each atom the true potential and the corresponding all-electron wavefunctions are replaced by a smooth pseudopotential without the singularity at the nucleus and the resulting nodeless pseudo wavefunctions. Outside the sphere, the pseudo and all-electron wavefunctions coincide and therefore should lead to the same chemical bonding. Choosing the smooth potential makes plane waves (PWs) applicable to well expand this pseudo wavefunctions by a reasonable number of such site-independent basis functions. This has been accomplished in the plane wave pseudopotential method.

Note, that this classification cannot be regarded as unique, since different criteria can apply to one method.

3.1 The Rayleigh-Ritz Variational Principle

Since the exact wavefunction for solids is not known a priori, a trial function $\Psi_{\mathbf{k}}$ is used instead. $\Psi_{\mathbf{k}}$ is set up as linear combination of basis functions Φ_i, which are weighted by coefficients C_i:

$$\Psi_{\mathbf{k}} = \sum_{i=1}^{n} C_i \Phi_i. \tag{3.1}$$

The expectation value of the energy $\langle E \rangle$ is given by:

$$\langle E \rangle = \frac{\int \Psi^*_{\mathbf{k}}(C_1, \ldots, C_n) \hat{H} \Psi_{\mathbf{k}}(C_1, \ldots, C_n) \mathrm{d}\mathbf{r}}{\int \Psi^*_{\mathbf{k}}(C_1, \ldots, C_n) \Psi_{\mathbf{k}}(C_1, \ldots, C_n) \mathrm{d}\mathbf{r}} \tag{3.2}$$

The lowest $\langle E \rangle$ is obtained by the condition:

$$\frac{\partial \langle E \rangle}{\partial C_i} = 0 \qquad i = 1, \ldots, n \tag{3.3}$$

This corresponds to the Rayleigh-Ritz variational principle that states:
The expectation value of any trial function is always greater than the eigenvalue of the exact wavefunction.

Building the derivatives with respect to C_i for $i = 1, \ldots, n$, yields a set of n equations, the so-called *secular equation*:

$$\sum_{j=1}^{n}(H_{ij} - \epsilon_i S_{ij})C_j = 0 \tag{3.4}$$

$$H_{ij} = \int \Phi_i^* \hat{H} \Phi_j \mathrm{d}^3\mathbf{r} \tag{3.5}$$

$$S_{ij} = \int \Phi_i^* \Phi_j \mathrm{d}^3\mathbf{r}, \tag{3.6}$$

where H_{ij} are the matrix elements of the single-particle KS Hamiltonian $\hat{H}$ and S_{ij} denotes the overlap matrix elements. This equation represents a *general eigenvalue problem*. A non-trivial solution to the secular equation (3.4) only exists, if the corresponding determinant vanishes:

$$|H_{ij} - \epsilon_i S_{ij}| = 0. \tag{3.7}$$

We end up with a polynomial function in ϵ_i with the highest power n, the so called *characteristic polynomial function*. Once ϵ_i is known, it is substituted in Eq. (3.4) and the variational coefficients C_j are determined. Thus the trial function $\Psi_{\mathbf{k}}$ in Eq. (3.1) is defined completely. Furthermore, the obtained energy eigenvalues ϵ_i are real values, since the Hamiltonian and the overlap matrix are hermitian.

This procedure is applied in case of energy dependent matrices $\hat{H}$ and S_{ij}. When the basis set is independent of energy, the eigenvalue problem reduces to a linear one and the eigenvalues ϵ_i are obtained in a single step by the diagonalization of the expression given in Eq. (3.4).

3.2 The APW Basis Set

In a very simple approach PWs are used to create an appropriate basis set. They describe the wavefunctions of the delocalized electrons well. However, in the vicinity of the atomic core, the wavefunctions have nodes and strong oscillations, which cannot be expanded well in a reasonable number of PWs. In 1937 SLATER first suggested to augment the PW set with another type of basis functions appropriate for the atomic spheres, which resulted in the APW method [70]. The straightforward idea illustrated in Fig. 3.1 was to divide the unit cell of the crystal in two regions, namely into

- non-overlapping atomic spheres (S) centered at the nuclear positions and
- the interstitial region (I, hatched in Fig. 3.1).

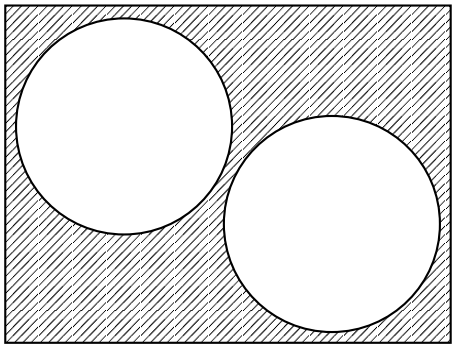

Figure 3.1: Partition of the unit cell into atomic spheres and interstitial region (hatched area) in the (L)APW method.

Thus the augmented basis set consists of PWs that match atomic-like wavefunctions at the atomic sphere boundary:

$$\Phi^{\mathrm{APW}}_{\mathbf{k}+\mathbf{G}}(\mathbf{r}) = \begin{cases} \dfrac{1}{\sqrt{\Omega}} e^{\mathrm{i}(\mathbf{k}+\mathbf{G})\mathbf{r}} & \mathbf{r} \in \mathrm{I} \\ \displaystyle\sum_{l=0}^{l_{max}} \sum_{m=-l}^{+l} A^{\alpha}_{lm}(\mathbf{k}+\mathbf{G}) u_l(r_\alpha, E) Y_{lm}(\hat{r}_\alpha) & \mathbf{r} \in \mathrm{S} \end{cases} \tag{3.8}$$

Here, $\frac{1}{\sqrt{\Omega}}$ denotes the normalization factor, while Ω, $\mathbf{k}$, and $\mathbf{G}$ represent the unit cell volume, the wave vector within the IBZ, and a reciprocal lattice vector, respectively. $u_l(\mathbf{r}_\alpha, E)$ and $Y_{lm}(\hat{r}_\alpha)$ are the radial part and the spherical harmonics of the atomic wavefunctions with $\mathbf{r}_\alpha$ being the distance between the electron and the nucleus position $\mathbf{R}_\alpha$ within the atomic sphere with the *muffin tin radius* radius R^{α}_{MT}.

$$\mathbf{r}_\alpha = \mathbf{r} - \mathbf{R}_\alpha, \qquad |\mathbf{r}_\alpha| \leq R^{\alpha}_{MT}. \tag{3.9}$$

l and m correspond to the angular momentum and magnetic quantum number, respectively. The coefficient $A^{\alpha}_{lm}(\mathbf{k}+\mathbf{G})$ is determined by matching each PW in value with the atomic basis function at the sphere boundary. The radial wavefunction $u_l(\mathbf{r}_\alpha, E)$ is energy dependent. In case of an atom, it is calculated for a given energy by a numerical outward integration of the radial Schrödinger equation starting with a regular solution at the origin (nucleus). Then the energy is varied until the radial wavefunction decays to zero for large $\mathbf{r}$. When used as a basis function in the APW basis set, the radial wavefunction is restricted to the size of the atomic sphere. As a consequence, the criterion of

the exponential decay at large $\mathbf{r}$ is lost. The $u_l(\mathbf{r}_\alpha, E)$ can be calculated for any energy, which is not necessarily an eigenstate of the radial Schrödinger equation. Since in the APW method, it is required at an eigenvalue of the KS equation, the basis set is energy dependent, which leads to a non-linear eigenvalue problem. This is solved by varying the energy to search for the roots of the determinant $|H_{ij} - \epsilon_i S_{ij}|$.

3.3 The LAPW Method

Solving a non-linear eigenvalue problem is an elaborate task, which can be simplified by a linearization of the APW basis functions. This idea goes back to ANDERSEN [71], who proposed to expand the energy dependence of $u_l(\mathbf{r}, E)$ by its energy derivative and thus has established the LAPW method.

3.3.1 The LAPW basis set

The basis set inside the atomic spheres S reads:

$$\phi_{\mathbf{k}+\mathbf{G}}(\mathbf{r}) = \sum_{l=0}^{l_{max}} \sum_{m=-l}^{+l} [A_{lm}^{\alpha}(\mathbf{k}+\mathbf{G}) u_l(r_\alpha, E_l) + B_{lm}^{\alpha}(\mathbf{k}+\mathbf{G}) \dot{u}_l(r_\alpha, E_l)] Y_{lm}(\hat{r}_\alpha) \quad (3.10)$$

Compared to the original APW basis set, the radial wavefunction for a fixed expansion energy E_l is used and its derivative $\dot{u}_l(r_\alpha, E_l)$ taken at the same energy is included. Note that the energy E_l is not an eigenvalue, but a fixed expansion energy chosen to be close to the center of the corresponding band with l-like character. Thus an energy independent basis is constructed that allows for the diagonalization of the Hamiltonian by which all eigenvalues are obtained simultaneously. The coefficients $A_{lm}^{\alpha}(\mathbf{k}+\mathbf{G})$ and $B_{lm}^{\alpha}(\mathbf{k}+\mathbf{G})$ are determined by requiring that each PW must match the atomic-like basis functions in value and slope at the sphere boundary.

Up to now, the individual basis functions for S and I have been defined. The crystalline wavefunction $\Psi_{\mathbf{k}+\mathbf{G}}(\mathbf{r})$ is then expressed as linear combination of the combined basis sets, i.e., the LAPWs:

$$\Psi_{\mathbf{k}+\mathbf{G}}(\mathbf{r}) = \sum_{i=1}^{n} C_i \Phi_{i_{\mathbf{k}+\mathbf{G}}}^{\mathrm{LAPW}}(\mathbf{r}) \quad (3.11)$$

$$\Phi_{i_{\mathbf{k}+\mathbf{G}}}^{\mathrm{LAPW}}(\mathbf{r}) = \begin{cases} \frac{1}{\sqrt{\Omega}} e^{\mathrm{i}(\mathbf{k}+\mathbf{G})\mathbf{r}} & \mathbf{r} \in \mathrm{I} \\ \sum_{l=0}^{l_{max}} \sum_{m=-l}^{+l} [A_{lm}^{\alpha} u_l(r_\alpha, E_l) + B_{lm}^{\alpha} \dot{u}_l(r_\alpha, E_l)] Y_{lm}(\hat{r}_\alpha) & \mathbf{r} \in \mathrm{S} \end{cases} \quad (3.12)$$

Such LAPW's are used for the description of the *valence* electrons only, which are defined in such a way that their wavefunction is delocalized over the whole unit cell. In particular, there is a non-vanishing probability for them to be located in I. The energy of these valence electrons is close to the Fermi level and thus they are clearly energetically distinguished from the *core* electrons. The latter are much deeper in energy and therefore can be assumed to be confined within S. In the LAPW method, which is an *all*-electron scheme, the core electrons are treated only inside the muffin-tin spheres by solving the relativistic Dirac equation for the spherical part of the potential [72].

3.3.2 Charge density and crystalline potential

The energy levels $\epsilon_{\mathbf{k}_i}$ are occupied with increasing energy according to the *aufbau principle* and to their weight w_i, which represents the number of equivalent $\mathbf{k}$-points in the IBZ, until no electron is left. The charge density $n(\mathbf{r})$ is calculated by summing over all occupied levels $\epsilon_{\mathbf{k}_i}$ up to the Fermi energy E_F with:

$$n(\mathbf{r}) = \sum_{\epsilon_{\mathbf{k}_i} \leq E_\mathrm{F}} w_i n_{\mathbf{k}_i}(\mathbf{r}) \tag{3.13}$$

$$n_{\mathbf{k}_i}(\mathbf{r}) = \Psi^*_{\mathbf{k}_i}(\mathbf{r})\Psi_{\mathbf{k}_i}(\mathbf{r}) \tag{3.14}$$

Analogous to the wavefunctions in the LAPW method, the valence electron density is expanded differently in S and I. Spherical harmonics are used inside the atomic spheres, whereas PWs are chosen for the interstitial:

$$\rho_\mathrm{val}(\mathbf{r}) = \begin{cases} \sum_{\mathbf{G}} \rho^v(\mathbf{r}) e^{\mathbf{iGr}} & \mathbf{r} \in \mathrm{I} \\ \sum_{lm} \rho^v_{lm}(\mathbf{r}) Y_{lm}(\hat{\mathbf{r}}) & \mathbf{r} \in \mathrm{S} \end{cases} \tag{3.15}$$

In addition, the electron density of the core electrons ($l = m = 0$) is assumed to be spherically symmetric and completely confined to the atomic spheres S. Thus the core contribution to the density $\rho_\mathrm{c}(\mathbf{r})$ for $\mathbf{r} \in \mathrm{I}$ is equal to zero, whereas it is given by $\rho^\mathrm{c}_{00}(\mathbf{G})Y_{00}$ for $\mathbf{r} \in \mathrm{S}$. The total charge density is the sum of the valence and the core contributions.

The KS potential $V(\mathbf{r})$ is expressed in the same form as the charge density:

$$V(\mathbf{r}) = \begin{cases} \sum_{\mathbf{G}} \tilde{V}(\mathbf{G}) e^{\mathbf{iGr}} & \mathbf{r} \in \mathrm{I} \\ \sum_{lm} V_{lm}(\mathbf{r}) Y_{lm}(\hat{\mathbf{r}}) & \mathbf{r} \in S \end{cases} \tag{3.16}$$

3.3.3 Local orbitals

One shortcoming of the linearized basis set in LAPW is that these basis functions inside an atomic sphere do not allow the simultaneous description of electronic wavefunctions with the same angular quantum number l, but with different principle quantum numbers n. Note that in equation (3.10) the radial wavefunction does not depend on n. Therefore the treatment of, e.g., 3p- and 4p-orbitals, in one energy window is not possible. In order to allow a consistent description of semi-core (e.g. 3p) and valence orbitals (e.g. 4p) in one energy window, SINGH introduced the *local orbitals* (lo's) [72, 73], which also improve the variational flexibility of the basis set. They are added to the basis set for S, i.e, they are confined to the atomic spheres, and are defined for a given angular quantum number l by

$$\phi_{lm}^{\mathrm{lo}}(\mathbf{r}) = \begin{cases} 0 & \mathbf{r} \in \mathrm{I} \\ [A_{lm}^{\mathrm{lo}} u_l(r_\alpha, E_l) + B_{lm}^{\mathrm{lo}} \dot{u}_l(r_\alpha, E_l) + C_{lm}^{\mathrm{lo}} u_l(r_\alpha, E_l^{\mathrm{lo}})] Y_{lm}(\hat{r}_\alpha) & \mathbf{r} \in \mathrm{S} \end{cases} \tag{3.17}$$

The additional radial wavefunction with the coefficient C_{lm}^{lo} is calculated at a second linearization energy E_l^{lo}, which can be set to the energy of the semi-core state. The coefficients A_{lm}^{lo}, B_{lm}^{lo}, and C_{lm}^{lo} are determined by the requirement that $\phi_{lm}^{\mathrm{lo}}(\mathbf{r})$ must be normalized and vanish in value and slope at the sphere boundary.

3.4 The APW+lo Method

Compared to the original APW scheme, the LAPW method has one major advantage, but also one considerable disadvantage:

(+) The basis set is energy independent resulting in an linear eigenvalue problem.

(–) A larger plane wave cut off is required for a proper description of the crystalline wavefunction.

Recently, SJÖSTEDT et al. [74] have shown, that the advantages of the APW and LAPW methods can be combined in the so-called APW+lo approach. That means, one starts with the APW basis set as described in Eq. (3.8), but with a fixed linearization energy E_l, and adds local orbitals specified for this energy:

$$\Phi_{\mathbf{k}+\mathbf{G}}^{\mathrm{APW+lo}}(\mathbf{r}) = \begin{cases} \dfrac{1}{\sqrt{\Omega}} e^{\mathrm{i}(\mathbf{k}+\mathbf{G})\mathbf{r}} & \mathbf{r} \in \mathrm{I} \\ \left.\begin{array}{l} \displaystyle\sum_{l=0}^{l_{max}} \sum_{m=-l}^{+l} A_{lm}^{\alpha}(\mathbf{k}+\mathbf{G}) u_l(r_\alpha, E_l) Y_{lm}(\hat{r}_\alpha) \\ [A_{lm}^{\mathrm{lo}} u_l(r_\alpha, E_l) + B_{lm}^{\mathrm{lo}} \dot{u}_l(r_\alpha, E_l)] Y_{lm}(\hat{r}_\alpha) \end{array}\right\} & \mathbf{r} \in \mathrm{S} \end{cases} \tag{3.18}$$

By this procedure, an energy independent basis set with reasonable variational flexibility is constructed. Calculations using such an APW+lo basis set converge to the same result as LAPW, but require a significantly smaller amount of PWs in the basis [74, 75]. Therefore, the size of the Hamiltonian to diagonalize is reduced to approximately the half. Thus the memory usage as well as the computation time decrease, which is crucial for investigating molecular crystals such as oligo-acenes.

4 Linear Optical Response

Mathematics began to seem too much like puzzle solving. Physics is puzzle solving, too, but of puzzles created by nature, not by the mind of man.

Maria Goeppert-Mayer

When studying the optical properties of solids, one is interested in the linear response due to an optical perturbation of the many-body system, i.e., the response generated by light in the visible region, which has a much larger wave length compared to the atomic scale of the sample. In this chapter, the main concepts of two methods, which allow to describe such properties starting from the density functional ground state (KS eigenvalues) are summarized. The next section is dedicated to the random phase approximation, which provides the dielectric function in a single-particle picture. Thereafter, the Bethe-Salpeter equation that is the equation of motion for the two-particle Green's function [76] is introduced. Compared to the former, the latter includes the electron-hole (e-h) interaction and thus it allows for the calculation of two-particle excitation spectra. The diagonalization of the Bethe-Salpeter equation yields e-h pair energies that subsequently enter the dielectric function.

4.1 The Random Phase Approximation

EHRENREICH and COHEN [77] developed the frequently used random phase approximation (RPA) to describe the linear optical response of extended systems in a self-consistent manner. They derived an expression for the dielectric function $\mathrm{Im}\ \varepsilon_{ij}(\omega)$ under the following assumptions:

- The electrons and holes move *independently* of each other in a self-consistent potential. This assumption is known as *the independent particle approximation*.

- The self-consistent potential $V(\mathbf{r},t)$ is the sum of the externally applied potential $V_{\rm ext}(\mathbf{r},t)$ and the screening potential $V_{\rm s}(\mathbf{r},t)$, which originates in the rearrangement of the electrons in the solid due to the external perturbation and is taken as a classical electrostatic screening potential without xc effects. This approximation accounts for the fact that electrons and holes are treated as independent particles.

- The local fields are neglected. In a treatment, where these effects are included, the microscopic dielectric matrix is first calculated by computing the irreducible polarization in the independent particle approximation. Therefrom, the macroscopic dielectric function is obtained from the $\{\mathbf{G}=\mathbf{0},\mathbf{G}'=\mathbf{0}\}$ component of the inverse microscopic dielectric matrix. By neglecting the local fields, the macroscopic dielectric function can be directly related to the irreducible polarization, in particular, only the $\mathbf{G}=\mathbf{G}'=\mathbf{0}$ component of it is needed. Consequently, the matrix inversion that requires much computational effort, is considerably reduced.

- The long wave length limit is applied. Optical excitations occur at much larger wave lengths compared to the characteristic momenta in solids and therefore can be treated in the limit $|\mathbf{q}|\rightarrow\mathbf{0}$.

Working out all these approximations [78] one arrives at the macroscopic dielectric function explicitely written like this:

$$\mathrm{Im}\varepsilon_{ij}(|\mathbf{q}|\rightarrow\mathbf{0},\omega)=\frac{8\pi^2}{\Omega}\frac{1}{\omega^2}\sum_{vc\mathbf{k}}\langle v\mathbf{k}|p_i|c\mathbf{k}\rangle\langle c\mathbf{k}|p_j|v\mathbf{k}\rangle\delta(E_{c\mathbf{k}}-E_{v\mathbf{k}}-\omega), \qquad (4.1)$$

where the indices v (c) and $\mathbf{k}$ represent the valence (conduction) band and a vector $\mathbf{k}$ in the IBZ. Ω and ω stand for the crystal volume and the frequency, respectively. $\langle v\mathbf{k}|p_i|c\mathbf{k}\rangle$ are the optical dipole matrix elements, where p_i denotes the i-th Cartesian component of the momentum operator. It is important to note, that $\mathrm{Im}\varepsilon_{ij}$ is a tensorial quantity with the number of independent components depending on the symmetry of the solid. Further, the energies $E_{n\mathbf{k}}$[1] in Eq. (4.1) denominate the quasi-particle energies of the corresponding quasiparticle wavefunctions $|n\mathbf{k}\rangle$. These quantities can be obtained on a GW level by solving

$$\big[-\frac{1}{2}\nabla^2+V_{\rm C}(\mathbf{r})\big]\Psi_{n\mathbf{k}}(\mathbf{r})+\int\mathrm{d}\mathbf{r}'\;\Sigma(\mathbf{r},\mathbf{r}';E_{n\mathbf{k}})\Psi_{n\mathbf{k}}(\mathbf{r}')=E_{n\mathbf{k}}\Psi_{n\mathbf{k}}(\mathbf{r}) \qquad (4.2)$$

A more simple approach is to use the KS orbitals for $|n\mathbf{k}\rangle$ and their corresponding energies $\epsilon_{n\mathbf{k}}$. Indeed several self-energy GW calculations have shown that

[1] n stands for v or c

- the KS orbitals are an almost perfect approximation for the corresponding quasi-particle wavefunctions [79, 80] and
- as emphasized before, in many cases the $\mathbf{k}$-independent, rigid upward shift Δ_c of the KS conduction band energies turned out to be a sufficient self-energy correction [69].

If the KS energies are used, it has been shown that the optical transition matrix elements $\langle v\mathbf{k}|\mathbf{p}|c\mathbf{k}\rangle$ in Eq. (4.1) have to be corrected (renormalized) for the non-locality in the self-energy operator [81]. However, within the RPA a rather simple expression for the dielectric function is obtained:

$$\mathrm{Im}\varepsilon_{ij}(\omega) = \frac{8\pi^2}{\Omega(\omega-\Delta_\mathrm{c})^2}\sum_{vc\mathbf{k}}\langle v\mathbf{k}|p_i|c\mathbf{k}\rangle\langle c\mathbf{k}|p_j|v\mathbf{k}\rangle \times \delta(\epsilon_{c\mathbf{k}}-\epsilon_{v\mathbf{k}}+\Delta_\mathrm{c}-\omega) \quad (4.3)$$

Note, this formulation of the dielectric tensor is still in the single-particle picture and therefore the electron-hole interaction is not considered in this model. In order to include these interactions in the dielectric function, one has to go beyond the RPA to a two-particle description. Such an ansatz is realized by the Bethe-Salpeter equation (BSE) for the two-particle Green's function [76].

4.2 Excitonic Effects via the BSE

4.2.1 Dielectric response including e-h interactions

The e-h interactions in optical absorption spectra are considered by solving the Bethe-Salpeter equation (BSE) for the e-h Green's function [76]. In this section, the most important formulas are summarized, whereas a comprehensive description of the formalism, the derivations of all equations and the implementation into the FP-(L)APW method (**WIEN2k** code) by PUSCHNIG is given in Refs. [78, 82].

The imaginary part of the dielectric function $\mathrm{Im}\varepsilon_{ii}(\omega)$ in its diagonal form and in the limit $|\mathbf{q}| \to \mathbf{0}$ is obtained by evaluating

$$\mathrm{Im}\varepsilon_{ii}(\omega) = \frac{8\pi^2}{\Omega}\sum_{\lambda}\left|\sum_{vc\mathbf{k}} A^{\lambda}_{vc\mathbf{k}}\frac{\langle v\mathbf{k}|p_i|c\mathbf{k}\rangle}{\epsilon_{c\mathbf{k}}-\epsilon_{v\mathbf{k}}}\right|^2 \times \delta(E^\lambda-\omega) \quad (4.4)$$

The indices v, c and $\mathbf{k}$, as well as Ω are the same as in Eq. (4.1). The *uncorrected* KS valence and conduction state energies are denoted by $\epsilon_{v\mathbf{k}}$ and $\epsilon_{c\mathbf{k}}$, and $\langle v\mathbf{k}|p_i|c\mathbf{k}\rangle$ are again the optical dipole matrix elements calculated within DFT-LDA. The quantities E^λ and $A^\lambda_{vc\mathbf{k}}$ entering this summation over all exciton

states λ are the eigenvalues and eigenvectors of the reformulated BSE. The original BSE is an integral equation that has been transformed into a matrix eigenvalue equation [78] of the following form:

$$\sum_{v'c'\mathbf{k}'} \hat{H}^{\mathrm{eff}}_{vc\mathbf{k},v'c'\mathbf{k}'} A^{\lambda}_{v'c'\mathbf{k}'} = E^{\lambda} A^{\lambda}_{vc\mathbf{k}} \tag{4.5}$$

The eigenvalues represent the excitation energies of the correlated e-h pair, while the eigenvectors can be interpreted as coupling coefficients and are used to construct the exciton wavefunctions:

$$\Phi^{\lambda}(\mathbf{r}_e, \mathbf{r}_h) = \sum_{vc\mathbf{k}} A^{\lambda}_{vc\mathbf{k}} \psi^{*}_{v\mathbf{k}}(\mathbf{r}_h) \psi_{c\mathbf{k}}(\mathbf{r}_e) \tag{4.6}$$

Therein $\mathbf{r}_e$ and $\mathbf{r}_h$ denote the electron and hole coordinates, respectively. The single-particle wavefunctions for valence and conduction states with momentum $\mathbf{k}$ are denoted with $\psi_{v\mathbf{k}}$ and $\psi_{c\mathbf{k}}$.

The effective Hamiltonian $\hat{H}^{\mathrm{eff}}$ of the BSE consists of three terms in case of spin singlet excitons

$$\hat{H}^{\mathrm{eff}}_{vc\mathbf{k},v'c'\mathbf{k}'} = \hat{H}^{\mathrm{diag}}_{vc\mathbf{k},v'c'\mathbf{k}'} + \hat{H}^{\mathrm{dir}}_{vc\mathbf{k},v'c'\mathbf{k}'} + 2\hat{H}^{\mathrm{x}}_{vc\mathbf{k},v'c'\mathbf{k}'} \tag{4.7}$$

The first term, $\hat{H}^{\mathrm{diag}}$, is a kinetic term given by the differences of quasi-particle energies ($E_{c\mathbf{k}}, E_{v\mathbf{k}}$), which can be approximated by Δ_{c} corrected KS energies:

$$\hat{H}^{\mathrm{diag}}_{vc\mathbf{k},v'c'\mathbf{k}'} = (E_{c\mathbf{k}} - E_{v\mathbf{k}}) \delta_{vv'} \delta_{cc'} \delta_{\mathbf{k}\mathbf{k}'} \tag{4.8}$$

The direct and the exchange interaction matrix elements, $\hat{H}^{\mathrm{dir}}$ and $\hat{H}^{\mathrm{x}}$, are given by the following integrals:

$$\hat{H}^{\mathrm{dir}}_{vc\mathbf{k},v'c'\mathbf{k}'} = -\int \mathrm{d}\mathbf{r}\mathrm{d}\mathbf{r}' \psi_{v\mathbf{k}}(\mathbf{r}) \psi^{*}_{c\mathbf{k}}(\mathbf{r}') W(\mathbf{r},\mathbf{r}') \psi^{*}_{v'\mathbf{k}'}(\mathbf{r}) \psi_{c'\mathbf{k}'}(\mathbf{r}') \tag{4.9}$$

$$\hat{H}^{\mathrm{x}}_{vc\mathbf{k},v'c'\mathbf{k}'} = \int \mathrm{d}\mathbf{r}\mathrm{d}\mathbf{r}' \psi_{v\mathbf{k}}(\mathbf{r}) \psi^{*}_{c\mathbf{k}}(\mathbf{r}) \bar{v}(\mathbf{r},\mathbf{r}') \psi^{*}_{v'\mathbf{k}'}(\mathbf{r}') \psi_{c'\mathbf{k}'}(\mathbf{r}') \tag{4.10}$$

The direct term $\hat{H}^{\mathrm{dir}}$ is attractive and thus responsible for the formation of bound excitons. Thus the bound e-h pair is energetically lower than the quasi-particle energy gap. The exchange term $\hat{H}^{\mathrm{x}}$ acts oppositely to the $\hat{H}^{\mathrm{dir}}$ and is not active for spin triplet excitations. This means that $\hat{H}^{\mathrm{x}}$ controls the details of the excitation spectrum, such as the splitting between spin singlet and spin triplet excitations. It is important to note that the direct interaction term contains the screened Coulomb interaction $W(\mathbf{r},\mathbf{r}')$, whereas in the exchange term the bare Coulomb interaction $\bar{v}(\mathbf{r},\mathbf{r}')$ without the long-range part is present.

4.2.2 Screened Coulomb interaction

The screened Coulomb interaction is given by

$$W^{(1)}_{\mathbf{GG'}}(\mathbf{q}) = \frac{4\pi\varepsilon^{-1}_{\mathbf{GG'}}(\mathbf{q})}{|\mathbf{q}+\mathbf{G}||\mathbf{q}+\mathbf{G'}|}, \tag{4.11}$$

where the quantity $\mathbf{q}$ denotes the difference between $\mathbf{k}$ and $\mathbf{k}'$ within the IBZ. In Eq. (4.11) the screened interaction is evaluated by calculating the full inverse dielectric matrix $\varepsilon^{-1}_{\mathbf{GG'}}$, which is taken to be static, i.e., at $\omega = 0$. Since the computation of this expression is rather demanding, the following approximations have also been considered:

$$W^{(2)}_{\mathbf{GG'}}(\mathbf{q}) = \frac{4\pi\delta_{\mathbf{GG'}}}{\varepsilon_{\mathbf{GG'}}(\mathbf{q})|\mathbf{q}+\mathbf{G}|^2} \tag{4.12}$$

$$W^{(3)}_{\mathbf{GG'}}(\mathbf{q}) = \frac{4\pi\delta_{\mathbf{GG'}}}{(\mathbf{q}+\mathbf{G})\cdot\tilde{\varepsilon}\cdot(\mathbf{q}+\mathbf{G})} \tag{4.13}$$

In Eq. (4.12) simply the diagonal part $\mathbf{G} = \mathbf{G}'$ of $\varepsilon^{-1}_{\mathbf{GG'}}$ is used to approximate W, whereas in Eq. (4.13) the full dielectric matrix $\varepsilon^{-1}_{\mathbf{GG'}}$ is replaced by a constant tensor $\tilde{\varepsilon}$.

4.2.3 Back to the RPA

Once we have arrived at the expression of the dielectric function in the two-particle picture, it is interesting to see, how it can be reduced to its formulation in the independent particle picture neglecting local field effects (Eq. (4.1)). For independent particles the $\hat{H}^{\mathrm{dir}}$ and $\hat{H}^{\mathrm{x}}$ are equal to zero. Therefore $\hat{H}^{\mathrm{eff}}$ is equal to $\hat{H}^{\mathrm{diag}}$, which is already diagonal. As a consequence, the eigenvectors and eigenvalues of Eq. (4.5) become

$$A^{\lambda}_{vc\mathbf{k}} = \delta_{\lambda,vc\mathbf{k}} \tag{4.14}$$

$$E^{\lambda} = (E_{c\mathbf{k}} - E_{v\mathbf{k}}). \tag{4.15}$$

Using these definitions in Eq. (4.4), reduces the double sum to a single sum over $vc\mathbf{k}$, since in the sum over λ just one term remains. Further, by considering the renormalization of the LDA optical transition matrix elements required in the quasi-particle picture, we obtain

$$\mathrm{Im}\varepsilon_{ii}(\omega) = \frac{8\pi^2}{\Omega}\frac{1}{\omega^2}\sum_{vc\mathbf{k}}|\langle v\mathbf{k}|p_i|c\mathbf{k}\rangle|^2 \times \delta(E_{c\mathbf{k}} - E_{v\mathbf{k}} - \omega), \tag{4.16}$$

which is identical to Eq. (4.1).

5 Structural Optimization

It is wrong to think that the task of physics is to find out how Nature is. Physics concerns what we can say about Nature.

Niels Bohr

The thorough understanding of the crystal structure, in particular, the molecular arrangement, is of great importance, when the electro-optical properties of organic semiconducting materials are studied. The structural properties itself are governed by the intermolecular interactions. Therefore, one aim of this work has been the detailed investigation, how these interactions influence the structural and further the electronic and optical properties of herringbone stacked organic molecular crystal. This has been achieved by combining experimental techniques with ab-initio calculations. The experimental contribution consists of X-ray diffraction measurements under high pressure and a subsequent Rietveld refinement of the experimental data. The former provide the lattice parameters as a function of pressure, whereas the latter yields the internal structure parameters defining as molecular orientation. In order to allow for the comparison between experiment and theory it is necessary to consider the structure optimization in our theoretical approach. For the following two reasons, we have restricted ourselves to the *internal* structure optimization, which includes the calculation of the optimized molecular orientation as well as the bond lengths and angles for a fixed set of lattice parameters:

- First of all, it was not a priori clear, if the LDA and the GGA xc functionals are applicable for these studies, i.e., a stable solid would be obtained.
- The materials studied have monoclinic and triclinic space group symmetries. Thus they are characterized by four and six lattice parameters, respectively. In addition, the molecular orientation is defined by three independent angles. For such low symmetric materials the optimization of this large set of degrees of freedom is computationally not affordable, even with the best computer power available at the time.

Before the general procedure of the internal structure optimization employed in this work is explained, the structural properties of the materials of interest are described in the next section.

5.1 Structural Properties of the Oligo-acenes

In this work, we present calculations on naphthalene (2A), anthracene (3A), tetracene (4A), and pentacene (5A), which are the first four members in the oligo-acene group. Each single oligo-acene molecule consist of sp^2-hybridized carbon atoms (C) and hydrogen atoms (H). In particular, each C forms three covalent σ-bonds, the fourth valence electron stays in a 2p-orbital perpendicular to the molecular plane generating the aromatic π-electron cloud. The oligo-acene molecules are rather rigid and planar due to this aromatic type of bonding. In comparison, the inter-ring σ-bonds in oligo-phenyls are more flexible. For example, in biphenyl the two phenyl rings are tilted with respect to each other. When pressure is applied the biphenyl molecules become planar [83]. The planarity of the oligo-acene molecules is preserved in the crystalline environment. In Fig. 5.1 one anthracene molecule is depicted as example. The black and grey lines represent C-C and C-H σ bonds, respectively. The π-electron cloud is indicated by the ellipses. The number of repeating phenyl rings n equals 2, 3, 4, and 5 for naphthalene, anthracene, tetracene and pentacene, respectively.

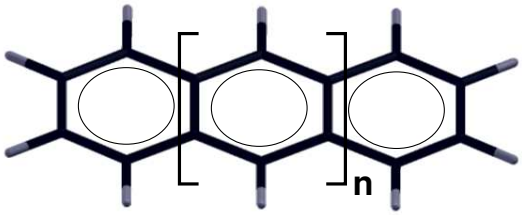

Figure 5.1: The anthracene (3A) molecule. The number of repeating phenyl rings is marked by n and equals 2, 3, 4, and 5, for naphthalene, anthracene, tetracene, and pentacene, respectively.

The oligo-acene crystals exhibit two specific structure features: One is the so-called *herringbone* stacking of the two inequivalent molecules in the (ab)-plane. Such a stacking is common for many organic molecular crystals [42] consisting of planar rod-like molecules. The second feature is the layered structure in the crystalline c-direction. Both are illustrated by means of anthracene in Fig. 5.2, which shows two projections of its crystalline structure. According to

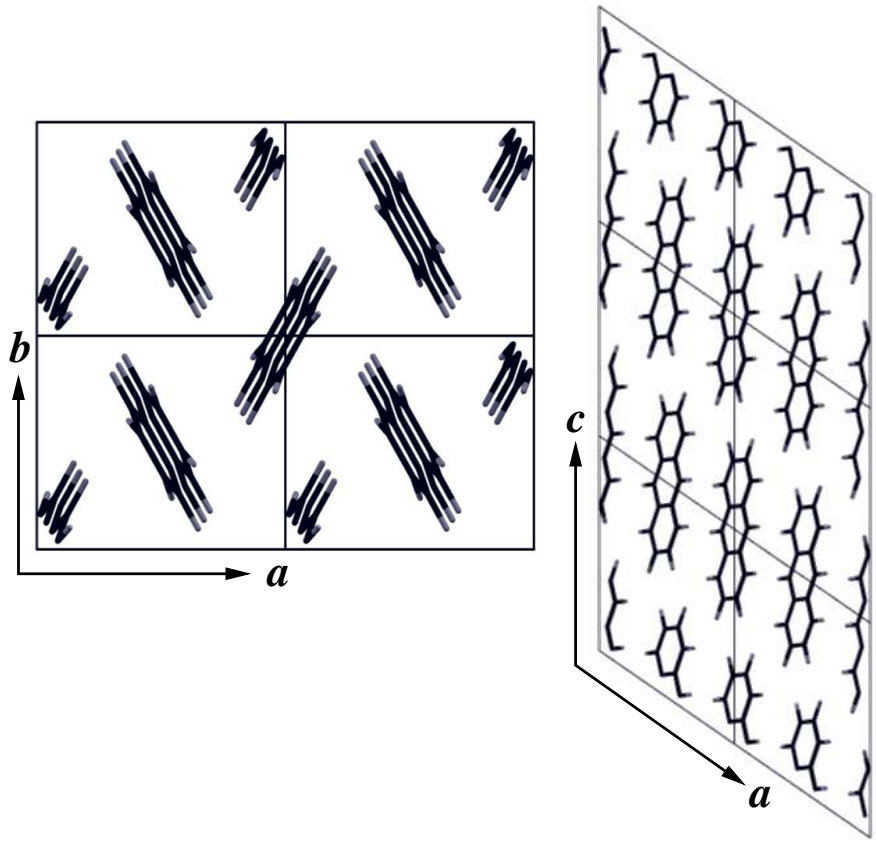

Figure 5.2: The projections of the anthracene crystal on the (ab)-plane (left) and the (ac)-plane (right) illustrate the herringbone stacking and the layered structure, respectively. The crystalline lattice constants are denoted by a, b, and c.

this completely different molecular arrangement in the (ab)-plane compared to the c-direction, the anisotropy of electro-optical properties can be understood. The distances between the molecules are shortest along the c-direction.

5.1.1 Lattice parameters at ambient pressure

In Tab. 5.1 the lattice parameters, as well as the unit cell volume V for the investigated series of oligo-acenes are listed [84–87]. Among them, 2A and 3A crystallize in a monoclinic structure, whereas 4A and 5A have a triclinic space group. The monoclinic systems are specified by three lattice constants a, b, and c as well as the monoclinic angle β. The monoclinic space group $P2_1/a$ consists of four symmetry operations, namely two screw axes, the inversion and the identity. The triclinic structures require six lattice parameters to be fully determined: a, b, and c as well as all three angles α, β, and γ, which are

Table 5.1: Lattice parameters of the oligo-acenes: Naphthalene (2A) [84], anthracene (3A) [85], tetracene (4A) [86], and pentacene (5A) [87].

	2A	3A	4A	5A
chemical formula	$C_{10}H_8$	$C_{14}H_{10}$	$C_{18}H_{12}$	$C_{22}H_{14}$
space group	$P2_1/a$	$P2_1/a$	$P\bar{1}$	$P\bar{1}$
a [Å]	8.235	8.562	7.98	7.93
b [Å]	6.003	6.038	6.14	6.14
c [Å]	8.658	11.184	13.57	16.03
α [deg]	90.0	90.0	101.3	101.9
β [deg]	122.9	124.7	113.2	112.6
γ [deg]	90.0	90.0	87.5	85.8
V [Å^3]	361.7	475.35	599.2	705.0

different from 90°. Concerning the symmetry operations, only the inversion and the identity remain in these structures. Remarkably, within this series the lattice constants a and b change only slightly, while the significant increase of c nicely correlates with the growth of the molecules when going from naphthalene to pentacene.

5.1.2 Lattice parameters of anthracene up to 10 GPa

The lattice parameters of anthracene up to 10 GPa that are summarized in Tab. 5.2 served as starting points for its internal structure optimizations as a function of pressure. At ambient pressure the lattice parameters observed at 290° K and the atomic positions listed in Tab. 1 (ii) of Ref. [85] have been used. The details of the X-ray powder diffraction experiments of anthracene under high pressure are given in Refs. [88–90].

When pressure up to 10 GPa is applied to anthracene the lattice constants are reduced, whereas the monoclinic angle increases. Despite these changes, the crystalline structure is stable and no phase transition is found up to 20 GPa [91]. The decrease of the lattice constants is different for a, b, and c. This can be traced back to the the anisotropic linear compressibility [92], which is highest in a-direction. Therefore, up to 10 GPa, the reduction of a is largest, which is 1.16 Å or 14% of its magnitude at ambient pressure. In contrast, b and c decrease by 9% and 6%, respectively. As we will see later, this anisotropic change in the lattice constants is also visible in the pressure dependence of the molecular orientation.

Table 5.2: Monoclinic lattice parameters a, b, c, β and the unit cell volume $V = a \cdot b \cdot c \cdot \sin\beta$ of anthracene as a function of pressure p. At ambient pressure the values have been taken from Ref. [85], the pressure data are from Ref. [88].

p [GPa]	a [Å]	b [Å]	c [Å]	β [deg]	V [Å^3]
0.0	8.510	6.027	11.162	124.63	475.35
1.1	8.117	5.850	10.886	125.29	421.94
2.5	7.893	5.753	10.759	125.75	396.50
3.1	7.828	5.724	10.724	125.87	389.32
4.0	7.733	5.679	10.669	126.02	378.96
6.1	7.572	5.601	10.592	126.48	361.23
8.0	7.444	5.533	10.517	126.81	346.85
10.2	7.347	5.483	10.470	127.07	336.55

5.2 Internal Geometry

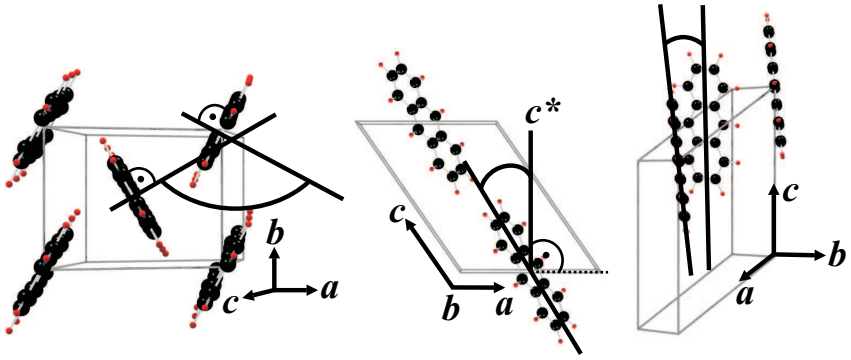

Figure 5.3: Three views of the crystal structure of anthracene illustrating the definition of the herringbone angle θ (left), the tilting angle χ, and δ (right), which served as the structure parameters for the internal geometry optimization. The crystalline axes are denoted with a, b, and c, respectively.

As already mentioned in Sec. 5.1, the intramolecular bonds (σ bonds) are typically rather rigid, whereas the intermolecular interactions are believed to be weak long-range vdW type. Due to the former, the displacements of the carbon atoms result in big atomic forces. In contrast, rotations of the rigid molecule are accompanied by much smaller total energy changes. Therefore the most effective procedure in theoretically determining the internal geometry turned out to consist of two steps. At the beginning, the internal molecular geometry has been optimized by minimizing the forces acting on each of the atoms to be

below 2 mRy/a.u. in magnitude. This procedure leads to the optimized bond lengths and angles within the molecules. Subsequently, the total energy has been minimized with respect to the molecular orientation defined by the angles θ, χ, and δ. This means, we search for the global energy minimum of the 3D energy surface $E = E(\theta, \chi, \delta)$. The definition of these angles is illustrated in Fig. 5.3. The herringbone angle θ quantifies the angle between the normal vectors of the molecular planes of two inequivalent molecules. The tilting angle of the long molecular axis with respect to the c^*-axis (perpendicular to the (ab)-plane) is denoted by χ. The angle between the long molecular axes of two inequivalent molecules is labeled δ.

By this definition, the variation of these angles corresponds to rotations of the rigid molecules. In order to handle the problem of the multi-dimensional energy surface, the herringbone angle θ has been optimized at fixed χ and δ first. Then the optimized θ has been kept constant and successively χ and δ have been varied. Once the three angles have been determined in a first cycle, the data have been refined by another iteration. In the first loop, these angles have been varied in steps of approximately one degree usually in the range plus to minus five degrees from the starting point. Whether this window was sufficiently large, has been checked once in case of the herringbone angle by a variation between zero and 180 degrees. The results of this analysis are depicted in Fig. 5.4 and clearly demonstrate that one energy global minimum exists, which can be more accurately determined by searching close to it in small steps. The internal geometry optimization was finished with a final

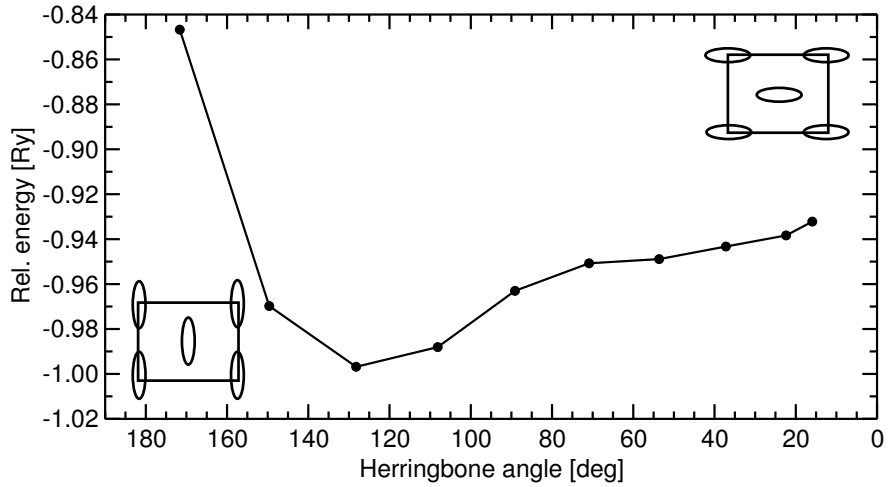

Figure 5.4: Variation of the herringbone angle in a window from 0 to 180 degrees. The sketches in the left and right corner illustrate the molecular arrangement in the (ab) plane, if θ equals 180 (left) and 0 (right) degrees, respectively.

relaxation of the atomic positions with the same accuracy as in the beginning.

Part II

Results and Discussion

6 Pressure Studies on Anthracene

For a long time I have considered even the craziest ideas about atom nucleus... and suddenly I discovered the truth.

Maria Goeppert-Mayer

In this chapter, the calculated pressure dependence of the internal geometry including bond lengths, shortest intermolecular distances and internal structure parameters, as well as the bulk modulus is presented. Moreover, the band structure, the density of states, and the optical absorption spectrum of anthracene are investigated as a function of the unit cell volume. By applying pressure to the crystal, the unit cell volume is reduced resulting in decreased intermolecular distances and therefore enhanced intermolecular interactions. By this procedure the importance of those interactions on the physical properties of anthracene has been studied exemplarily for organic molecular crystals.

6.1 Internal Geometry Optimization

6.1.1 Molecular orientation

Starting from the lattice parameters up to 10.2 GPa as listed in Sec. 5.1.2 the internal structure has been optimized within the LDA according to the procedure explained in 5.2. The obtained results for the three angles θ, χ and δ as a function of pressure are summarized in Tab. 6.1 and plotted in Fig. 6.1. The experimentally determined values for these quantities [88] are included in the figure for comparison. All three angles increase over the pressure region from 0 to 10.2 GPa in good agreement with experiment. It is found that the increase of θ is the dominating effect. By this change of the herringbone angle the translationally inequivalent molecules are aligned, i.e., they turn into a more parallel arrangement. Moreover, this variation is largest in the pressure range from 0 to 3 GPa, where θ raises by 12.6° and then slightly drops off up

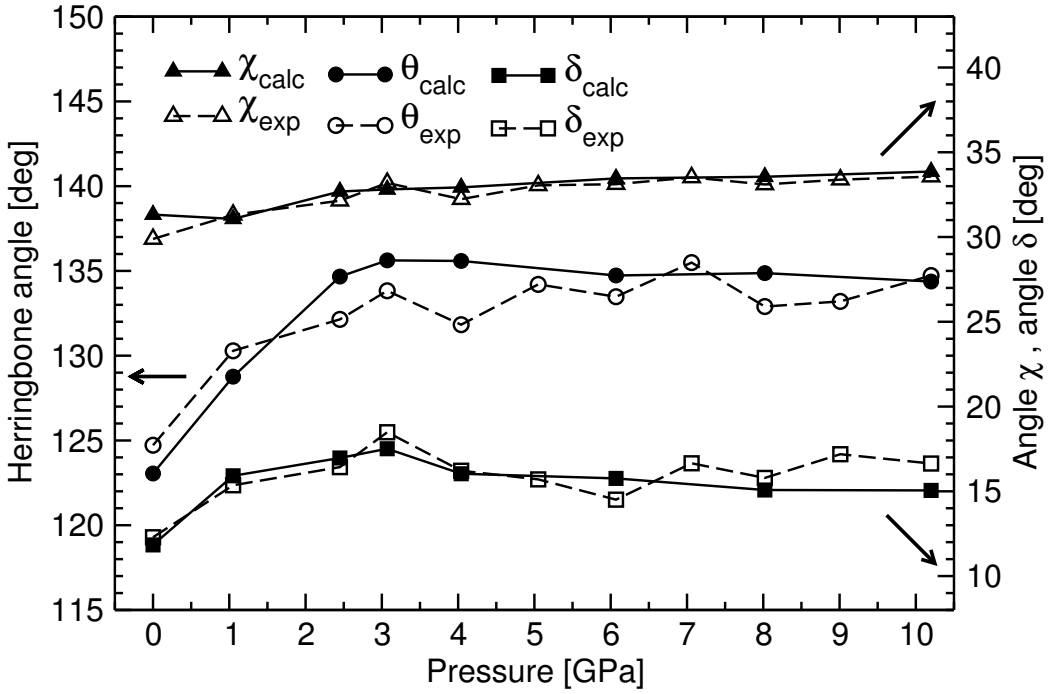

Figure 6.1: FP-APW+lo results (full lines with filled symbols): the angles θ, χ and δ are compared to the values refined from experiment (dashed lines with open symbols) [88] as a function of pressure.

Table 6.1: Calculated angles θ, χ, and δ in degrees as a function of pressure p. The lattice parameters as summarized in 5.1.2 served as input parameters for these calculations.

	LDA		
p [GPa]	θ [deg]	χ [deg]	δ [deg]
0.0	123.05	31.32	11.837
1.1	128.76	31.07	15.914
2.5	134.67	32.69	16.968
3.1	135.62	32.81	17.511
4.0	135.59	32.93	16.038
6.1	134.73	33.46	15.763
8.0	134.87	33.55	15.076
10.2	134.38	33.86	15.054

to 10.2 GPa. δ has a similar trend, but exhibits changes smaller in magnitude, which are +5.7° between 0 and 3 GPa. In contrast, χ increases by only 2.5° up to a pressure of 10.2 GPa. It can be argued that the behavior of χ and δ is due to the reduction of the lattice parameter c and the associated decrease of the layer distance, while the variation of θ is caused by the decrease of the lattice parameter a [88]. Therewith the distinct pressure influence on θ is explained, since the pressure induced change of a is largest as already pointed out in the previous chapter. The argument that interchain interactions are responsible for the pressure effect on δ was proven by total energy calculations for unit cells with elongated c-axes. Starting from the crystal structure at ambient pressure with c=11.162 Å, the c-axis has been increased by 1 and 2 Å. Subsequently the angle δ has been varied between 6° and 18°. The resulting total energies are shown in Fig. 6.2. In case of c=12.162 Å , the stretching of the c-axis raises the shortest HH-distance from 2.4 Å to 3.4 Å. This HH-distance is defined as the separation between particular end-hydrogen atoms of neighboring molecules in c-direction. For c=13.162 Å , the corresponding value of 4.4 Å is obtained for this quantity. Up to an HH-distance of approximately 4 Å the interchain interaction is important and a total energy minimum is found for δ=12°. For larger layer distances the energy changes become smaller and no global energy minimum exists in the considered range.

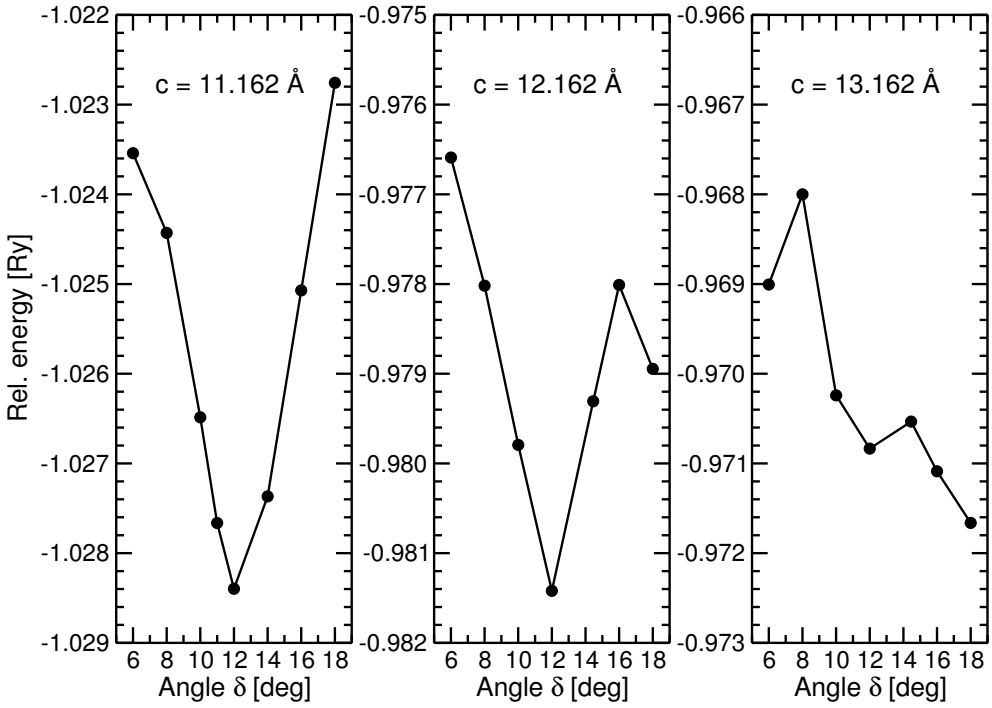

Figure 6.2: Total LDA energy as a function of δ calculated for monoclinic unit cells with c=11.162 Å (left), c=12.162 Å (middle), and c=13.162 Å (right panel), respectively.

6.1.2 Bond lengths and intermolecular distances

The fully optimized internal structures have also been analyzed in terms of intermolecular distances and bond lengths. Due to the rigidity of the molecules the decrease in CC-bond and CH-bond lengths turned out to be in the range of mÅ in the whole pressure region. Therefore the anthracene molecules themselves do not significantly change with pressure. In contrast, the shortest intermolecular CH- and HH-distances, which are the distances between end-hydrogen atoms and C or H atoms of the neighboring molecule in c-direction, decrease by several hundreds of mÅ . These findings are illustrated in Fig. 6.3 and confirm the expected result that the intramolecular interactions (covalent σ and π bonds inside the molecules) are less sensitive to pressure than the intermolecular interactions. Between 0 and 10.2 GPa a decrease in CC-bond and CH-bond lengths of 1-15 mÅ is found, whereas the shortest intermolecular CH- and HH-distances reduce by 630 mÅ and 420 mÅ, respectively.

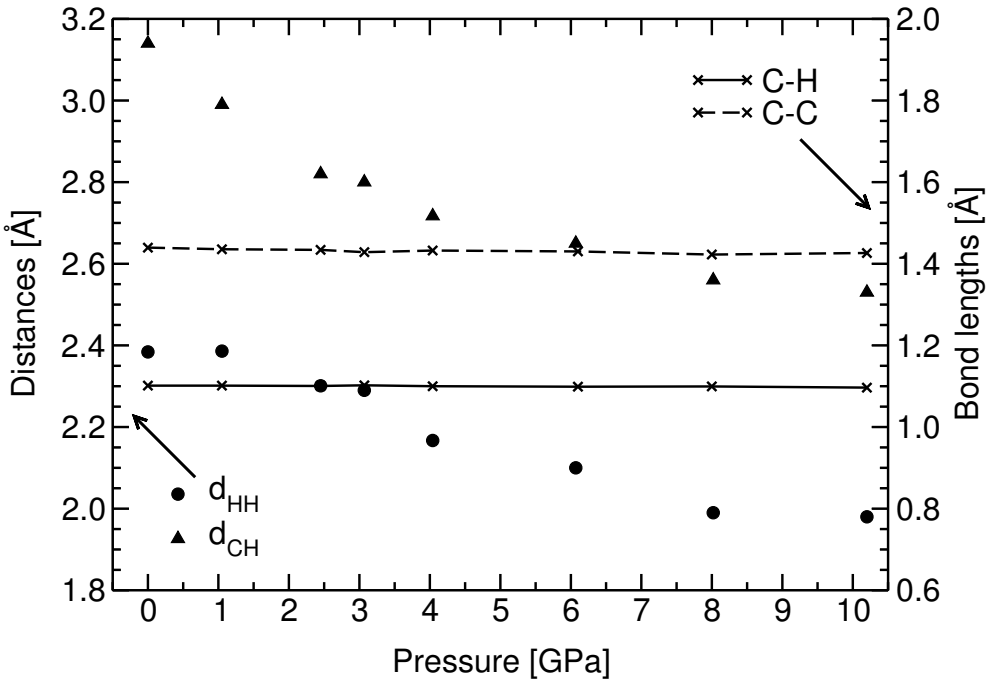

Figure 6.3: The shortest intermolecular distances between end-hydrogen atoms and C (d_{CH}, triangles), respectively H atoms (d_{CH}, circles), as well as the largest CC (dashed line) and CH (full line) bond lengths as a function of pressure.

6.1.3 LDA results compared to GGA findings

To analyze how sensitively the three internal structure parameters θ, χ and δ depend on the approximation for the xc potential, the internal structure optimization has been carried out using both, the LDA and the GGA. For the reason given in Sec. C.1, the underlying lattice parameters as a function of pressure up to 4 GPa originate from a different experimental data set. In Tab. 6.2 the GGA findings are compared to the values obtained by LDA calculations. The GGA results turned out to be very similar to the LDA findings. The GGA

Table 6.2: Calculated angles θ, χ, and δ in degrees as a function of pressure p. The underlying lattice parameters up to 4 GPa originate from a different experimental data set as explained in Sec. C.1.

	LDA			GGA		
p [GPa]	θ [deg]	χ [deg]	δ [deg]	θ[deg]	χ [deg]	δ [deg]
0.0	123.05	31.32	11.84	123.62	30.77	11.94
0.5	128.71	32.49	15.61	130.58	30.05	12.79
1.3	129.36	31.26	15.01	130.34	31.36	14.96
2.1	134.53	32.79	16.80	134.96	32.73	16.77
2.9	134.11	33.08	16.25	134.93	33.12	16.80
3.8	134.47	33.63	17.38	134.90	33.59	16.96

also yields an overall increase of the three angles as a function of pressure and the trend obtained with the LDA is fully reproduced.

6.1.4 Isothermal bulk modulus

The isothermal bulk modulus B is given by the equation:

$$B(V) = -V\frac{\partial p}{\partial V} = V\frac{\partial^2 E}{\partial V^2}. \tag{6.1}$$

Birch [93] derived an equation of state (EOS) for calculating B from the total energy E as a function of volume V:

$$\begin{aligned} E(V) &= E_0 + \frac{9}{8}B_0V_0\left(\left(\frac{V_0}{V}\right)^{\frac{2}{3}} - 1\right)^2 \\ &+ \frac{9}{16}B_0V_0(B_0^{'} - 4)\left(\left(\frac{V_0}{V}\right)^{\frac{2}{3}} - 1\right)^3 \\ &- \sum_{n=1}^{N}\gamma_n\left(\left(\frac{V_0}{V}\right)^{\frac{2}{3}} - 1\right)^n, \end{aligned} \tag{6.2}$$

where B_0 and V_0 denote the isothermal bulk modulus and the equilibrium volume at ambient pressure, respectively. $B_0^{'}$ and γ_n are the first and higher order derivatives of B_0. In Eq. (6.2) the inclusion of higher order terms, which is limited by the number of data points available for fitting the parameters $B_0^{'}$ and γ_n, crucially influences the result for the isothermal bulk modulus at ambient pressure B_0. For consistency, a Birch EOS excluding terms with the power greater than three has been used for all fits. Starting from the LDA total energies E versus unit cell volume V, B_0 and the first derivative $B_0^{'}$ have been calculated. Then the same fit has been applied to the experimental data set (p versus V). For comparison to the experimental counterparts we also derive the theoretical pressure as $p = -\frac{\partial E}{\partial V}$. The volume dependence of the isothermal bulk modulus is then obtained from the fitted function. Figure 6.4 summarizes the results of

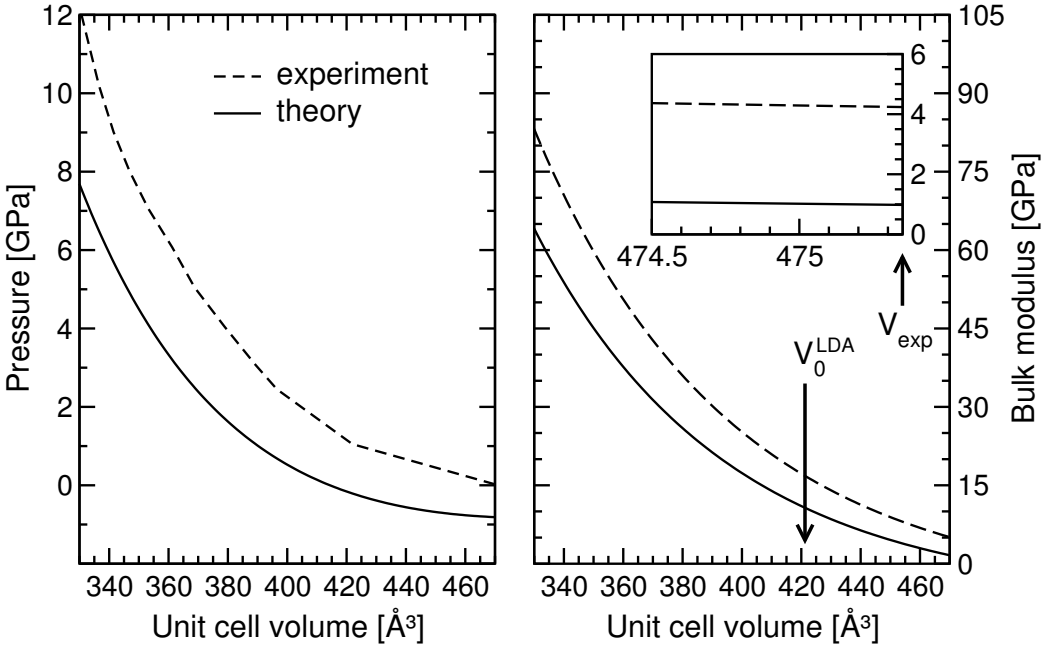

Figure 6.4: The pressure as a function of volume calculated by a fit (Eq. (6.2)) of the theoretical data set (full line) and the experimental data set (dashed line, Tab. 5.2) is shown in the left panel. In the right panel the isothermal bulk modulus versus volume for these two data sets resulting from the fit function is plotted. In the inset the focus is put on the region at the true equilibrium volume ($V_{exp} = 475.35$ Å^3). V_0^{LDA} marks the LDA equilibrium volume.

this analysis. In the left panel, the theoretical and the experimental pressure data as a function of volume are compared. The theoretical curve is shifted with respect to the experimental one, but the pressure dependence of the volume is reproduced. This shift is due to the underestimation of the equilibrium by the LDA potential and will be further discussed below. Since the energy dependence on the volume is not parabolic, the pressure is not linearly related

to V. Hence, the bulk modulus strongly depends on the particular volume, for which it is evaluated. This fact is evident in the right panel of Fig. 6.4, where the bulk modulus as a function of volume is depicted. For example, B_0 and its derivative B_0' calculated at the true equilibrium volume V_{exp} using both, the theoretical and experimental fit functions at ambient pressure are found to be 0.98 and 4.24 GPa, respectively. This is further illustrated in the inset of the right panel in Fig. 6.4. The corresponding values for B_0' are 9.66 and 15.97 GPa. Moreover, the LDA as well as the GGA are not able to reproduce the true equilibrium volume V_{exp}, but suggest different volumes for the stable crystal. For comparison, the LDA equilibrium volume V_0^{LDA} combined with the theoretical fit function suggests B_0 to be equal 12.61 GPa, while the analogous treatment using the GGA data yields 15.98 GPa. Besides, by using different types of EOS for fitting the experimental data B_0 values between 5.34 and 11.49 GPa have been obtained [91, 94]. Thus the LDA and the GGA bulk modulus are significantly overestimated. All these discrepancies reflect that such organic materials are soft and thus related to small energy differences upon modification. Therefrom and due to the reasons given above it is clear that different EOS as well as the usage of different xc potentials can only reproduce B_0 in its order of magnitude, but not an unambiguous value.

6.1.5 Discussion

As already stressed in Sec. 2.3.1, the LDA suffers from the overbinding effect that is responsible for the underestimation of the equilibrium volume and the overestimation of the bulk modulus. This major drawback has been encountered here. For the reasons given in Sec. 2.3.1 it could be argued that the overbinding of the LDA potential compensates for the missing VdW force and therefore leads to reasonable results concerning the internal geometry, which needs to be verified. According to Tab. 6.2 the LDA and the GGA yield similar internal structure parameters. This gives rise to the conclusion that the internal geometry does not significantly depend on the xc potential used. Since the theoretical results are reproduced by the Rietveld refinement of experimental data (Fig. 6.1), it is further concluded that the LDA, as well as the GGA, are able to correctly describe the internal structure of organic molecular crystals. Therefore, the reliability of such methods within DFT for these investigations is confirmed. On the other hand, if the VdW forces were the *glue* between neighboring molecules and the LDA compensated for this interaction, it would be expected that GGA does not give a stable crystal at all. For this reason, the LDA and the GGA total energies as a function of the unit cell volume have been analyzed. The LDA predicts the theoretical equilibrium volume V_0^{LDA} at 422 Å^3, which is 11% smaller than the experimental volume at ambient pressure V_{exp}. In contrast, a parabolic fit of the GGA total energies corresponding to the con-

tracted structures suggests an equilibrium structure with a volume larger than $V_{\rm exp}$, which remains to be proven. For this purpose the lattice parameters and the three angles specifying the internal geometry have been extrapolated in order to obtain good starting geometries for the expanded structures with unit cell volumes increased by 4, 7, 14, and 24%, respectively. For details on this procedure it is referred to Appendix C. The structure optimization has followed the same approach as explained in Sec. 5.2. The resulting optimized internal geometry reasonably follows the trend of the extrapolation of the pressure data. The GGA total energies as a function of unit cell volume for the pressure data (dots) and the hypothetical structures (open circles) are shown in Fig. 6.5.

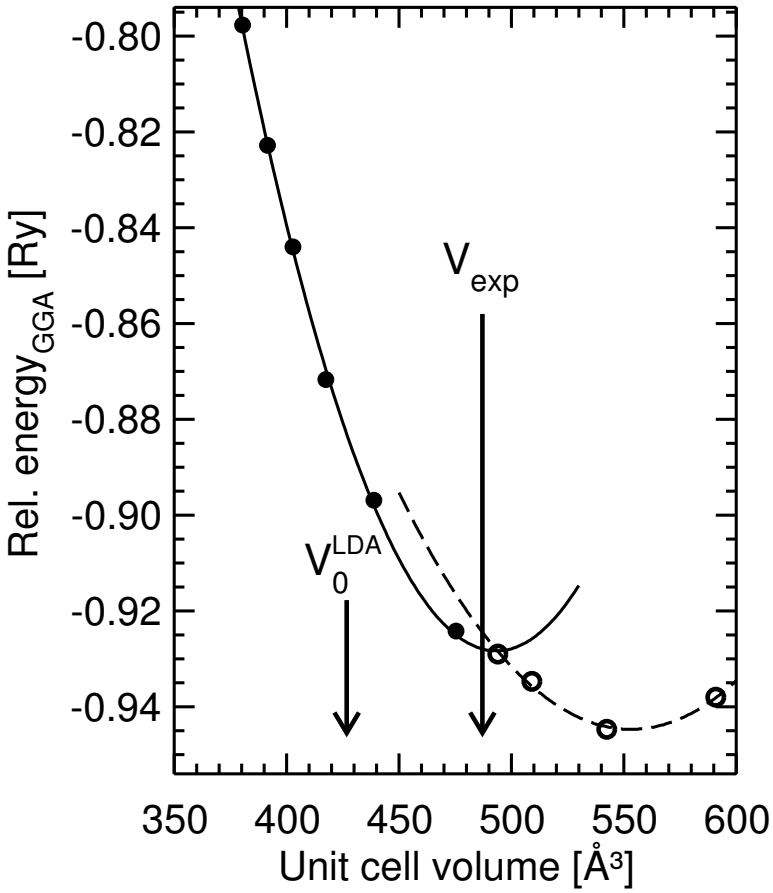

Figure 6.5: The calculated relative GGA energies [Ry] as a function of the unit cell volume [Å^3]. The full symbols denote the pressure data, whereas the open symbols correspond to hypothetical structures with a unit cell volume increased by 4, 7, 14, and 24%, respectively, obtained by extrapolating the lattice parameters as well as the angles θ, χ, and δ. The arrows indicate the LDA and the experimental equilibrium volume.

From this procedure one can conclude that the GGA is also able to yield a bound crystal, but with an equilibrium volume 16% larger than the experimental one. However, since the values corresponding to the expanded volumes rely on the assumption that such an extrapolation is valid and also slightly deviate from a parabolic fit, they are not completely convincing. For additional information the electron densities calculated with the LDA and the GGA, which are discussed in the next section, have been analyzed.

6.1.6 Summary

Up to here, several conclusions have been derived on the basis of the ab-initio investigation of the internal geometry of anthracene under high pressure. Here, they are once more concisely summarized:

- In accordance with the pressure dependence of the lattice parameters, the three angles determining the molecular orientation change under pressure, which turned out to be in good agreement with experimental findings.
- Concerning the internal geometry, both xc functionals, the LDA and the GGA are able to reproduce the experimental results, which gives rise to the conclusion that such investigations can rely on these functionals.
- However, the LDA and the GGA do not yield the true equilibrium volume. The former underestimates it, whereas the latter, even though it is not expected for vdW bound crystals, suggests a stable crystal, but with an overestimated volume.
- The volume as a function of pressure deviates from a parabolic relation resulting in a strong non-linear dependence of the bulk modulus on the volume. This reflects the softness of such materials. Therefore, and due to uncertainty in the LDA and the GGA equilibrium volumes the calculated values for the bulk modulus are not clear without any ambiguity.

6.2 Electronic Properties

Based on the crystal structures optimized with respect to the internal molecular orientation the electronic band structures, the electron DOS, and the electron densities of anthracene have been calculated up to 10.2 GPa.

6.2.1 Band structure and DOS

The main features of the band structure of anthracene are anisotropic band dispersion and band splitting, which are 3D effects and originate from the overlap of the π-wavefunctions of neighboring molecules. Both are a measure for the intermolecular interactions. Particularly, band splitting is due to the two translationally inequivalent molecules per unit cell and causes the *Davydov doublets* present in the excitation spectra of anthracene [95]. Since it has been found that the intermolecular distances are reduced and thus the intermolecular interactions are enhanced with increasing pressure, both, band splitting and band dispersion are expected to increase accompanied by a broadening of the density of states. These effects are apparent in the band structure and total DOS presented in Figs. 6.7, 6.8, and 6.9. The calculation of the band structures have been carried out following a $\mathbf{k}$-path connecting high symmetry points in the IBZ as illustrated in Fig. 6.6. The internal coordinates of these points Γ, Y, Z, A, B, and K in units of ($\frac{2\pi}{a}$, $\frac{2\pi}{b}$, $\frac{2\pi}{c}$) are (0,0,0), (0.5,0,0), (0,0,0.5), (0.5,0.5,0), (0,0.5,0), and (0.4,0,0.2), respectively.

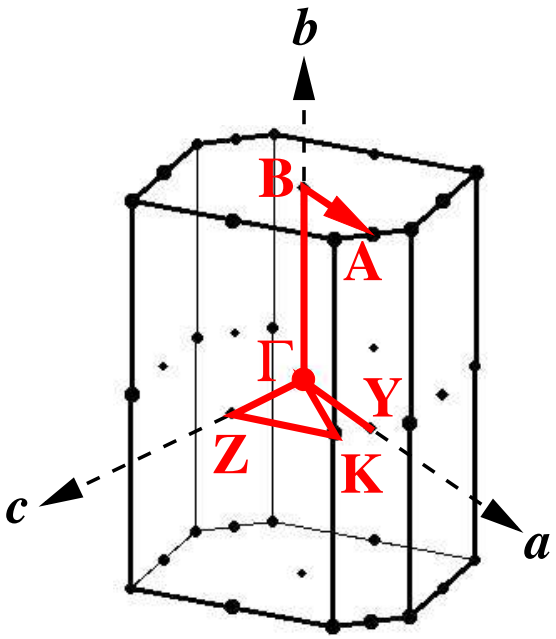

Figure 6.6: $\mathbf{k}$-path used for the band structure calculations of anthracene under pressure. The internal coordinates of these points Γ, Y, Z, A, B, and K in units of ($\frac{2\pi}{a}$, $\frac{2\pi}{b}$, $\frac{2\pi}{c}$) are (0,0,0), (0.5,0,0), (0,0,0.5), (0.5,0.5,0), (0,0.5,0), and (0.4,0,0.2), respectively.

As a matter of symmetry, the bands are degenerate at Y and B, i.e., at the zone boundaries of the IBZ in the a- and b-direction, respectively, as well as along $\overline{\mathrm{BA}}$. This finding is in agreement with earlier calculations performed by KATZ

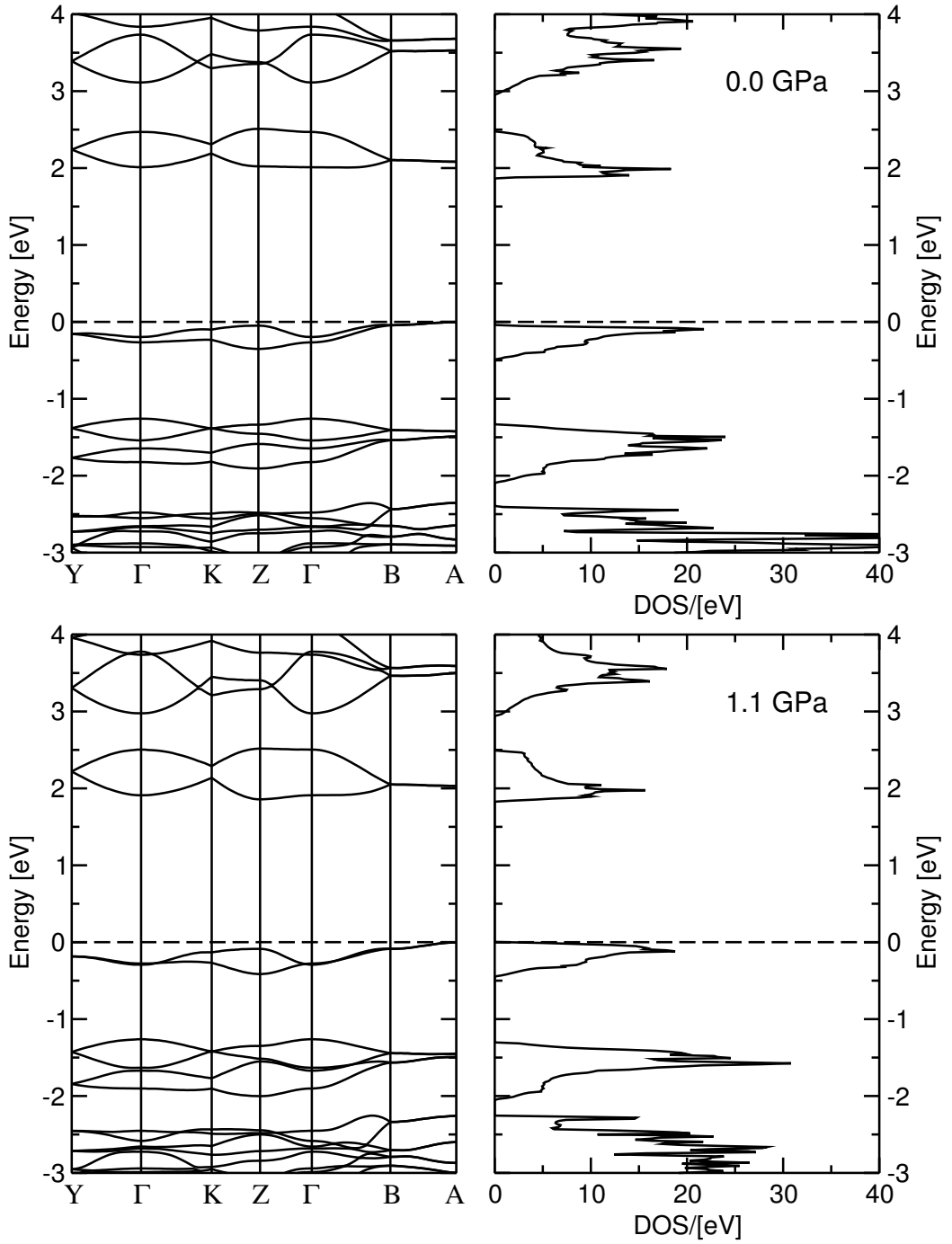

Figure 6.7: Band structure E($\mathbf{k}$) (left) and DOS (right) of anthracene at ambient pressure and 1.1 GPa, respectively. In each case the Fermi level is indicated by a dashed line.

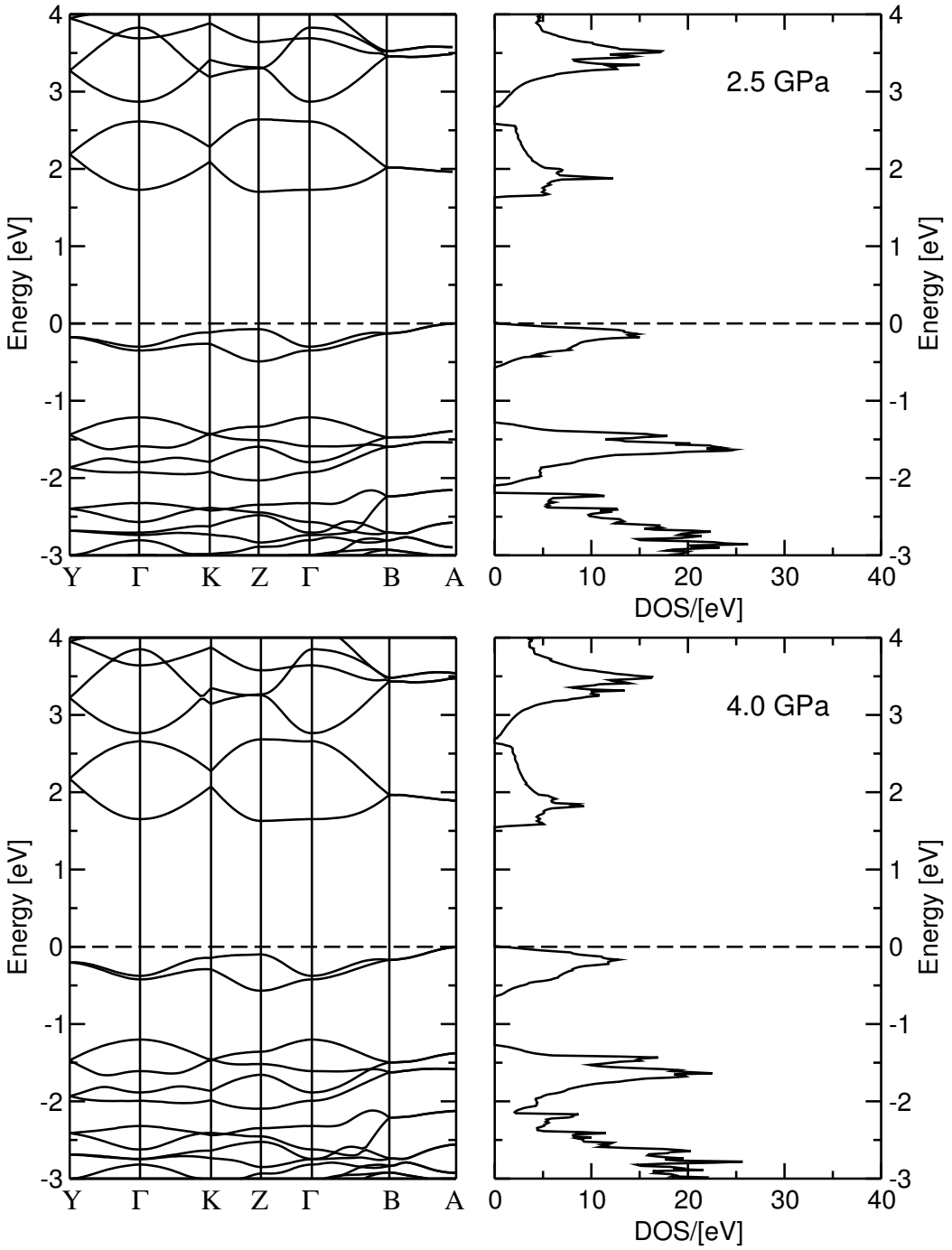

Figure 6.8: Band structure E(k) (left) and DOS (right) of anthracene at 2.5 and 4.0 GPa, respectively. In each case the Fermi level is indicated by a dashed line.

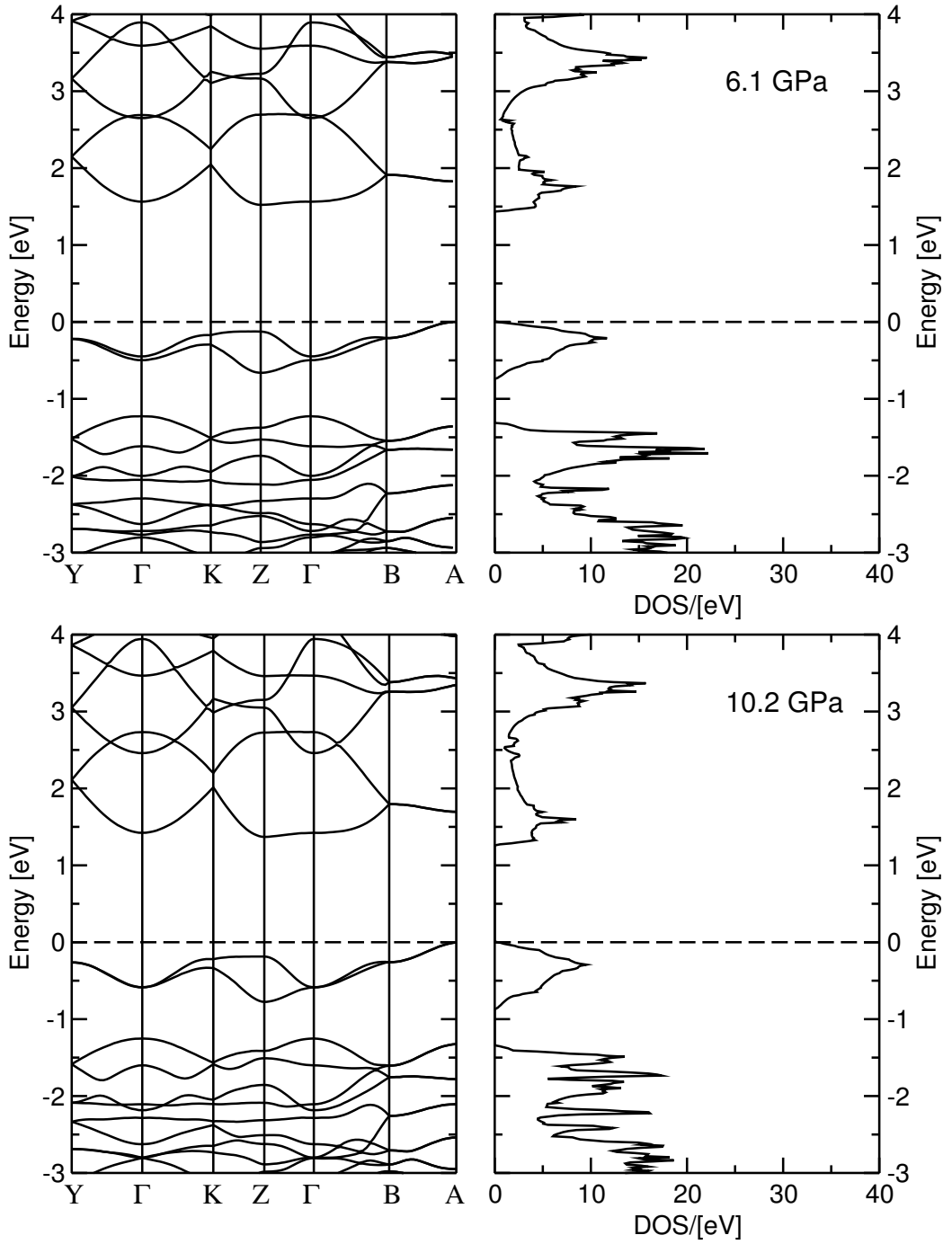

Figure 6.9: Band structure E(k) (left) and DOS (right) of anthracene at 6.1 and 10.2 GPa, respectively. In each case the Fermi level is indicated by a dashed line.

et al. [96] and by SILBEY et al. [97, 98]. While upon pressure the symmetry and thus the degeneracy of the bands in this parts of the band structure is not changed, the band splitting becomes large at the zone center, along $\overline{\Gamma Z}$ and $\overline{KZ}$. However, the intermolecular interactions are anisotropically altered with pressure due to the non-uniform pressure dependence of the lattice parameters [88]. Therefore, the increase in band widths and band splitting is strongly direction dependent. Fig. 6.10 shows the band splitting of the band pairs closest to the Fermi level as a function of pressure at Γ and Z. In the following, the valence and the conduction band pair are abbreviated with VB and CB, respectively. In addition, a subscript is introduced, which denotes the sequence of the single bands within this pairs downwards or upwards in energy from the Fermi level, respectively. Both, VB and CB, exhibit maximum band splitting

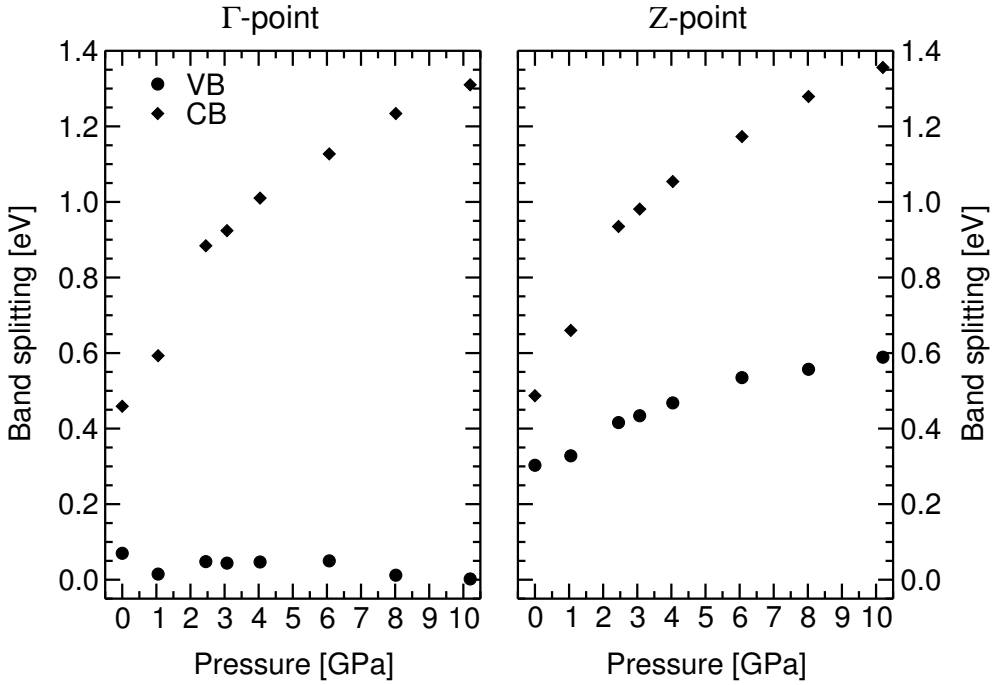

Figure 6.10: Band splitting of the highest VB (dots) and the lowest CB (diamonds) evaluated at Γ (left) and Z (right) as a function of pressure.

at the Z-point, which is 0.30 eV and 0.49 eV, respectively. The band splitting increases upon pressure. For example at Z and 10.2 GPa, it is 0.6 eV for VB, while the bands of CB differ by 1.36 eV. This effect is apparent in the whole band structure, except for VB at Γ, where VB_1 and VB_2 are almost degenerate at 10.2 GPa.

Table 6.3 summarizes the band widths of CB_1, VB_1, and VB_2 evaluated in the directions $\overline{\Gamma Y}$, $\overline{\Gamma B}$, $\overline{\Gamma Z}$, and $\overline{\Gamma K}$ for the investigated pressure region, which are

Table 6.3: Calculated band widths [meV] of the bands close to the Fermi level (CB_1, VB_1, and VB_2) analyzed in the directions $\overline{\Gamma Y}$, $\overline{\Gamma B}$, $\overline{\Gamma Z}$, and $\overline{\Gamma K}$ as a function of pressure [GPa].

[GPa]	0.0	1.1	2.5	4.0	6.1	8.0	10.2
$\overline{\Gamma Y}$:							
CB_1	230	308	460	522	587	643	691
VB_1	40	91	124	172	227	295	322
VB_2	111	107	172	218	276	307	325
$\overline{\Gamma B}$:							
CB_1	94	141	287	314	350	358	372
VB_1	153	193	171	206	238	286	325
VB_2	224	207	219	253	287	298	327
$\overline{\Gamma Z}$:							
CB_1	11	52	26	22	40	45	53
VB_1	148	190	225	277	322	372	398
VB_2	85	122	143	145	164	173	188
$\overline{\Gamma K}$:							
CB_1	179	227	363	422	486	543	592
VB_1	97	145	182	231	275	340	365
VB_2	35	24	85	130	203	222	251

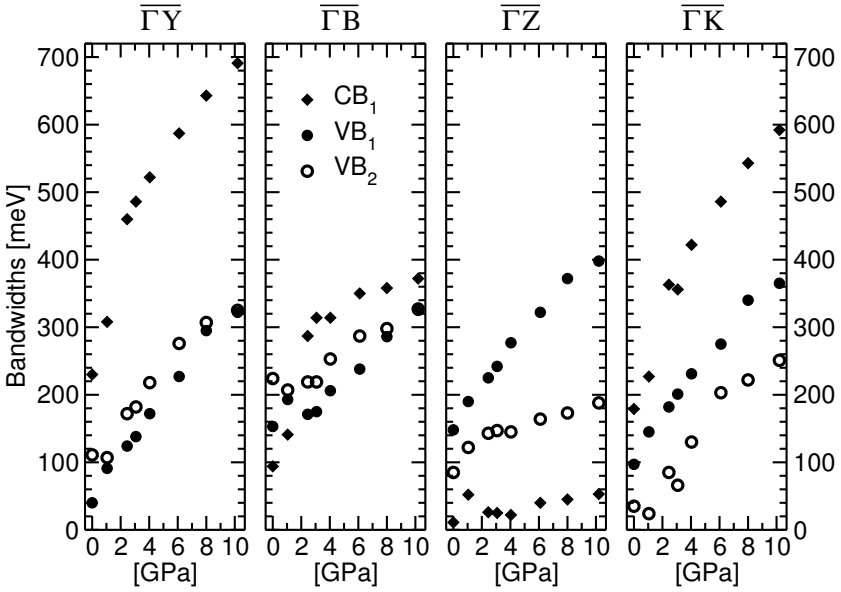

Figure 6.11: Band widths of CB_1, VB_1, and VB_2 evaluated in the directions $\overline{\Gamma Y}$, $\overline{\Gamma B}$, $\overline{\Gamma Z}$, and $\overline{\Gamma K}$ as a function of pressure.

graphically shown in Fig. 6.11. The increase of the band widths with pressure is largest along $\overline{\Gamma\mathrm{Y}}$ for all bands. This is in accordance with the pressure dependence of the lattice parameter a, which is affected most by pressure [88]. The maximum gain in band width for VB_1 and CB_1 with pressure is 0.28 eV and 0.46 eV, respectively. At ambient pressure the band dispersion of CB_1 is highest in $\overline{\Gamma\mathrm{Y}}$, which is perpendicular to the long molecular axis and parallel to the herringbone stacking direction. Since the charge carrier mobility is inversely dependent on the effective mass and thus proportional to the band width, the electron carrier mobility is largest in the crystalline a-axis. This remains unchanged up to high pressures. In contrast to the electron conduction at ambient pressure, theory suggests $\overline{\Gamma\mathrm{B}}$ and $\overline{\Gamma\mathrm{Z}}$ as the favored channels for hole carriers. However, with increasing pressure the gain in band width of VB_1 becomes more pronounced along $\overline{\Gamma\mathrm{Z}}$ and thus the hole conduction is supposed to be largest in the direction of the long molecular axis from approximately 3 GPa on. Comprising these results allows to conclude that the pressure effect on the band widths is opposite to that caused by raising temperature, which localizes the charge carriers in well confined bands with small band widths resulting in large effective charge carrier masses.

In order to gain insight into the origin of the different band dispersion and band splitting properties the electron densities have been calculated, which are discussed below.

6.2.2 The band gap

Before the electronic band gap from the band structure as a function of pressure is extracted, some fundamentals according energy gaps are recalled, which are also important for the discussion of the optical properties later in this chapter. When talking about energy gaps, it must be clearly distinguished between the electronic band gap E_g and the *optical* gap Δ_g. The former is defined as the energy difference between the lowest conduction band minimum and the uppermost valence band maximum. If these two extrema exist at the same $\mathbf{k}$-point, the band gap is further specified as *direct* band gap. When this condition is not fulfilled, one talks about an *indirect* band gap. The electronic band gap E_g is also called *fundamental* gap. In contrast, the *optical* gap Δ_g measures the energy of the lowest direct transition that is allowed by the dipole-dipole selection rules and thus optically active. This does not necessarily have to be the lowest direct band gap.

At ambient pressure, the LDA band gap $E_\mathrm{g}^\mathrm{LDA}$ in anthracene turned out to be an indirect gap of 2 eV. For comparison, the lowest direct band gap appears at the A-point (see Fig. 6.6) and is only 0.1 eV larger than the indirect one. These values are underestimated compared to experimental findings due to

the overbinding of the LDA. Experimental results of intrinsic photoconductivity measurements for the anthracene crystal are reported in Ref. [92]. Therein, an averaged experimental value for E_{g} equal to 3.9$\pm$0.1 eV is proposed. Besides theses experimental findings, calculations, which are based on the experimentally determined ionization and polarization energies yield values ranging from 3.75 eV to 4.2 eV [92]. From this it is concluded, that the energy gap of crystalline anthracene is 4.0 eV within an accuracy of $\pm$0.2 eV. In order to make the $E_{\mathrm{g}}^{\mathrm{LDA}}$ consistent with experiment, it is necessary to account for the self-energy correction Δ_{c}. The exact value for the self-energy could be obtained by GW calculations. To my knowledge, this has not been done for crystalline anthracene yet, since this is computationally very demanding. An alternative is the comparison of $E_{\mathrm{g}}^{\mathrm{LDA}}$ to the experimentally determined electronic band gap. Regarding the experimental findings quoted above, the calculated $E_{\mathrm{g}}^{\mathrm{LDA}}$ is approximately 50% to small. Therefore, a scissors operator Δ_{c} of 2.0$\pm$0.2 eV is required.

If pressure is applied to anthracene, the LDA band gap $E_{\mathrm{g}}^{\mathrm{LDA}}$ of anthracene is reduced by pressure. This is a consequence of the increase in the band widths, which has already been previously discussed. The pressure effect on $E_{\mathrm{g}}^{\mathrm{LDA}}$ is illustrated in Figure 6.12 representing the LDA findings that are additionally summarized in Tab. 6.4.

Table 6.4: The uncorrected LDA band gap $E_{\mathrm{g}}^{\mathrm{LDA}}$ of anthracene extracted from the band structure as a function of pressure.

p [GPa]	0.0	1.1	2.5	3.1	4.0	6.1	8.0	10.2
$E_{\mathrm{g}}^{\mathrm{LDA}}$ [eV]	2.01	1.86	1.70	1.67	1.63	1.52	1.44	1.37

Unfortunately, there are no experimental data available for the pressure dependence of E_{g} of crystalline anthracene. Therefore, the Δ_{c} as a function of pressure is not known. Since it is not a priori clear, whether the scissors operator is pressure independent or not, the analysis of the pressure effect on the band gap has been done without any correction of the LDA conduction band energies.

According to the non-uniform pressure dependence of the structural properties, the energy gap reduction is more strongly pronounced in the low pressure range compared to the high pressure region. In the former as well as in the latter, the data points suggest a linear relationship between $E_{\mathrm{g}}^{\mathrm{LDA}}$ and pressure. When applying a linear fit to the lower and upper pressure range, respectively, the average decrease of $E_{\mathrm{g}}^{\mathrm{LDA}}$ up to 3 GPa is -0.1 eV/GPa and -0.04 eV/GPa from 3 to 10.2 GPa. Note, this is only a rough estimate, which is based on

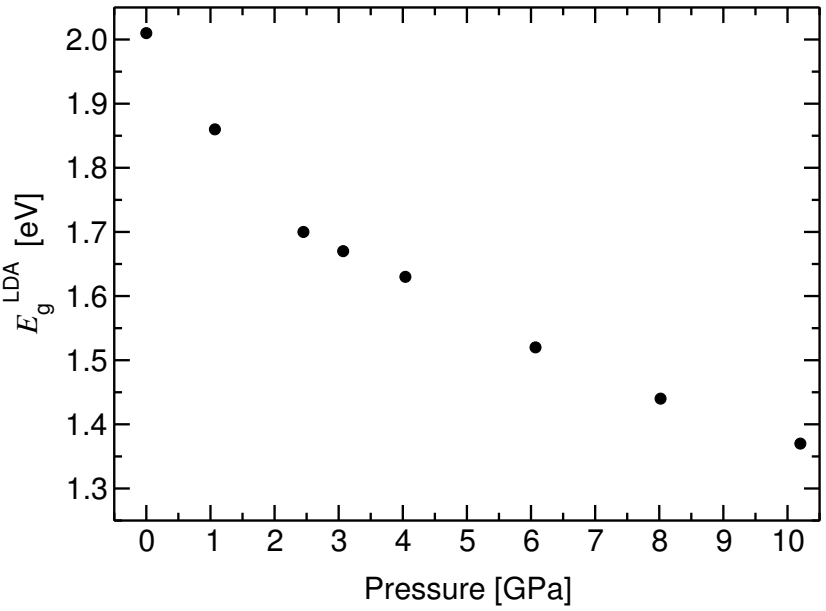

Figure 6.12: Plot of the uncorrected LDA band gap $E_{\mathrm{g}}^{\mathrm{LDA}}$ of anthracene deduced from the band structure as a function of pressure.

the assumption that the self-energy correction is constant over the whole pressure region. As it will be seen later, it turned out that Δ_{c} is indeed pressure dependent.

6.2.3 Electron densities

The previously presented band structures revealed a very anisotropic pressure effect on the bands close to the Fermi level, e.g., on VB_1 and VB_2 along $\overline{\Gamma\mathrm{KZ}}$. The central topic of this section is the spatial variation of the contributions to the electron density calculated for CB_1 VB_1, and VB_2 as a sum over 40 $\mathbf{k}$-points along $\overline{\Gamma\mathrm{KZ}}$ at different pressure values. The results obtained for the (ab)-plane at different z-coordinates are plotted in Fig. 6.13 for ambient pressure and 10.2 GPa, respectively. These density distributions evidence the enhancement of the intermolecular interactions with pressure. The *bonding* states CB_1 and VB_2 significantly raise the π-electron density in the interstitial region, which is in contrast to the *antibonding* band VB_1. While they are rather similar at ambient pressure, VB_1 exhibits a highly diminished electron density between neighboring molecules at 10.2 GPa compared to its *bonding* counterpart VB_2, which leads to its localized behavior. This explains the decrease in dispersion of VB_1 in contrast to the increase of VB_2 in this part of the band structure.

Another interesting feature is the electron distribution in the interstitial. It is

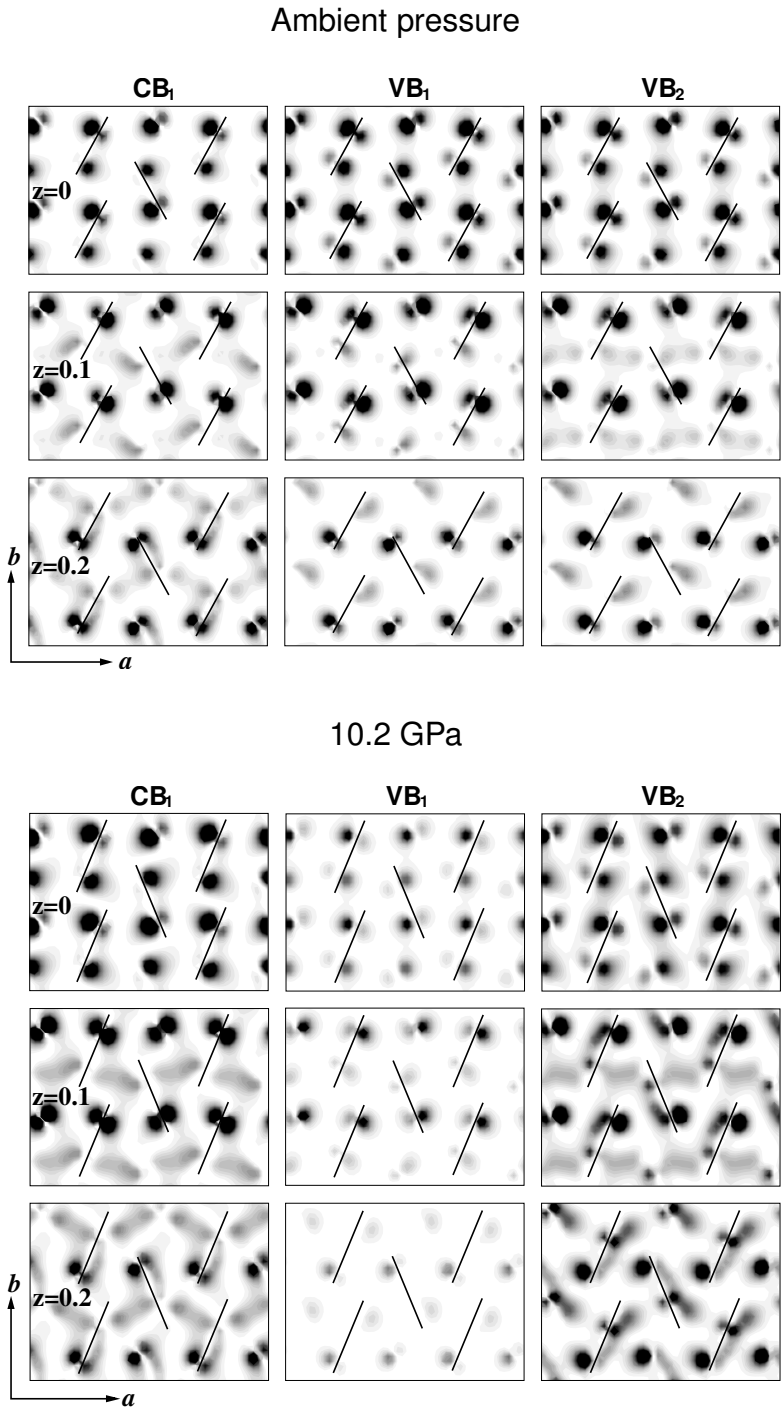

Figure 6.13: The LDA 2D electron density plots of CB_1, VB_1, and VB_2 in the (ab)-plane calculated as sum over 40 $\mathbf{k}$-points along $\overline{\Gamma\mathrm{KZ}}$ for different z-coordinates in units of c at ambient pressure and 10.2 GPa, respectively. The thin solid lines indicate the molecules to illustrate the herringbone arrangement in anthracene. The dark regions correspond to high density and vice versa.

supposed that the herringbone arrangement of the molecules favors the maximum overlap of the π-wavefunctions. With increasing pressure the molecules orient in such a way that this overlap can be sustained. Similar results have been obtained for biphenyl [78, 99].

6.2.4 Conclusions

The conclusions drawn from the results presented in this section are summarized as follows:

- This study clearly evidences that applying pressure anisotropically enhances the intermolecular interactions in anthracene. Consequently,
  - the band dispersion and splitting are increased.
  - the band gap is reduced.
  - the optical gap is expected to decrease accordingly, which should result in a red-shift of the lowest optical transitions.
- Due to the anisotropy of the band structure the favored channels for electron and hole conduction are found to be along different crystalline directions.
- The electron densities calculated within the LDA exhibit significant contributions between the molecules, which are raised with pressure.
- This LDA electron densities are completely reproduced by the analogous GGA calculations at ambient pressure and 10.2 GPa. To confirm this, the GGA results are presented in Fig. 6.14 for these two pressures.
- These findings give strong evidence that the VdW interaction is not solely the driving force for the bonding mechanism in anthracene.

6.3 Optical Properties

Studies on the optical absorption processes in organic polymers give controversial answers to the question, whether the lowest energy transition is due to free charge carriers (direct interband transitions) or the absorption of tightly bound excitons (Frenkel exciton model) [37, 38]. In this context, the experimentally determined exciton binding energy published for PPV ranges from 0.1 to 0.9 eV [40]. With this work it will be contributed to solve this puzzle on the exciton binding energies in organic semiconductors. To a first approximation,

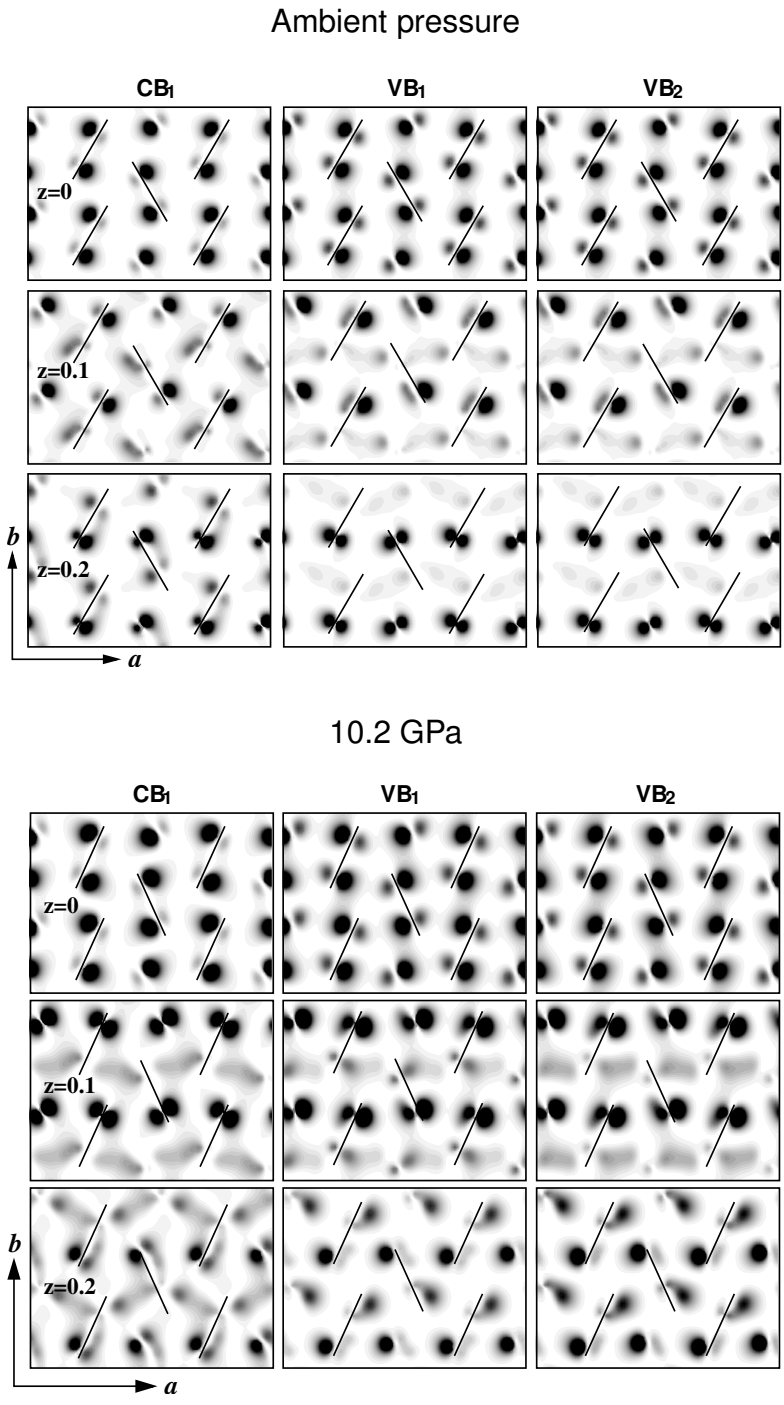

Figure 6.14: GGA 2D electron density plots of CB_1, VB_1, and VB_2 in the (ab)-plane calculated as sum over 40 $\mathbf{k}$-points along $\overline{\Gamma\mathrm{KZ}}$ for different z-coordinates in units of c at ambient pressure and 10.2 GPa, respectively. The thin solid lines indicate the molecules to illustrate the herringbone stacking in anthracene. The dark regions correspond to high density and vice versa.

the optical absorption spectra of anthracene as a function of pressure have been investigated by calculating the dielectric function within the RPA. Further, excitonic effects have been included in the dielectric tensor by solving the BSE (Sec. 4.2.1) for the e-h two-particle Green's function in an ab-initio framework.

6.3.1 Optical Spectra within the RPA

According to the monoclinic symmetry of the crystal, the computed dielectric function consists of the Cartesian diagonal elements $Im\varepsilon_{zz}$, $Im\varepsilon_{yy}$, and $Im\varepsilon_{xx}$, and the additional off-diagonal xz-component. The Cartesian axes y and z are equivalent to the crystalline b- and c-axis, while the a-axis deviates from x by the monoclinic angle β. For the reasons given in Sec. A.2.1, $Im\ \varepsilon_{yy}$ and $Im\ \varepsilon_{bb}$ are identical as well as $Im\ \varepsilon_{zz}$ and $Im\ \varepsilon_{cc}$.

In Fig. 6.15 the y-component (top panel) and z-component (bottom panel) of the imaginary part of the dielectric tensor as a function of pressure are presented. The a-component is minor and therefore not displayed in Fig. 6.15. Note, these are uncorrected LDA results.

At ambient pressure, a y-polarized transition with weak oscillator strength at 2.1 eV is found. As emphasized before, this energy corresponds to the lowest direct band gap indicating that the lowest direct transition in anthracene is also an optically active one. In addition, a strong z-polarized peak next in energy at 3.5 eV is obtained. The lowest transition corresponds to the optical response generated by light with the electric field vector parallel to the short molecular axis, whereas the latter is due to long molecular axis polarized probing light.

Both transitions are shifted to lower energies (red-shift) and broadened with increasing pressure, which is a consequence of the increase in the band widths and band splitting. Analogously to the trend found in the band structures, this pressure effect is more strongly pronounced in the low pressure region. These spectra agree with early measurements of the near-ultraviolet and visible absorption peaks of anthracene by WIEDERHORN and DRICKAMER [100], which confirm the red-shift and the broadening as a function of pressure. They observe a linear red-shift of approximately -0.06 eV/GPa for the lowest absorption peak, which is constant up to 5 GPa. In the higher pressure region the red-shift is diminished and non-linear.

Concerning the band gap, we have found that $E_{\mathrm{g}}^{\mathrm{LDA}}$ requires a self-energy correction Δ_{c} of 2.0$\pm$0.2 eV at ambient pressure. Since the difference between the $E_{\mathrm{g}}^{\mathrm{LDA}}$ and RPA gap $\Delta_{\mathrm{g}}^{\mathrm{LDA}}$ is only 0.1 eV, it could be assumed, that this scissors operator is also a good approximation for adapting the RPA spectra at ambient pressure. However, the question, whether the scissors operator is pressure dependent or not, still remains. Moreover, more recent optical

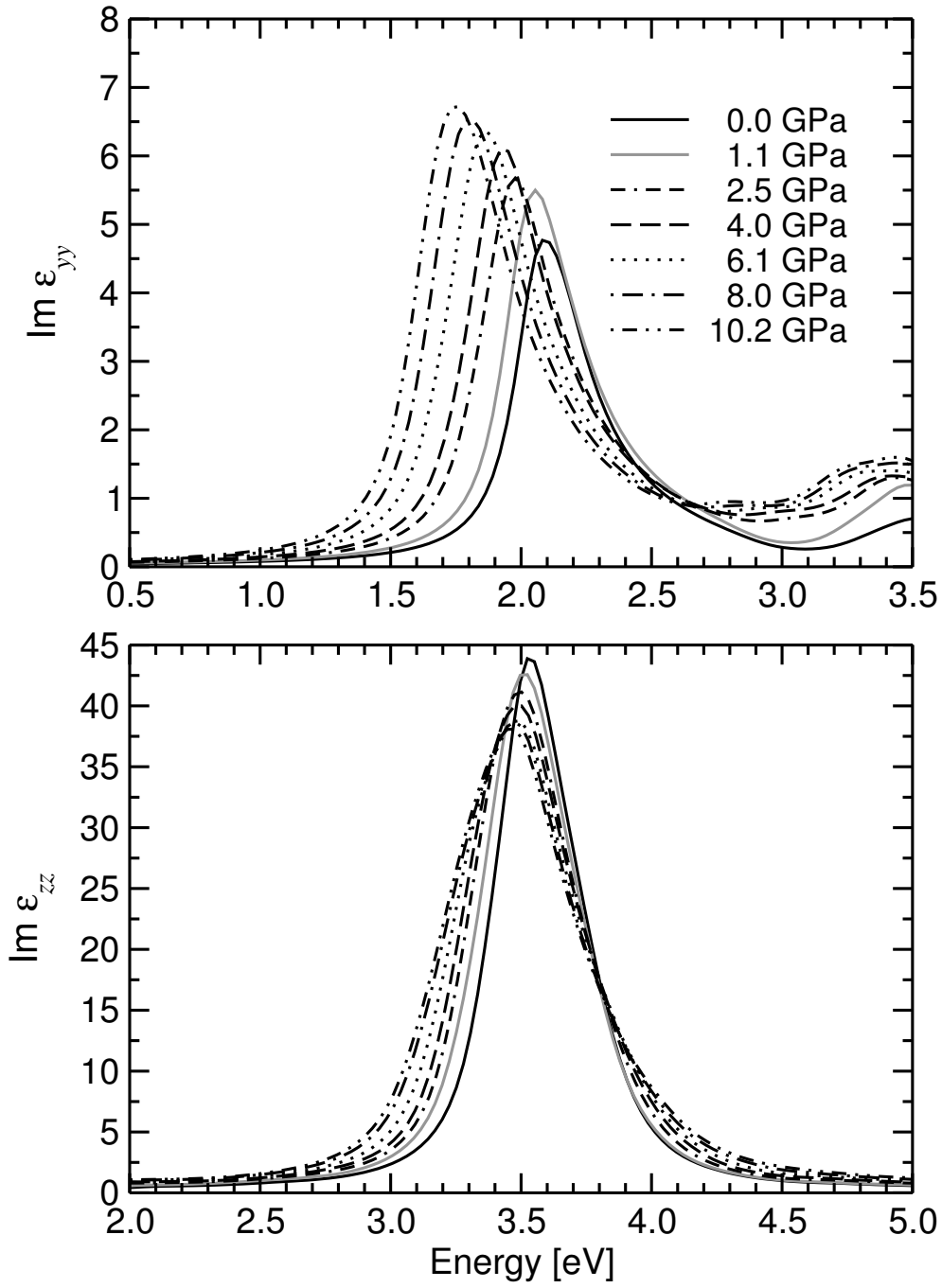

Figure 6.15: Imaginary part of the dielectric tensor computed at several pressure values up to 10.2 GPa separated in y-polarized (top panel) and z-polarized response (bottom panel). The self-energy correction Δ_c has been omitted. A life-time broadening of 0.1 eV has been included to smoothen the spectra.

absorption measurements of crystalline anthracene have observed that the lowest transition is due to a spin singlet exciton (e-h pair) [101]. The energy levels of such bound excitons are located within the electronic band gap. Thus the optical gap is reduced by the exciton binding energy. The energies of the spin singlet excitons in anthracene have also been measured as a function of pressure [101], which should be used for comparison to the calculated spectra and thus could give Δ_{c} as a function of pressure. But before, the e-h interactions have to be included in the theoretical model for a proper description of the optical properties.

6.3.2 Optical spectra including e-h interactions

For organic molecular crystals it is generally agreed that the intermolecular interactions are weak and therefore their photophysics are governed by electron-hole pairs confined to single molecules with large exciton binding energies. In this section, the excitonic effects in anthracene and their pressure dependence are addressed. Figure 6.16 presents the two major components of the imaginary part of the dielectric tensor including e-h interactions calculated by solving the BSE as a function of pressure. The RPA results are included for comparison. For consistency, the RPA, as well as the BSE optical spectra have been corrected by a pressure dependent self-energy correction $\Delta_{\mathrm{c}}(p)$, which will be discussed in Sec. 6.3.3.

First, we focus on the y-polarized optical spectra at ambient pressure, which are depicted in the left panels of Fig. 6.16. Both, the RPA and the BSE formalism, find the lowest optical transition to be short-axis polarized and of weak oscillator strength. The inclusion of e-h interactions further identifies it as a strongly bound singlet exciton (S) below the RPA gap at 3.11 eV. The corresponding spin triplet exciton (T) is found further below in energy at 1.89 eV, which is in excellent agreement with the experimental values of 1.83 eV [102] and 1.85 eV [92], respectively. The resulting singlet-triplet (S-T) splitting is 1.22 eV at ambient pressure, which perfectly reproduces the experimental value of 1.27 eV [92]. The spin singlet exciton binding energy (SBE), which is defined as the energy difference of the quasi-particle gap (RPA peak) and the S peak maximum, is 0.64 eV. As expected, it is larger compared to the values so far calculated for polymers [18, 26], where such a high SBE has only been obtained for isolated polymer chains. Analogously to SBE, the triplet exciton binding energy (TBE) is determined to be 1.86 eV.

If pressure is applied, S is shifted to lower energies by approximately 0.4 eV up to 10.2 GPa. This can be understood by looking at the dielectric constant $\varepsilon_{00}(0)$ as a function of pressure, which is shown in the right panel of Fig. 6.17. This quantity represents the major component of the dielectric screening in

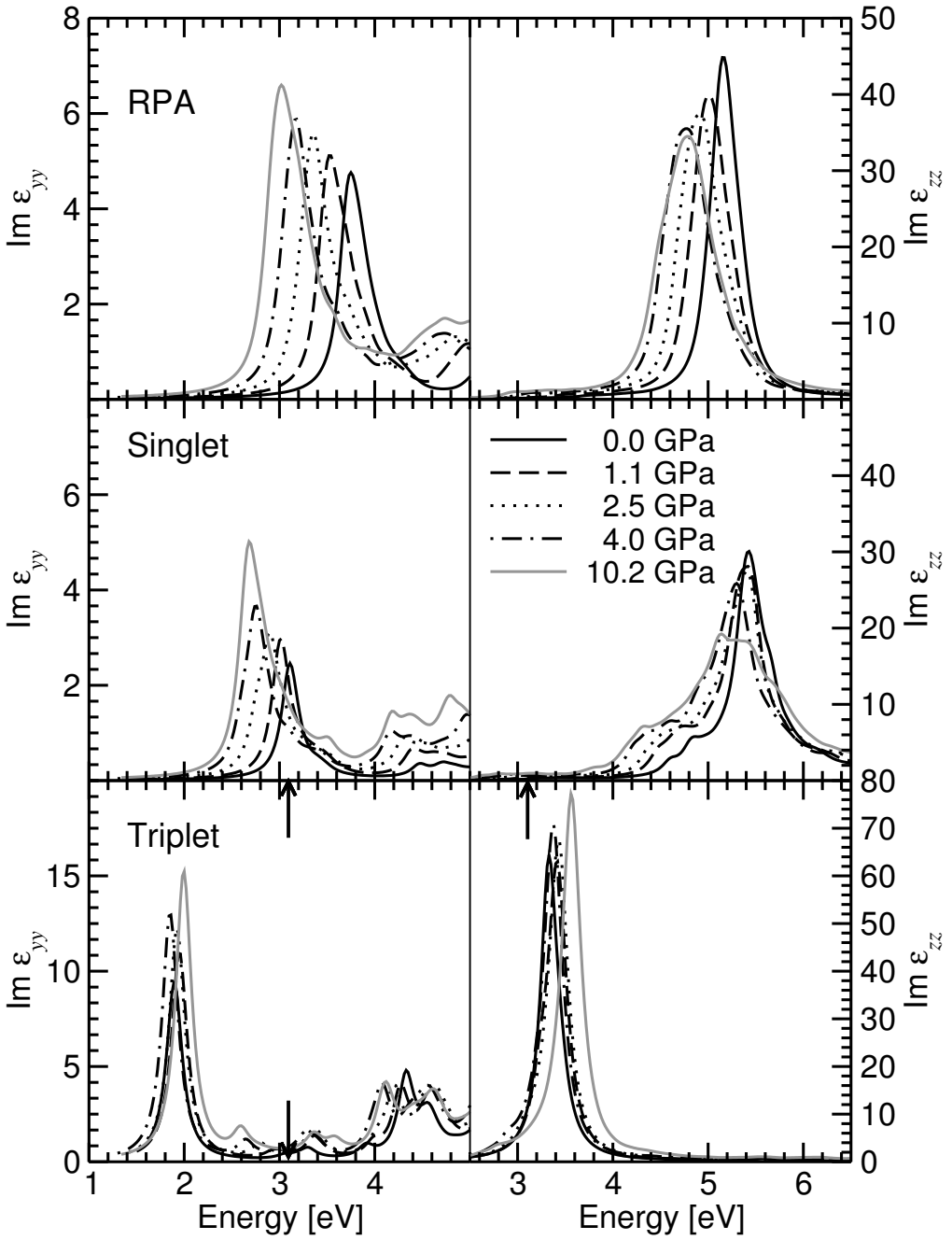

Figure 6.16: y-component (left panels) and z-component (right panels) of the imaginary part of the dielectric tensor as a function of pressure calculated using the RPA (upper panels) compared to the solution of the BSE (lower panels). All optical absorption spectra have been corrected by the self-energy correction given in Tab. 6.7. A life-time broadening of 0.1 eV has been included. The arrows at 3.1 eV indicate the optical gap at ambient pressure.

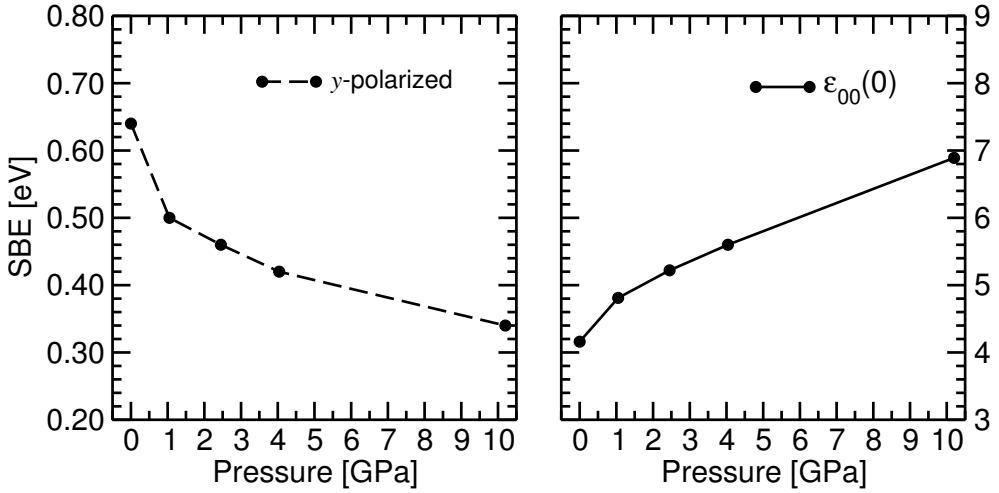

Figure 6.17: The spin singlet exciton binding energy (left panel) and the major component of the dielectric screening (right panel) as a function of pressure.

the 3D environment. As can be seen from Fig. 6.17 it is strongly enhanced by pressure. For this reason, the SBE decreases with pressure and is reduced to almost 50% at 10.2 GPa, which is 0.34 eV. This effect is illustrated in the left panel of Fig. 6.17 as well as in Tab. 6.5. As a consequence, the pressure induced red-shift of the absorption peaks is less pronounced than that suggested by the RPA. In contrast to S, the energy shift of T is very small, i.e.,

Table 6.5: y-polarized response: The peak positions (maxima) of the RPA result, the spin singlet (S), and triplet (T) e-h pair, as well as the spin singlet (triplet) exciton binding energy SBE (TBE) and the singlet-triplet (S-T) splitting as a function of pressure.

p [GPa]	0.0	1.1	2.5	4.0	10.2
RPA [eV]	3.75	3.52	3.36	3.18	3.02
S [eV]	3.11	3.02	2.90	2.76	2.68
T [eV]	1.89	1.94	1.92	1.86	2.00
SBE [eV]	0.64	0.50	0.46	0.42	0.34
TBE [eV]	1.86	1.58	1.44	1.32	1.02
S-T [eV]	1.22	1.08	0.98	0.90	0.68

comparable to the theoretical accuracy. Nevertheless, due to the dominating shift of S and the RPA gap, respectively, the S-T splitting as well as the TBE decrease with pressure to almost 50% at 10.2 GPa.

Let us now concentrate on the response to z-polarized light shown in the

right panels of Fig. 6.16. The energies of these transitions are summarized in Tab. 6.6. In this channel, an excitation at 5.4 eV is found, which exhibits much larger oscillator strength compared to S. This is the second optically active absorption and in contrast to S, it appears above the quasi-particle gap, indicating that it is due to a free e-h pair (FE). The corresponding spin triplet state appears at 3.3 eV, which is 2.1 eV below the optically active FE. This long-axis polarized excitation is shifted to the red by pressure, but only by half the amount of S, which is approximately 0.2 eV up to 10.2 GPa[1]. Again, the shift obtained by the BSE calculation is less pronounced than that observed within the RPA.

Table 6.6: z-polarized response: Analogous to Tab. 6.5, but only the peak positions and the splitting between FE and T (FE-T) are listed.

p [GPa]	0.0	1.1	2.5	4.0	10.2
RPA [eV]	5.15	5.00	4.92	4.78	4.78
FE [eV]	5.43	5.42	5.50	5.30	5.21
T [eV]	3.33	3.42	3.42	3.38	3.56
FE-T [eV]	2.10	2.00	1.98	1.92	1.67

At ambient pressure the excitation energies of these two transitions are in agreement with those reported by SCHLOSSER and PHILPOTT [103]. Unfortunately, the calculated z-polarized absorption spectrum as a function of pressure cannot be compared to experiment, because the earlier published pressure investigations [100, 101, 104] have only measured the b-axis polarized spectrum and a polarization direction perpendicular, which is not well defined. In this context, it is pointed out that the c-component of the dielectric function is the strongest one, whereas the a-component is nearly negligible. Therefore, the performance of optical absorption measurements of anthracene under pressure with light polarized along the crystalline c-axis would be extremely important.

6.3.3 The optical gap

In this section, the calculated optical gap is compared to experimental data. As introductory remark it is emphasized that all calculations of the imaginary part of the dielectric tensor including e-h interactions have been performed without invoking the GW approach [64, 65], which would provide the self-energy

[1] Since the peak shape at 10.2 GPa is not distinct, which is presumably due to the coarse $\mathbf{k}$-mesh, the mean between the two peak maxima has been taken.

for correcting the LDA gap. The comparison of the calculated optical gaps, Δ_{g}, to the experimentally observed ones, $\Delta_{\mathrm{g}}^{\mathrm{exp}}$ [101] up to 4 GPa allows us to determine the pressure dependence of the self-energy correction Δ_{c}. In Tab. 6.7, $\Delta_{\mathrm{g}}^{\mathrm{LDA}}$, $\Delta_{\mathrm{g}}^{\mathrm{exp}}$, the resulting Δ_{c}, and the ratio between the theoretical and experimental optical gap are listed up to 10.2 GPa. The experimental error evaluated by comparison of two experimental data sets [101, 104] does not exceed 0.05 eV. Besides, the theoretical accuracy depends on the $\mathbf{k}$-mesh used for the calculation. In case of the BSE calculations this mesh was rather coarse to keep the computing times tolerable. As shown in Sec. B.1, the convergence with the number of $\mathbf{k}$-points has been tested by comparing the RPA spectrum of anthracene calculated on a much finer $\mathbf{k}$-mesh (413 $\mathbf{k}$-points) with that obtained for 64 $\mathbf{k}$-points. This convergence tests make confident that the theoretical error is less than 0.1 eV. Regardless these small uncertainties, the ratio between the theoretical and experimental optical gaps up to 4 GPa is found to be a constant factor of approximately 0.5 independent of pressure. At this point it is emphasized that the previously found underestimation of the LDA quasi-particle gap in various polymers by 40% [105] is only true within the RPA. Since our previous calculations of the structural and electronic properties of anthracene revealed that the pressure effect is less pronounced in the high pressure region [106], it is assumed that this factor is still valid for 10.2 GPa. This enables to predict an optical gap of 2.68$\pm$0.1 eV for 10.2 GPa. Moreover, this knowledge allows to estimate the optical gap of other molecular crystals without performing the exact, but expensive GW calculations for the self-energy correction.

Table 6.7: Calculated and experimentally observed optical energy gaps, Δ_{g} and $\Delta_{\mathrm{g}}^{\mathrm{exp}}$ [101], respectively, the resulting self-energy correction Δ_{c}, and the ratio between Δ_{g} and $\Delta_{\mathrm{g}}^{\mathrm{exp}}$ as a function of pressure.

p [GPa]	$\Delta_{\mathrm{g}}^{\mathrm{LDA}}$ [eV]	$\Delta_{\mathrm{g}}^{\mathrm{exp}}$ [eV]	Δ_{c}[eV]	$\Delta_{\mathrm{g}}^{\mathrm{LDA}} : \Delta_{\mathrm{g}}^{\mathrm{exp}}$
0.0	1.48	3.11	1.63	0.48
1.1	1.52	3.02	1.50	0.50
2.5	1.48	2.90	1.42	0.51
4.0	1.46	2.76	1.30	0.53
10.2	1.34	2.68		

6.3.4 Spin singlet exciton wavefunctions

In order to further highlight the physical origin of the differences between the two lowest optical excitations, as well as their pressure dependence, the spin singlet exciton wavefunctions have been computed according to Eq. (4.6). In Figs. 6.18 and 6.19, the electron distributions with respect to the hole at a fixed position are depicted. The calculation of the wavefunctions has been performed on a rectangular 2D grid including 4×4 unit cells for ambient pressure as well as 10.2 GPa. The size of one unit cell is indicated by the dashed rectangles in each plot. In the upper and lower panels of these figures the (ab)-planes and the (ac)-planes of the bound singlet exciton and the free e-h pair are displayed, respectively. In detail, the (ab)-maps represent slides through the unit cell at $z = 0.3$ with the hole located at $z = 0$. Note, z is given in units of the lattice constant c. Analogously, the (ac)-maps describe the slides at $y = 0.3$ with the hole fixed at $y = 0$, where y is given in units of b. The cross refers to the position of the hole in the 2D grid that has been chosen in a region of non-vanishing probability density for the electron.

The important structural features of anthracene are clearly visible, which are the herringbone stacking of the molecules and the layered structure along c. The former is evident in the (ab)-map of the exciton wavefunction, while the latter can be identified in the (ac)-maps.

Let us discuss the S wavefunction at ambient pressure first, which is depicted in the left panels in Fig.6.18. There is no doubt that the electron of the e-h pair (dark regions) spreads over neighboring molecules along the a-axis, but predominantly in b-direction. However, the SBE is still as large as calculated for the isolated PA chain [18]. In fact, in the isolated PA chain the exciton is confined to one chain, but extended over approximately 20 unit cells in c-direction. For comparison, in anthracene it is basically restricted to one unit cell along c, what explains the rather large SBE despite its extension in the (ab)-plane.

Now the electron distribution of S is compared to that of FE (right panels in Fig.6.18). In case of S, the electron is found predominantly close to the hole. In contrast, the electron in FE avoids the vicinity of the hole and thus it is not bound to it. This holds for both maps, the (ab)- and (ac)-plane, emphasizing the bound nature of S and the independency of the charge carriers in FE. Moreover, the FE is spread out to neighboring molecules in the (ac)-plane to a higher extent than S.

If pressure is applied, the extension of S in the (ab)-plane is highly increased, whereas the e-h wavefunction remains rather confined in the c direction (bottom left panel in Fig.6.18). While the former is the reason for the significant reduction of SBE with pressure, the latter ensures that the electron and the

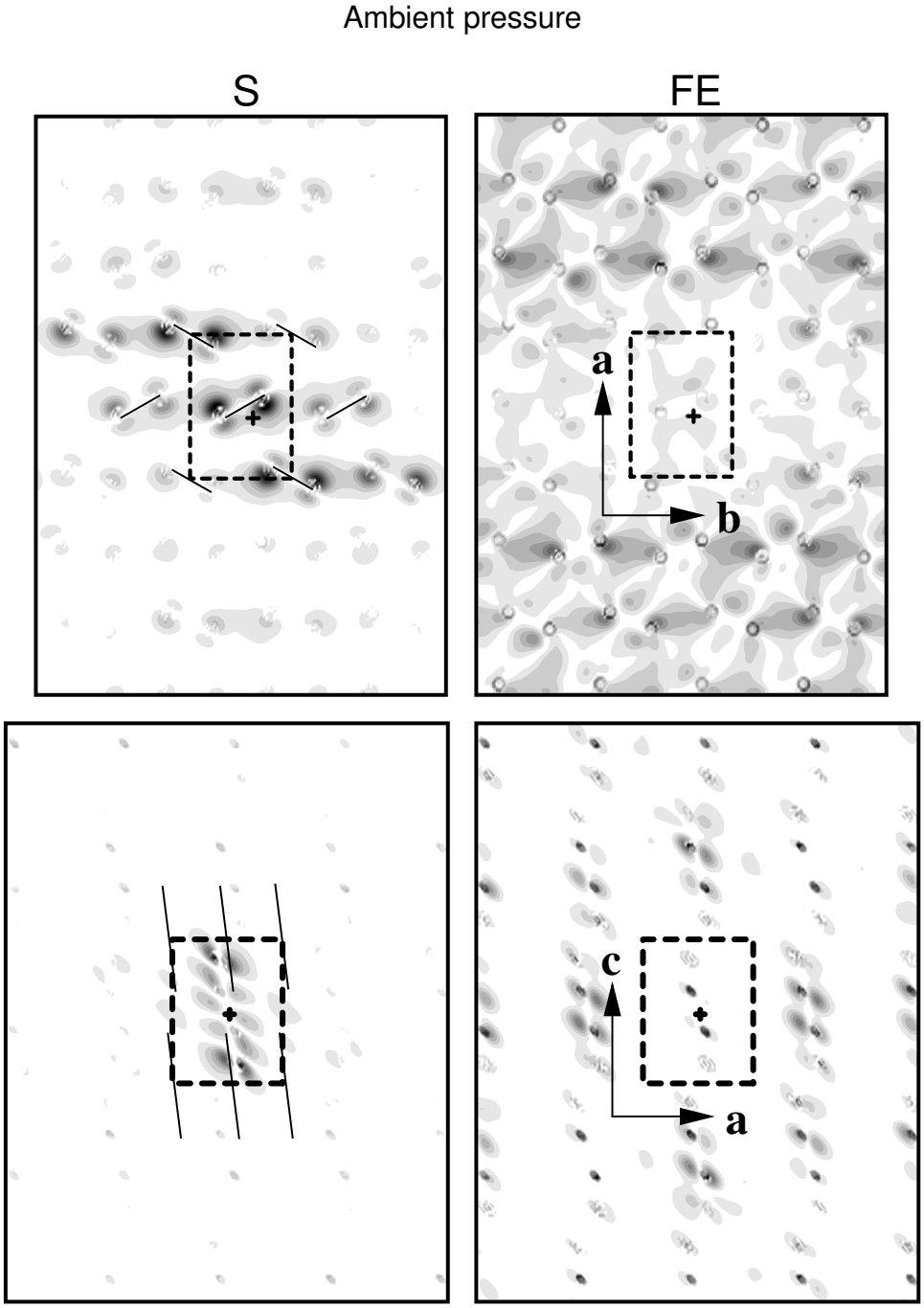

Figure 6.18: The 2D electron distribution $|\psi_{c\mathbf{k}}(\mathbf{r}_e)|$ with respect to the hole at a fixed position (dark cross) calculated at ambient pressure for S (left panels) and FE (right panels), respectively. The unit cell is indicated by dashed rectangles, the molecules therein by thin solid lines. These (ab)- [(ac)-] maps represent slides at $z = 0.3$ [$y = 0.3$] with the hole located at $z = 0$ [$y = 0$] in units of c [b]. The dark regions correspond to high density.

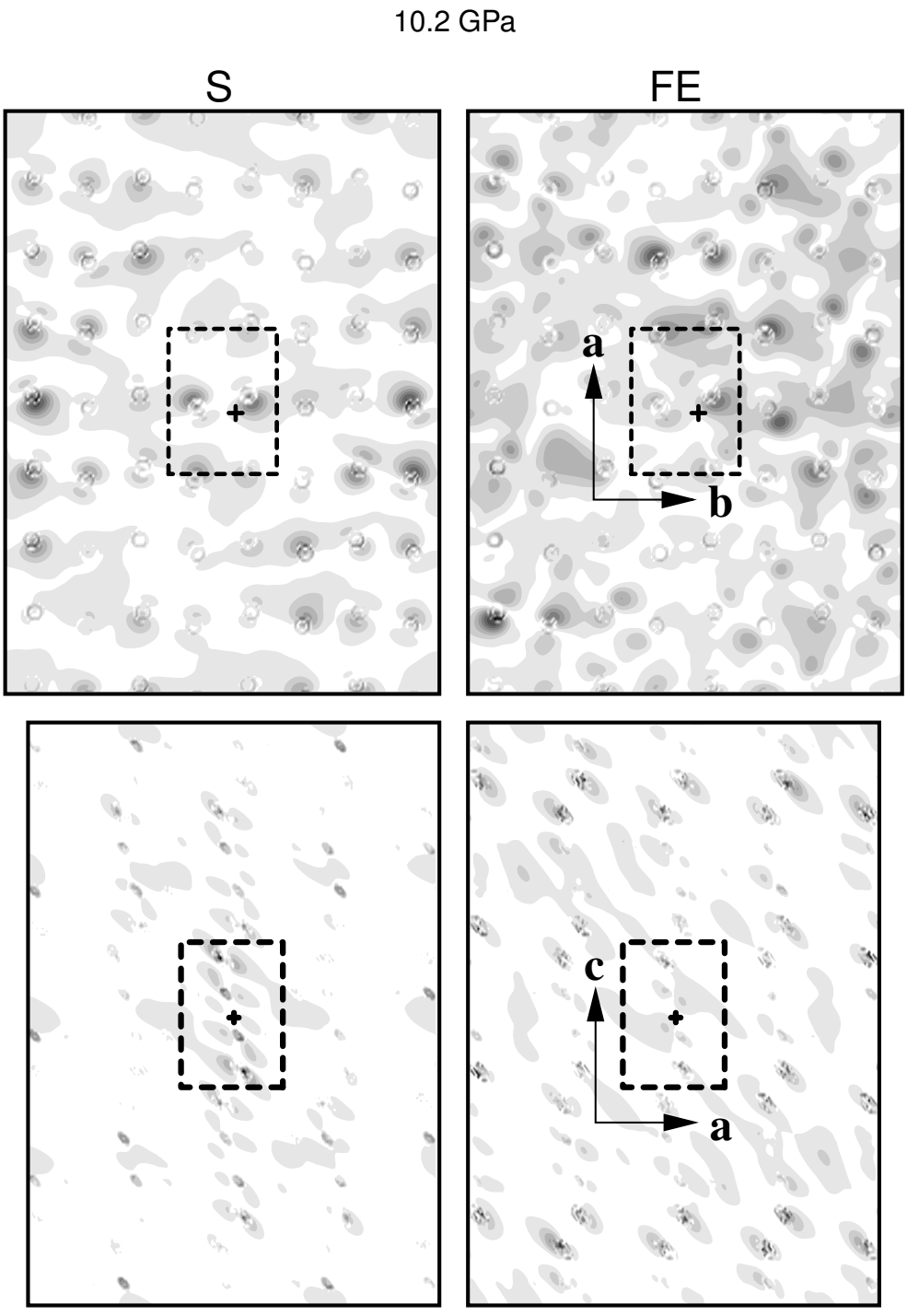

Figure 6.19: Analogous to Fig. 6.18, but evaluated at 10.2 GPa.

hole are still bound. As expected, pressure affects the electron distribution in FE to a smaller extent. Regarding the (ab)-map of FE, the electron is now almost uniformly distributed with respect to the hole. From the comparison of the FE (ac)-maps at 0 and 10.2 GPa it is clear, that the e-h wavefunction is expanded in a direction by pressure. These observations are consistent with the pressure effect on the band structure and can be explained through the enhancement of the intermolecular interactions by pressure. These interactions are generally responsible for an increased dielectric screening and thus for the reduction of the e-h pair binding energy. Due to the anisotropy of this enhancement the red shift of FE is smaller compared to S.

6.3.5 Conclusions

These calculations clearly demonstrate that in one material, depending on the polarization of the probing light with respect to the crystalline axes the physics underlying the optical response is different: While in the y-polarized channel a bound spin singlet e-h pair with 0.64 eV binding energy is found, the excitation higher in energy is z-polarized and can be as well as an excitation higher in energy, which can be traced back to free charge carriers. This fact is an important contribution to the ongoing discussion whether optical absorption processes in such materials are due to bound excitons or free electron-hole pairs. Compared to PA, the exciton binding energy is by a factor of 10 larger in anthracene. From this fact can be concluded that

- the exciton binding energy of bound e-h pairs could be generally larger in molecular crystals built of oligomers
- the exciton binding energy should strongly depend on the size of the molecules.

In general, absorption measurements for well defined polarization directions could further help to clarify the situation in different materials.

7 Properties of the Oligo-Acenes

Es ist schwieriger, eine vorgefaßte Meinung zu zertrümmern als ein Atom.

Albert Einstein

A variety of measurements have been performed on the linear oligo-acenes to determine their electronic and optical properties, e.g., carrier mobilities [33, 34, 107, 108] and photoconductivity [109]. Since fewer theoretical investigations are available, the FP-LAPW 3D band structure approach is applied to the first four members of the oligo-acenes in order to study the dependence of the physical properties on the oligomer length. The materials considered are naphthalene (2A), anthracene (3A), tetracene (4A), and pentacene (5A). Details on their crystal structure have been given in Sec. 5.1.

7.1 Electronic Properties

Starting from the experimentally determined crystal structures at ambient pressure and temperature, the molecular geometry has been optimized by relaxing the atomic positions, i.e., minimizing the forces acting on the atoms. Subsequently the electronic band structures along high symmetry directions have been calculated. These results are compared to theoretical findings obtained within the tight binding approximation by CHENG et al. [110].

7.1.1 Band structures

Before the band structures are discussed, it is reminded, that the unit cells of both, the monoclinic as well as the triclinic structures, contain two inequivalent molecules. As a consequence, each band in the band structures appears

doubled forming a band pair. Besides some high symmetry points in the IBZ, the bands of these pairs are non-degenerate giving rise to the band splitting.

The ab-initio band structures of the investigated series of oligo-acenes are presented in Figs. 7.2 and 7.3. The directions of high symmetry chosen for the $\mathbf{k}$-point sampling are illustrated in Fig. 7.1. The internal coordinates of the points along these directions Γ, Y, Z, A, B, C, D, and E in units of $(2\pi/a,\ 2\pi/b,\ 2\pi/c)$ are (0,0,0), (0.5,0,0), (0,0,0.5), (0.5,0.5,0), (0,0.5,0), (0,0.5,-0.5), (0.5,0.5,-0.5), and (0.5,0,-0.5), respectively. The point K in 2A and 3A corresponds to (0.4,0,0.2). In case of pentacene the coordinates of E and K are (0.5,0.01,-0.53) and (0.47,0.01,0.14).

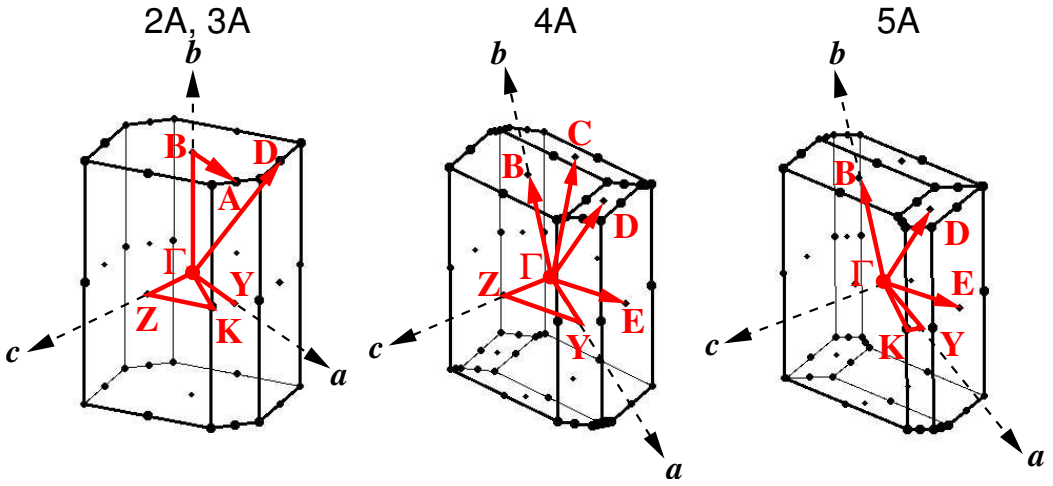

Figure 7.1: The $\mathbf{k}$-path used for the band structure calculations of 2A, 3A, 4A, and 5A. The coordinates of the high symmetry points Γ, Y, Z, A, B, C, D, and E in units of $(2\pi/a,\ 2\pi/b,\ 2\pi/c)$ are (0,0,0), (0.5,0,0), (0,0,0.5), (0.5,0.5,0), (0,0.5,0), (0,0.5,-0.5), (0.5,0.5,-0.5), and (0.5,0,-0.5), respectively. The point K in 2A and 3A corresponds to (0.4,0,0.2). In case of pentacene the coordinates of E and K are (0.5,0.01,-0.53) and (0.47,0.01,0.14).

Noticeable is that the two band structures corresponding to 2A and 3A are very similar. Besides, the band structure of 4A is alike that of 5A, but both can be clearly distinguished from the former. Thus there is a clear distinction between the monoclinic systems and the triclinic materials. This grouping is also found by evaluating the band splitting and band widths of these four oligo-acenes. The results of this analysis are visualized in Fig. 7.4, which shows the band splitting of the highest occupied VB and the lowest unoccupied CB at high symmetry points in the IBZ. For 2A and 3A the largest band splitting of VB as well as CB is obtained at the Z-point. In contrast, the VB and CB in 4A and 5A exhibit the largest splitting at the D-point. Note, at this point the bands corresponding to VB and CB are degenerate in 2A and 3A.

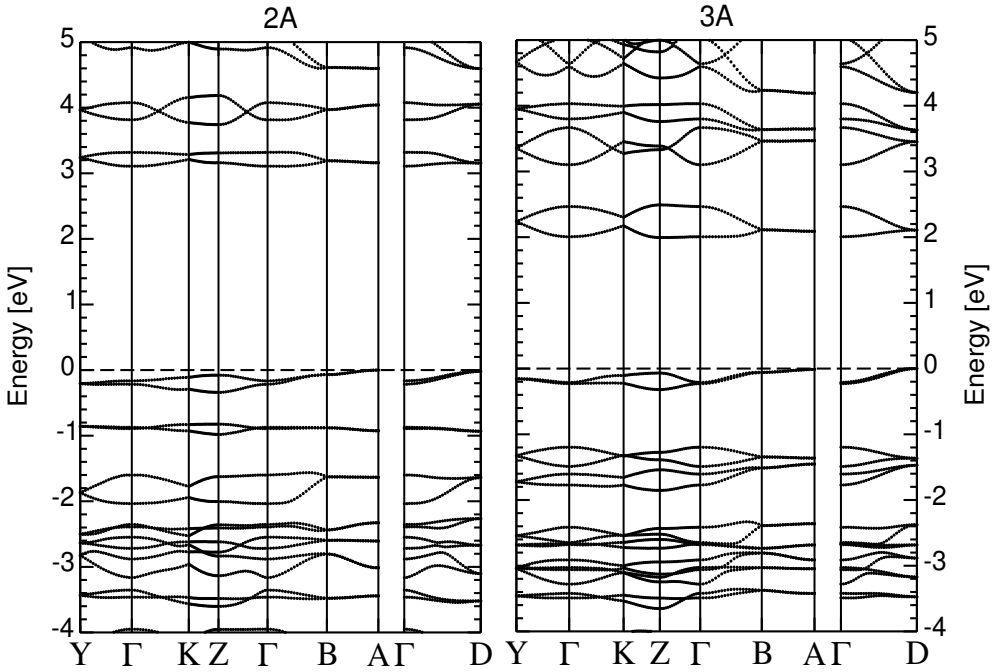

Figure 7.2: The band structures E($\mathbf{k}$) of the monoclinic 2A and 3A. The coordinates of the high symmetry points are specified in Fig. 7.1. The Fermi level is indicated by the dashed line.

Regarding the band widths of CB_1, VB_1, and VB_2 evaluated in the directions $\overline{\Gamma B}$, $\overline{\Gamma D}$, $\overline{\Gamma Y}$, and $\overline{\Gamma Z}$, which are depicted in Fig. 7.5 for the series, the analogous distinction between monoclinic and triclinic materials is expected. Both, 2A and 3A, show comparable band widths in each of the chosen direction. The two triclinic systems 4A and 5A exhibit also similar band widths along these directions, which are significantly smaller than those of the monoclinic materials. In 2A and 3A, the largest band dispersion of the first two valence bands VB_1 and VB_2 are determined in the direction of $\overline{\Gamma D}$. The lowest conduction band CB_1 of these systems exhibits the largest band widths along $\overline{\Gamma Y}$. In contrast, in the triclinic systems 4A and 5A the band dispersion of VB_1 is largest in $\overline{\Gamma B}$, while CB_1 and VB_2 reach their maximal band widths in $\overline{\Gamma D}$. Therefrom, it can be expected, that:

- in 2A and 3A the favored electron conduction channel is $\overline{\Gamma Y}$
- in 2A and 3A the favored hole conduction channel is $\overline{\Gamma D}$
- in 4A and 5A the favored electron conduction channel is $\overline{\Gamma D}$
- in 4A and 5A the favored electron conduction channel is $\overline{\Gamma B}$

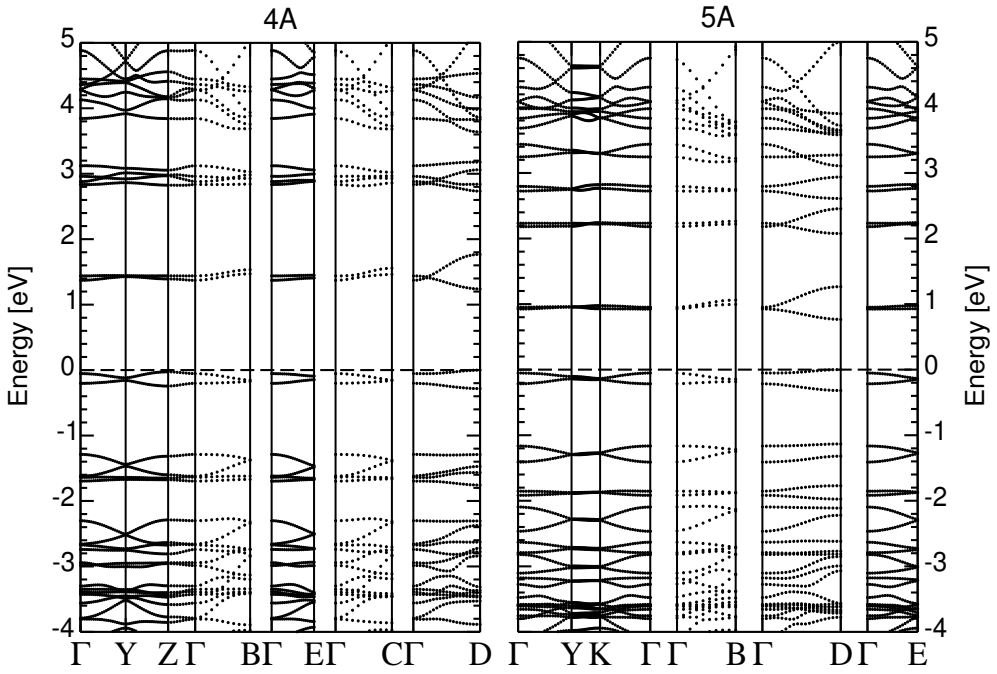

Figure 7.3: The band structures E($\mathbf{k}$) of the triclinic systems 4A and 5A. The coordinates of the high symmetry points are specified in Fig. 7.1. The Fermi level is indicated by the dashed line.

Note, all these directions are perpendicular to the long molecular axes, which is lying approximately in the $\overline{\Gamma \mathrm{Z}}$ direction.

The total band dispersion evaluated as difference between the maximum and minimum of the considered band, respectively, are listed in Tab. 7.1 for CB_1, VB_1, and VB_2. Within the series, 3A shows the highest band dispersion on av-

Table 7.1: The total band dispersion of 2A, 3A, 4A, and 5A for CB_1, VB_1, and VB_2.

band dispersion [eV]	2A	3A	4A	5A
CB_1	0.14	0.25	0.23	0.23
VB_1	0.21	0.21	0.15	0.15
VB_2	0.34	0.32	0.13	0.18

erage over the three investigated bands, followed by 2A. In 4A and 5A all bands are significantly flatter giving rise to higher effective carrier masses and therefore smaller charge carrier mobilities can be expected. The values listed in Tab. 7.1 range from 0.1 to 0.3 eV and are smaller compared to the 0.1 – 0.5 eV obtained by the tight binding approximation of Ref. [110]. Moreover, the latter

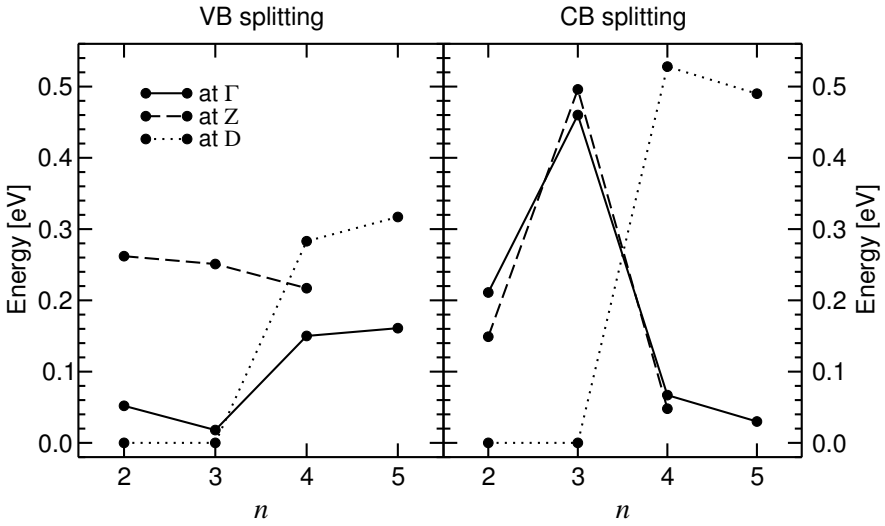

Figure 7.4: The band splitting of the highest occupied VB (left) and the lowest unoccupied CB (right) at high symmetry points in the IBZ as a function of the oligomer length.

yielded an increase with the oligomer lengths that could not been reproduced by the FP-LAPW method. Similar to the band widths of the oligomers of PPP, which exhibit a decrease within the series from biphenyl to hexaphenyl [29], a reduction of the band dispersion is also found for the oligo-acenes. It is assumed that the inherent difference in the methods used for the calculations is responsible for these discrepancies. As already pointed out in the previous chapter, considering the full 3D environment is crucial for a proper description of the electronic and optical properties. While the FP-LAPW scheme takes into account the full crystalline symmetry, in the tight binding approximation the calculations were done for molecular clusters.

7.1.2 Band gaps

When the fundamental band gaps of the monoclinic structures 2A and 3A are compared to those of the triclinic ones, it is clear from the band structures, that the former exhibit an indirect band gap, whereas in 4A and 5A a direct band gap is found. The direct band gap of 4A and 5A appears at the D-point, respectively. The fundamental band gaps of all oligo-acenes deduced from the band structures are listed in Tab. 7.2 together with experimental data [92, 111] for comparison. For additional information, the lowest direct energy gap in 2A is 3.16 eV, while it is 2.10 eV in 3A. In both cases, the VB maximum and the CB minimum are located at the A-point. In 2A as well as in 3A the direct gap

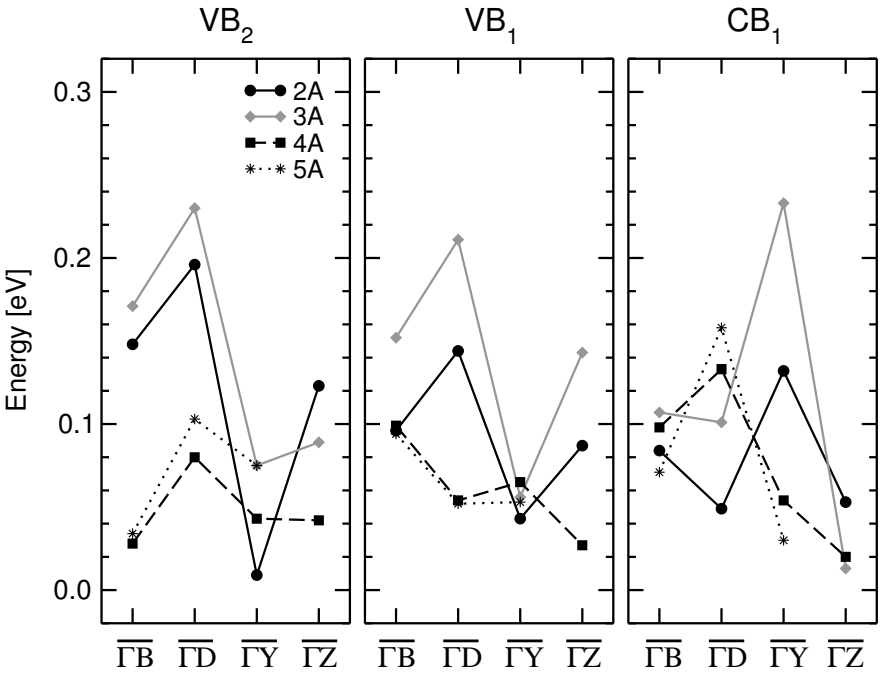

Figure 7.5: The band widths of CB_1, VB_1, and VB_2 evaluated in high symmetry directions as a function of oligomer length. Note that $\overline{\Gamma\mathrm{Y}}$ ($\overline{\Gamma\mathrm{B}}$) is parallel to the crystalline a-axis (b-axis), and $\overline{\Gamma\mathrm{Z}}$ corresponds to the c-direction, which is approximately the long molecular axis.

evaluated at the D-point differs only by less than 1 meV form that at A.

According to these values, the band gap decreases with the oligomer length n, which is illustrated in the left panel of Fig. 7.6. In fact, The GGA calculation underestimates the absolute value of the band gap, but the experimentally observed decrease within the series is almost perfectly reproduced by theory. A similar trend has been found for the oligomers of PPP, for which has been shown that the quasi-particle gaps follow the so-called $1/n$ law [29, 112–114]. Thus, by plotting the energy gap versus the inverse oligomer length a linear dependence is obtained. As can be seen from the right panel in Fig. 7.6, the

Table 7.2: The ab-initio energy gaps $E_{\mathrm{g}}^{\mathrm{GGA}}$ of 2A, 3A, 4A, and 5A compared to experimentally observed values [92, 111].

E_{g} [eV]	2A	3A	4A	5A
GGA	3.1	2.0	1.2	0.8
experiment	5.0	3.9	2.9	2.2

oligo-acenes exhibit also a nearly linear relation between energy gap and $1/n$, but with a kink, that distinguishes the monoclinic crystals 2A and 3A from the triclinic structures 4A and 5A.

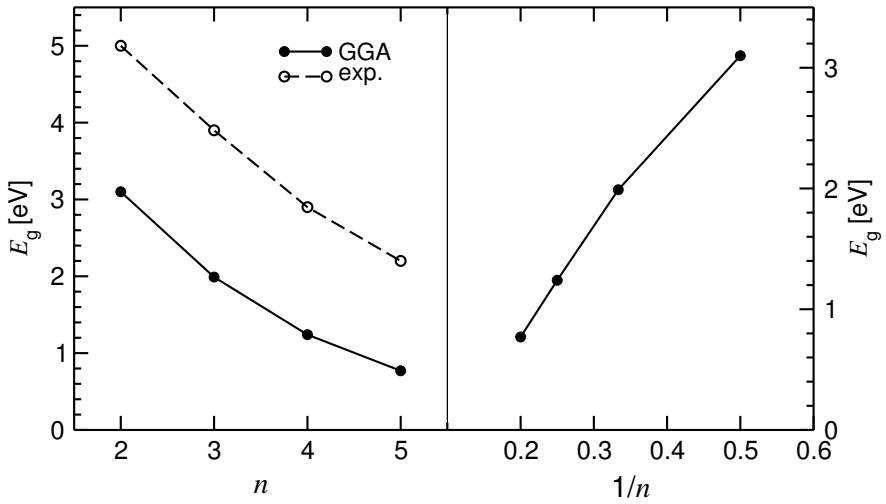

Figure 7.6: The GGA energy gap $E_{\mathrm{g}}^{\mathrm{GGA}}$ compared to data available in literature [92, 111] as a function of the oligomer length n (left) as well as a function of the inverse oligomer length $1/n$ (right).

7.2 Optical Properties

Up to now, we have studied the excitonic effects on the optical absorption spectra in anthracene under high pressure. There it has been found, that the lowest, but weak transition is generated by a strongly bound e-h pair, whereas the strong absorption next in energy is due to free charge carriers. In this context, we are also interested, how the optical properties depend on the oligomer length. For this reason, the optical absorption spectra have been calculated for the four oligo-acenes in the same way as previously described for anthracene under pressure. Unfortunately, the computation of the BSE for pentacene is extremely time consuming and could not been performed up to now. However, its optical spectrum calculated within the RPA is included in this analysis.

Figure 7.7 presents the two major components of the imaginary part of the dielectric tensor calculated within the RPA compared to the spectra including excitonic effects. To this extent, both, the RPA as well as the BSE optical spectra have not been corrected by a scissors operator Δ_{c}. Therefore, the absolute positions of the absorption peaks are underestimated in their energy. For the

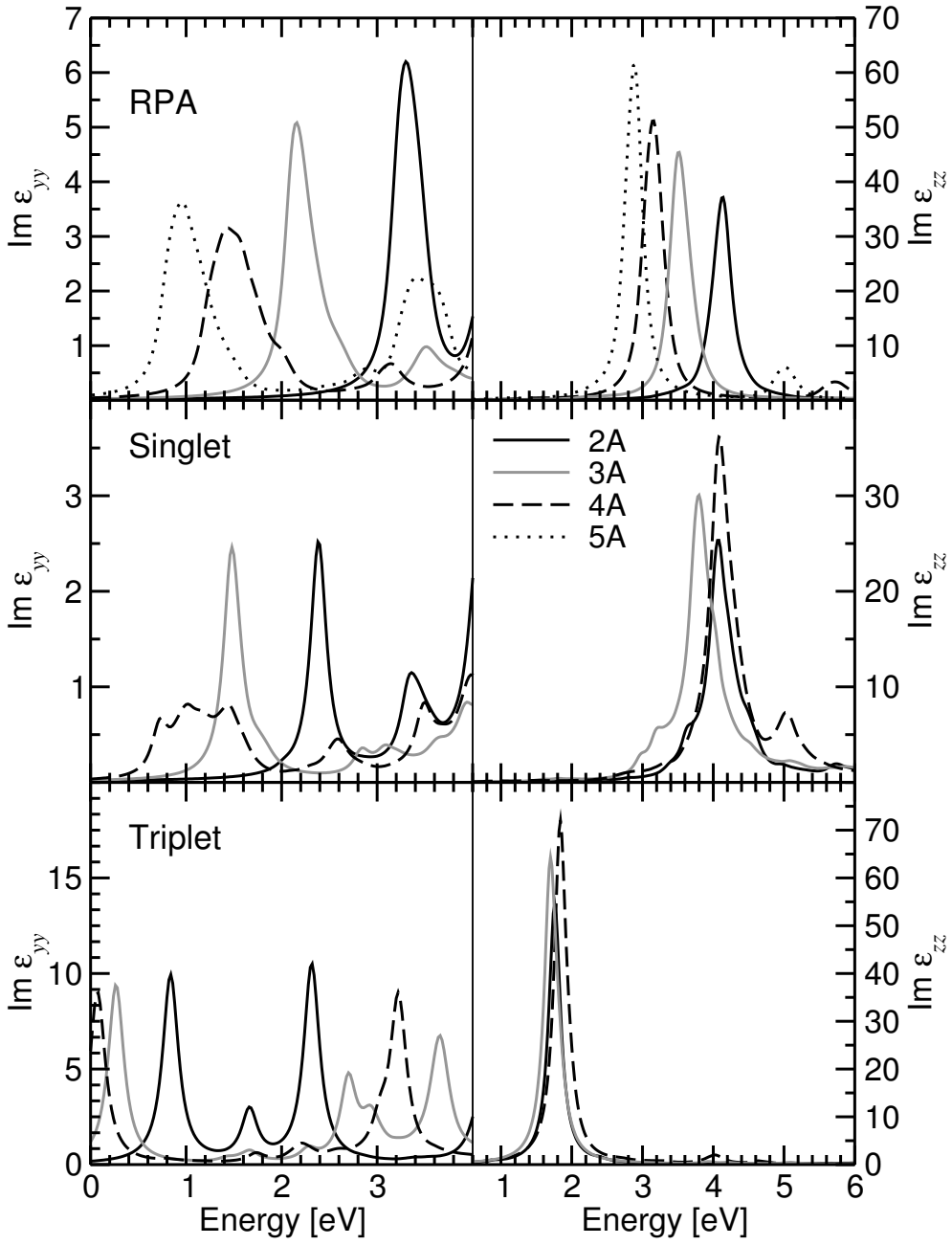

Figure 7.7: y-component (left panels) and z-component (right panels) of the imaginary part of the dielectric tensor calculated using the RPA (upper panels) compared to the solution of the BSE (lower panels) for 2A, 3A, 4A, and 5A. A life-time broadening of 0.1 eV has been included.

monoclinic symmetry as 2A and 3A, it has already been emphasized that the dielectric tensor consists of the three Cartesian diagonal elements plus the xz-component. The dielectric tensor is more complicated for the triclinic materials like 4A and 5A. In this case all off-diagonal components are present as well, but they are small compared to the y- and z-polarized response. According to the explanation in Sec. A.2, the Cartesian components of the dielectric tensor can be related to the crystalline axes. Since this mapping does not significantly change the absorption spectrum in the energy range of interest, only the $Im\ \varepsilon_{yy}$ and the $Im\ \varepsilon_{zz}$ are depicted in Fig. 7.7. The energies of the important transitions extracted from these data are listed in Tab. 6.5 in comparison with experimental values.

Table 7.3: y- and z-polarized response of crystalline 2A, 3A, 4A, and 5A: The peak positions (maxima) of the RPA result, the position of spin singlet (S), and triplet (T) e-h pair, as well as the spin singlet (triplet) exciton binding energy SBE (TBE) and the singlet-triplet (S-T) splitting as a function of the oligomer length. Experimental data concerning the lowest transitions in these material have been taken from Ref. [92] to determine the experimental SBE, TBE and the S-T included for comparison. Note that none of the calculated spectra has been scissors corrected.

	2A	3A	4A	5A	2A	3A	4A	5A
[eV]	y-polarized				z-polarized			
RPA	3.30	2.12	1.44	0.97	4.14	3.52	3.16	2.9
S	2.38	1.48	1.10		4.08	3.80	4.08	
T	0.84	0.26	0.08		1.76	1.70	1.84	
SBE	0.92	0.64	0.37		0.06	-0.28	-0.92	
TBE	2.46	1.86	1.36		2.38	1.82	1.32	
S-T	1.54	1.22	0.99		2.32	2.10	2.24	
exp. S [92]		3.1	2.4					
exp. T [92]		2.1	1.6					
exp. SBE		0.78	0.52					
exp. TBE		2.05	1.63					
exp. S-T		1.27	1.11					

First, we will focus on the RPA result. The lowest optically active transition has weak oscillator strength and is generated by y-polarized light in all four compounds. Compared to the band gap, the optical gap is 0.2 eV larger in 2A, 4A, and 5A, while it is 0.1 eV larger in 3A. As expected from the decrease in the band gap as a function of the oligomer length, the RPA spectrum is correspondingly red-shifted in both polarizations. The overall energy shift of the lowest transition is 2.3 eV within the series from 2A to 5A, whereas the

red-shift of $Im\,\varepsilon_{zz}$ is only 1.2 eV. As already shown above for the band gap and also for the oligomers of PPP [112], the red-shift of the optical gap depends almost linearly on the inverse of the oligomer length n. This finding also applies to $Im\,\varepsilon_{zz}$ as a function of 1/n as illustrated in Fig. 7.8.

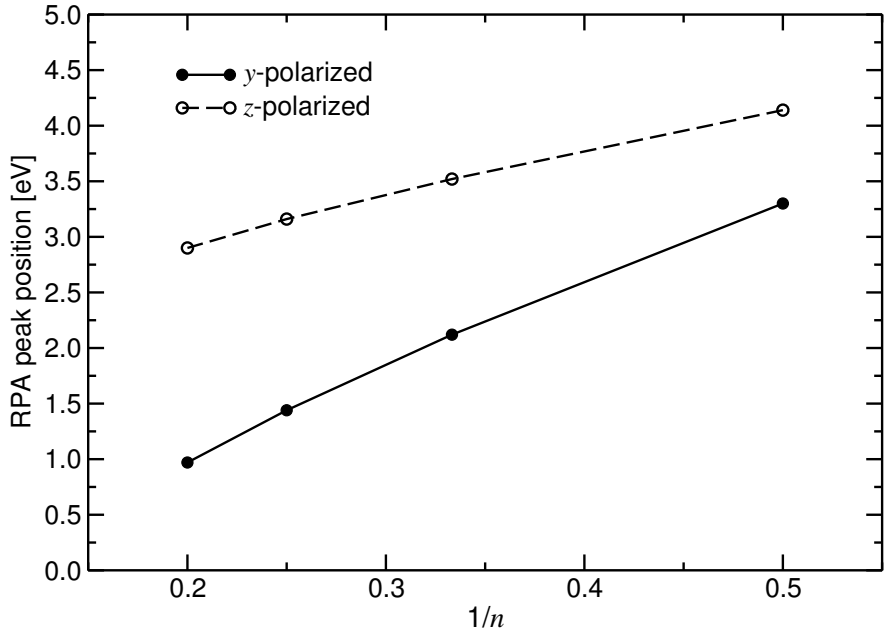

Figure 7.8: RPA peak position of $Im\,\varepsilon_{yy}$ and $Im\,\varepsilon_{zz}$ as a function of 1/n, respectively.

Now the excitonic effects on $Im\,\varepsilon_{yy}$ will be addressed. As a consequence of the attractive Coulomb interaction in the effective Hamiltonian, a strongly bound spin singlet e-h pair is found in 2A, 3A, and 4A below the RPA gap. The corresponding SBE decreases within this series from 0.92 to 0.64 and 0.37 eV, respectively. This reduction of the SBE can be understood in terms of the oligomer length in combination with the enhancement of the dielectric screening. The longer the oligomer is, the more the e-h pair can spread out and thereby the average Coulomb attraction is reduced. At the same time, the screening becomes more effective resulting in a decreased influence of $\hat{H}^{\mathrm{dir}}$. This is also evident in the TBE, since the RPA Hamiltonian and the effective Hamiltonian for the spin triplet exciton differ only in $\hat{H}^{\mathrm{dir}}$ (see Sec. 4.2.3). According to the values given in Tab. 7.3, the TBE reduces from 2.46 eV to 1.36 eV, which is 1.1 eV in total.

Secondly, when talking about spin singlet excitons, also the exchange term $\hat{H}^{\mathrm{x}}$ has to be considered. $\hat{H}^{\mathrm{x}}$ is a repulsive term and counteracts to $\hat{H}^{\mathrm{dir}}$. The effect of $\hat{H}^{\mathrm{x}}$ becomes visible, when the spin singlet and the spin triplet peaks are compared, because they differ only by this part in the effective Hamiltonian.

Since these triplet peaks are less red-shifted compared to the singlet peaks, we can conclude that also the exchange term is weakened with increasing oligomer size. This is again clear in terms of the larger e-h pair distribution as discussed above. However, the exchange interaction between electron and hole decreases only by half of the amount of $\hat{H}^{\mathrm{dir}}$, since the former is not screened, while in the latter the screening is enhanced with n. These findings are reflected in the S-T splitting, which reduces from 1.54 in 2A to 0.99 eV in 4A. The interplay of both terms gives rise to the significantly smaller SBE in 4A compared to that of 2A.

In comparison to experiment the SBE as well as the TBE are in excellent agreement, if the estimated uncertainty in the measurements of roughly $\pm$0.2 eV is taken into account. Besides, the S-T splitting for 3A and 4A perfectly reproduce the values deduced from experiment. This indicates that the calculated relative peak positions of S and T excellently agree with experiment. If the absolute peak positions of S are compared to experimental findings, the self-energy correction Δ_{c} can be determined. Unfortunately, reliable references are available only for crystalline 3A, 4A, and 5A [92]. The Δ_{c} for 3A has already been discussed above. There we have found that the optical gaps are roughly 50% to small. This is also verified in 4A, where the calculated spin singlet exciton energy is 1.1 eV compared to 2.4 eV observed by experiment. Note, the theoretical value has been taken as average over the three maxima that can be distinguished on top of the S peak.

Compared to the y-polarized spectra, pronounced differences are observed in the z-component of the dielectric tensors, when the S and T energies are analyzed. First of all, it is significant that strongly bound spin singlet excitons are not present in the spectrum. For example, the energy of S in 2A is almost identical to that of the corresponding RPA peak resulting in a rather small SBE of 0.06 eV. Therefrom it can be concluded, that the attractive $\hat{H}^{\mathrm{dir}}$ is almost compensated by $\hat{H}^{\mathrm{x}}$. When further looking at the details, it can be seen, that the influence of the $\hat{H}^{\mathrm{dir}}$ as well as the effect of $\hat{H}^{\mathrm{x}}$, which are manifested in the T energy and the S-T splitting, respectively, is not the same as expected from the interpretation of the y-polarized spectra. In both cases, their action decreases between 2A and 3A, but is increased again in 4A. Moreover, the effect of $\hat{H}^{\mathrm{x}}$ is significantly larger than that of $\hat{H}^{\mathrm{dir}}$ as concluded from comparing the changes of T with that of S-T as a function of n. However, since their variations are small compared to the dominating red-shift of the corresponding RPA peaks, a distinct trend is still found when looking at the SBE and TBE. According to the smaller $\hat{H}^{\mathrm{dir}}$, the TBE reduces by roughly 1 eV from 2.38 eV in 2A to 1.32 eV in 4A. In contrast, the strong exchange term further overcompensates the $\hat{H}^{\mathrm{dir}}$ in S resulting in a significant blue-shift of S, when going from 2A to 4A. These differences compared to the y-polarized absorption spectra may be attributed to the change in space group symmetry from monoclinic crystals to triclinic

structures, which is only reflected in this particular polarization. Up to now, a more detailed explanation for this puzzle cannot be given, but the calculation of the exciton wavefunction planned in the future should help to find a solution.

7.3 Conclusions

In this chapter, we have been interested in the question, how the oligomer length n influences the electronic and optical properties of the oligo-acenes. Finally, the most important findings and conclusions are summarized as follows:

- The calculated band structures show that the band dispersion and the band splitting is significantly smaller in the triclinic systems compared to the monoclinic structures. Anthracene exhibits the largest band widths.
- In all four crystals, the topmost valence band as well as the lowest conduction band exhibit their highest band dispersion in directions perpendicular to the long molecular axis. From this it can be expected that the favored channels for electron and hole conduction are perpendicular to this direction.
- The band gaps decrease, when going from naphthalene to pentacene. This reduction depends almost linearly on the inverse of n.
- In all four oligo-acenes, the lowest optically active transition has weak oscillator strength and is generated by a spin singlet exciton, which binding energy significantly decreases with increasing n. It appears in the y-polarized absorption spectrum.
- In contrast, if the light is polarized in the long molecular axis a nearly free (2A) and free (3A, 4A) e-h pair is found. The oscillator strength of this transition is an order of magnitude higher.
- The decreased effect of the Coulomb interaction with longer molecular size can be attributed to a more extended exciton wavefunction as well as to an enhanced screening.

8 Summing Up and Looking Ahead

Life is not easy for any of us. But what of that? We must have perseverance and above all confidence in ourselves. We must believe that we are gifted for something and that this thing must be attained.

Marie Curie

The main goals of the research work presented herein have been the detailed investigation of the role that the intermolecular interactions play in organic molecular crystals and second, the dependence of the opto-electronic properties on the oligomer length. These aims have been achieved by performing highly accurate FP-(L)APW calculations using the local density approximation and the generalized gradient approximation on the first four oligo-acenes, i.e., naphthalene, anthracene, tetracene, and pentacene.

The optimization of the internal molecular orientation in anthracene as a function of pressure revealed how the molecules turn in the unit cell and thus the herringbone stacking is altered by pressure. The change of the herringbone angle turned out to be the dominating pressure effect.

Further, for these optimized anthracene structures the isothermal bulk moduli, the electronic band structures, and the electron densities as a function of the unit cell volume have been calculated. Concerning this task one of the major problems of the LDA, the well-known overbinding effect, which is responsible for the underestimation of the equilibrium volume and thus the overestimation of the bulk modulus has been encountered. In particular, it has been argued that the strength of the hydrogen bond is seriously overestimated in the LDA, but the GGA's successfully compensate for this effect. However, both types of functionals have shortcomings in the description of weak long-range interactions such as the Van der Waals force. Since this interaction is generally believed to be responsible for the bonding in organic molecular crystals, the applicability of the LDA and the GGA xc potentials had to be proven. The

excellent agreement of the theoretical findings concerning the internal geometry of anthracene under pressure with the experimentally determined structure parameters validated that both, the LDA as well as the GGA are able to correctly describe the structural properties of such compounds. Moreover, both, the LDA and the GGA electron distributions clearly show a finite density between the molecules in the unit cell of the investigated oligo-acenes, which increases with pressure due to the enhancement of the intermolecular interactions. These findings support the interpretation that the bonding mechanism in organic molecular crystals is not solely Van der Waals type interaction.

The calculation of the band structures of anthracene as a function of pressure revealed that they are very anisotropically altered. According to the pressure effect on the structural properties, band dispersion and splitting significantly increase resulting in a reduction of the band gap. Further, regarding the reduction of the compressibility of the crystal with increasing pressure the pressure effect on both, structural and electronic properties, is more strongly pronounced in the low pressure range that is between ambient pressure and 3-4 GPa.

Concerning the optical properties of anthracene as a function of pressure, a red-shift of the absorption peaks is obtained due to the reduction of the optical gap, which itself is manifested in the pressure induced changes of the band structure. The calculations of the dielectric matrix including e-h interactions presented in this work clearly demonstrate that in one material, depending on the polarization of the probing light with respect to the crystalline axes the physics underlying the optical response is different: The lowest transition is generated by a bound e-h pair (spin singlet exciton), while an excitation higher in energy can be traced back to free charge carriers. This fact is an important contribution to the ongoing discussion, whether optical absorption processes in such materials are due to bound excitons or free electron-hole pairs. Compared to polymers, e.g., poly-acetylene, the exciton binding energies in the oligo-acenes are roughly by a factor of 10 larger. The exciton binding energy of the bound e-h pair in anthracene is decreased by pressure due to the enhancement of the dielectric screening. The self-energy correction that is necessary to bring theory in agreement with experiment has been deduced by the comparison of the calculated optical gaps with measured spectra. Thereby it turned out that this correction is pressure dependent, but the ratio between the theoretical and experimental optical gaps up to 4 GPa is found to be a constant factor of approximately 0.5 independent of pressure. This allows to estimate the optical gap of other molecular crystals without performing the exact, but expensive GW calculations for the self-energy correction. Unfortunately, most of the published optical absorption experiments on anthracene under pressure have only measured the b-axis polarized spectrum and a polarization direction perpendicular, which is not well defined. For this reason it is pointed out

that the c-component of the dielectric function is the strongest one, whereas the a-component is nearly negligible. Therefore, the performance of optical absorption measurements of anthracene under pressure with light polarized along the crystalline c-axis would be highly appreciated. In general, absorption measurements for well defined polarization directions could further help to clarify the situation in different materials.

When the band structures of the first four members within the oligo-acene family are compared, the monoclinic materials, namely naphthalene and anthracene, can be clearly distinguished from the triclinic tetracene and pentacene in terms of band widths and band splitting. The obtained values for the band widths range from 0.1 to 0.3 eV and decrease as a function of the oligomer length. The band dispersion of the monoclinic systems is significantly larger than that of the triclinic ones and reaches a maximum in anthracene. This has also been found to be valid for the oligomers of poly-*para*-phenylene. Therefore, the effective charge carrier mobilities are expected to be higher in naphthalene and anthracene than in tetracene and pentacene. The evaluation of the band widths in high symmetry directions of the crystals revealed that the favored electron and hole conduction channels are perpendicular to the long molecular axes in all four compounds. In particular, it is the direction along the a-axis, which is chosen by the electrons in naphthalene and anthracene. The absolute magnitude of the calculated band gaps of the oligo-acenes is in fact underestimated by theory, but the reduction within the series completely reproduces the experimental data available in literature. As already found for the oligomers of poly(para-phenylene), the band gap depends linearly on the inverse oligomer length within the investigated series.

Concerning the optical properties of the oligo-acenes, it is found that the lowest optically active transition appears in the short axis polarized spectrum. In all four structures, this absorption has weak oscillator strength and is generated by a spin singlet exciton. Analogously to the band gap, the spin singlet exciton energy is shifted to the red as a function of oligomer length, in particular linearly with the inverse molecular size. In contrast, the optical response due to light polarized in the long molecular axis exhibits a nearly free (naphthalene) or a free (anthracene, pentacene) e-h pair. It turned out that the excitonic effects become weaker, when going from naphthalene to pentacene. Thus the singlet and the triplet binding energy as well as the singlet-triplet splitting significantly decrease with increasing oligomer length. This is explained in terms of the decreased effect of the Coulomb interaction, which can be attributed to a more extended exciton wavefunction as well as to the enhanced screening.

The future perspectives are summarized as follows:

- In order to deeper understand the transport properties of organic molecular crystals the thorough analysis of the effective charge carrier masses

deduced from the calculated band structures is intended.

- The ab-initio description of other herringbone stacked molecular crystals could help to gain insight in the origin of this special type of geometry.
- The detailed comparison of the electro-optical properties of oligo-acenes, oligo-phenylenes and oligo-thiophenes will allow to figure out possible advantages of one class of compounds compared to the other with respect to their applicability in devices.
- The investigation of oligo-acene films regarding their transport and optical properties should help to tune them according to their needs for technical applications.

Epilogue

Science is like sex: sometimes something useful comes out, but that is not the reason we are doing it.

Richard P. Feynman

Part III

Appendix

A Computational Details

The FP-LAPW formalism as implemented in the **WIEN2k** code [45] has been used for the SCF computations. In particular, the APW+lo extension [74] to the **WIEN2k** package has been utilized for the internal structure optimization of anthracene under high pressure. Compared to the conventional LAPW method, the APW+lo method permits to decrease the plane wave cut-off $R_{\mathrm{MT}}K_{\mathrm{max}}$. Thus the size of the Hamilton matrix, and therefore the computational effort is considerably reduced. Exchange and correlation effects have been treated by the LDA [46] and the GGA-PBE [50]. Whereas both, the LDA and the GGA-PBE have been used for the pressure study on anthracene, the GGA was employed for the calculation of the oligo-acenes. In the following the **WIEN2k** specific parameters, which have been kept constant throughout the calculations of the oligo-acenes are summarized.

A.1 (L)APW Specific Parameters

The ground state properties of four oligo-acenes 2A, 3A, 4A, and 5A have been computed on the basis of the **WIEN2k** input parameters set according to the values listed in Tab. A.1. The muffin tin radii R_{MT} have been chosen in the way that the atomic spheres are as large as possible, but sphere overlap is avoided even when pressure is applied. For example, in anthracene R_{MT} has been fixed to 1.28 a.u. for carbon atoms and to 0.75 a.u. for hydrogen atoms, respectively. Within the APW+lo method, an $R_{\mathrm{MT}}K_{\mathrm{max}}$ of 3.0 Ry for H turned out to be sufficient for the accurate calculation of the atomic forces and the total energy. By keeping $R_{\mathrm{MT}}K_{\mathrm{max}}$ for H constant throughout the series, the corresponding value for the C atoms increases from 5.08 to 5.40 Ry when going from 2A to 5A according to the setting of the R_{MT} (C). The resulting number of plane waves increases from roughly 2700 in 2A to approximately 6500 in 5A. The $\mathbf{k}$-space integrations by the improved tetrahedron method [115] have been performed on a grid of 6 (5) $\mathbf{k}$-points in the IBZ. The atomic positions have been relaxed such that the forces acting on each atom were less than 2 mRy/a.u. in magnitude. In each SCF cycle, the atomic forces were

converged better than 1 mRy/a.u. resulting in a total energy convergence of 0.1 mRy. The numbers listed in the last five rows of Tab. A.1 give the details regarding the computational demand of these systems and should illustrate, how extensive they have been for FP-(L)APW calculations.

Table A.1: WIEN2k specific parameters for the oligo-acenes: naphthalene, anthracene, tetracene, and pentacene. R_{MT}, $R_{\mathrm{MT}}K_{\mathrm{max}}$, and G_{max} denote the muffin tin radius, the plane wave cut off, and the energy cut off for the Fourier expansion of the potential and the charge density, respectively.

	naphthalene	anthracene	tetracene	pentacene
$R_{\mathrm{MT}}K_{\mathrm{max}}$ (C) [Ry]	5.08	5.12	5.38	5.40
$R_{\mathrm{MT}}K_{\mathrm{max}}$ (H) [Ry]	3.00	3.00	3.00	3.00
R_{MT} (C) [a.u.]	1.27	1.28	1.22	1.26
R_{MT} (H) [a.u.]	0.75	0.75	0.68	0.70
G_{max} [Ry]	21.00	21.00	21.00	21.00
$\mathbf{k}$-points in IBZ	6	6	5	6
# of inequiv. atoms	9	12	30	36
atoms per unit cell	36	48	60	72
matrix size at Γ	2736	3622	6042	6540
# of local orbitals	116	160	180	222
# of occupied bands	48	66	84	102

The band structures $E(\mathbf{k})$ have been computed on discrete $\mathbf{k}$-meshes illustrated in Figs. 6.6 and 7.1 using approximately 120 $\mathbf{k}$-points on the whole path. The 3D electron densities have been computed by XCrySDen [1] on a grid of 50$\times$50 points in the (ab)-plane, while between 80 and 100 stacks have been calculated in the c-direction.

A.2 The Dielectric Tensor

A.2.1 Within the RPA

In case of anthracene, the dielectric tensor within the RPA has been calculated as a function of pressure starting from the internal geometry optimized structures. The momentum matrix elements that provide the selection rules for the frequency dependent complex dielectric tensor have been computed on a dense grid of 413 irreducible $\mathbf{k}$-points in an energy window from plus to minus 1.5 Ry with respect to the Fermi level. This number of $\mathbf{k}$-points corre-

sponds to a 13×14×9 $\mathbf{k}$-mesh. The results obtained with this mesh served as reference for the BSE calculations. According to the monoclinic symmetry of the crystal, the dielectric tensor consists of the Cartesian diagonal elements $Im\ \varepsilon_{zz}$, $Im\ \varepsilon_{yy}$, and $Im\ \varepsilon_{xx}$, and the additional off-diagonal xz-component. In order to transform the Cartesian components into those corresponding to the crystalline coordinates, the monoclinic Bravais matrix in real space

$$\hat{B}^{\mathrm{M}} = \begin{pmatrix} \sin\beta & 0 & \cos\beta \\ 0 & 1 & 0 \\ 0 & 0 & 1 \end{pmatrix}$$

has been utilized. $\hat{B}^{M}$ implies that the Cartesian axes y and z are equivalent to the crystalline b- and c-axis, while the a-axis deviates from x by the monoclinic angle β. Therefore, $Im\ \varepsilon_{yy}$ and $Im\ \varepsilon_{zz}$ are identical to $Im\ \varepsilon_{bb}$ and $Im\ \varepsilon_{cc}$, respectively. The former corresponds to the optical response generated by light with the electric field vector almost parallel to the short molecular axis, whereas the latter defines the response polarized in the direction of the long molecular axis. For the correspondence of these axes to the crystalline axes it is referred to Fig. 5.2. The a-component of the dielectric tensor has been extracted according to the following transformation:

$$Im\ \varepsilon_{aa} = \begin{pmatrix} \sin\beta & 0 & \cos\beta \end{pmatrix} . \begin{pmatrix} Im\ \varepsilon_{xx} & 0 & Im\ \varepsilon_{xz} \\ 0 & Im\ \varepsilon_{yy} & 0 \\ Im\ \varepsilon_{xz} & 0 & Im\ \varepsilon_{zz} \end{pmatrix} . \begin{pmatrix} \sin\beta \\ 0 \\ \cos\beta \end{pmatrix}$$

It turned out, that the a-component contains a major z-fraction and a minor x-fraction, when the monoclinic angle β equals 124.63°.

Compared to the monoclinic materials 2A and 3A, in 4A and 5A only the c-axis remains equivalent to the Cartesian z-axis. According to the triclinic symmetry, all off-diagonal terms of the Cartesian dielectric tensor, i.e., the xy-, xz- and yz-components, are different from zero. Analogous to the transformation in the monoclinic case, the corresponding triclinic Bravais matrix

$$\begin{aligned}
\hat{B}^{\mathrm{T}}_{11} &= \sin\left(\arccos(\cos\gamma - \cos\alpha\cos\beta)/\sin\alpha/\sin\beta\right)\sin\beta \\
\hat{B}^{\mathrm{T}}_{12} &= \cos\left(\arccos(\cos\gamma - \cos\alpha\cos\beta)/\sin\alpha/\sin\beta\right)\sin\beta \\
\hat{B}^{\mathrm{T}}_{12} &= \cos\beta \\
\hat{B}^{\mathrm{T}}_{21} &= 0 \\
\hat{B}^{\mathrm{T}}_{22} &= \sin\alpha \\
\hat{B}^{\mathrm{T}}_{23} &= \cos\alpha \\
\hat{B}^{\mathrm{T}}_{31} &= 0 \\
\hat{B}^{\mathrm{T}}_{32} &= 0 \\
\hat{B}^{\mathrm{T}}_{33} &= 1
\end{aligned}$$

has been utilized to project the Cartesian dielectric tensor onto the crystalline axes. In Fig. A.1 the Cartesian diagonal elements of the imaginary part of the dielectric tensor $Im\,\varepsilon$ and their transformations into the components along the crystalline axes are depicted. The Cartesian off-diagonal terms are minor compared to the diagonal elements and therefore not shown. It is important to note, that the a- and b-components are almost identically to their Cartesian counterparts, particularly in the low energy part of the spectrum, where the lowest optical excitations appear. Only at the position of the z-polarized absorption, the a- and b-components are significantly enhanced compared to the x- and y-polarized response indicating that they contain also a strong z-fraction.

These findings allow for the conclusion, that the Cartesian diagonal components of the dielectric tensor are a very good approximation for the optical response polarized along the crystalline axes, particularly in the energy range of interest. For this reason, the transformation of the Cartesian components has been omitted for the materials under investigation.

A.2.2 By solving the BSE

Convergence tests for PA revealed that an $R_{\mathrm{MT}}K_{\max}$ of 2.3 Ry for H is sufficient to obtain reasonable e-h interaction matrix elements [78]. The muffin tin radii R_{MT} for C and H used for the BSE calculations are the same as given in Tab. A.1. The resulting $R_{\mathrm{MT}}K_{\max}$ values of C are 3.89, 3.93, 4.13, and 4.14 for 2A, 3A, 4A, and 5A, respectively. In order to keep the computation times tolerable, a 4 $\times$ 4 $\times$ 4 $\mathbf{k}$-grid has been chosen to calculate the optical dipole matrix elements $\langle v\mathbf{k}|p_i|c\mathbf{k}\rangle$ entering the dielectric function given in Eq. 4.4. The quality of this $\mathbf{k}$-mesh has been tested by comparison of the spectrum excluding e-h interactions with the previous RPA result for anthracene (see Appendix B). For the screened Coulomb interaction $W(\mathbf{r},\mathbf{r}')$ as given in Eq. 4.11 the dielectric matrix $\epsilon_{\mathbf{G}\mathbf{G}'}(\mathbf{q})$ of 2A and 3A (4A and 5A) has been computed on a grid shifted by 30 (36) independent $\mathbf{q}$ vectors resulting in 2080 $\mathbf{k}\mathbf{k}'$-pairs. For the computation of $\epsilon_{\mathbf{G}\mathbf{G}'}(\mathbf{q})$, $W(\mathbf{r},\mathbf{r}')$, and $\bar{v}(\mathbf{r},\mathbf{r}')$, the convergence in terms of the number of $\mathbf{G}$ vectors, which is controlled by the $G_{\max}$ parameter, turned out to be different. Therefore, $G_{\max}$ has been set to 2.0 Ry, 1.5 Ry, and 2.5 Ry, respectively for these quantities. The energy window, which determines the number of occupied and unoccupied states considered to compute the screening, covered the range from -7.0 Ry to 8.0 Ry. The e-h matrix elements of H^{eff} have been calculated for the 2080 $\mathbf{k}\mathbf{k}'$-pairs and including a maximum of 14 valence and 14 conduction bands. The convergence with respect to the number of valence and conduction bands considered has been checked. For these tests it is referred to Appendix B. In all linear optical response calculations, a life-time broadening of 0.1 eV has been applied to obtain smooth optical spectra.

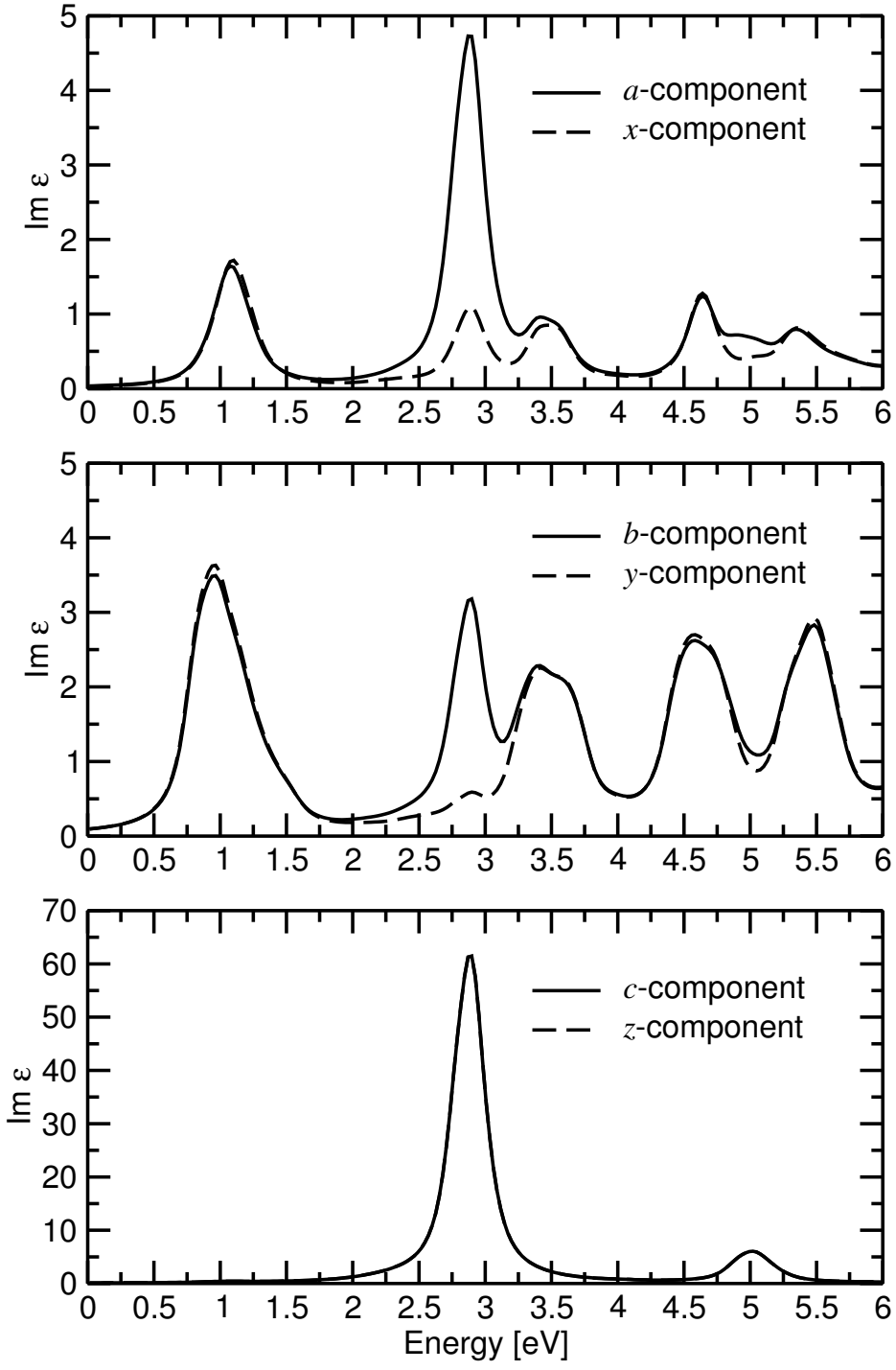

Figure A.1: Pentacene: The Cartesian diagonal elements of the imaginary part of the dielectric tensor and their transformations into the components along the crystalline axes.

B Convergence Tests

B.1 Brillouin Zone Sampling

The calculation of the dielectric tensor using the RPA has been performed on a dense 13×14×9 mesh of 413 $\mathbf{k}$-points, whereas within the BSE formalism only a 4 × 4 × 4 $\mathbf{k}$-grid has been chosen to calculate the optical dipole matrix elements. In the following plots, Figs. B.1 and B.2, the RPA spectra of anthracene at various pressures computed on the dense and coarse $\mathbf{k}$-grid are compared for the two main polarizations. The coarse $\mathbf{k}$-mesh yields reasonable results up to 10.2 GPa. The peak positions obtained with the fine mesh are well reproduced, particularly in the low pressure region of the b-polarized spectra. The theoretical error at higher pressures does not exceed 0.1 eV. Besides, the peak positions completely agree within 0.02 eV up to 10.2 GPa in case of the c-component. Only the peak height is slightly underestimated by the coarse mesh.

B.2 The Number of Valence and Conduction Bands

For anthracene, the convergence with respect to the number of valence and conduction bands considered in Eq. (4.5) downwards and upwards from the Fermi level has been tested at ambient pressure. The findings are depicted in Fig. B.3. The matrix size of the e-h Hamiltonian rapidly increases with that number, as well as with the number of $\mathbf{k}$-points. Considering 14 valence and 14 conduction states for the mesh of 64 $\mathbf{k}$-points yields a 12544×12544 matrix for $\hat{H}^{\mathrm{eff}}$. Since the differences compared to the results obtained with 12 bands are minor, we conclude that we have reached convergence.

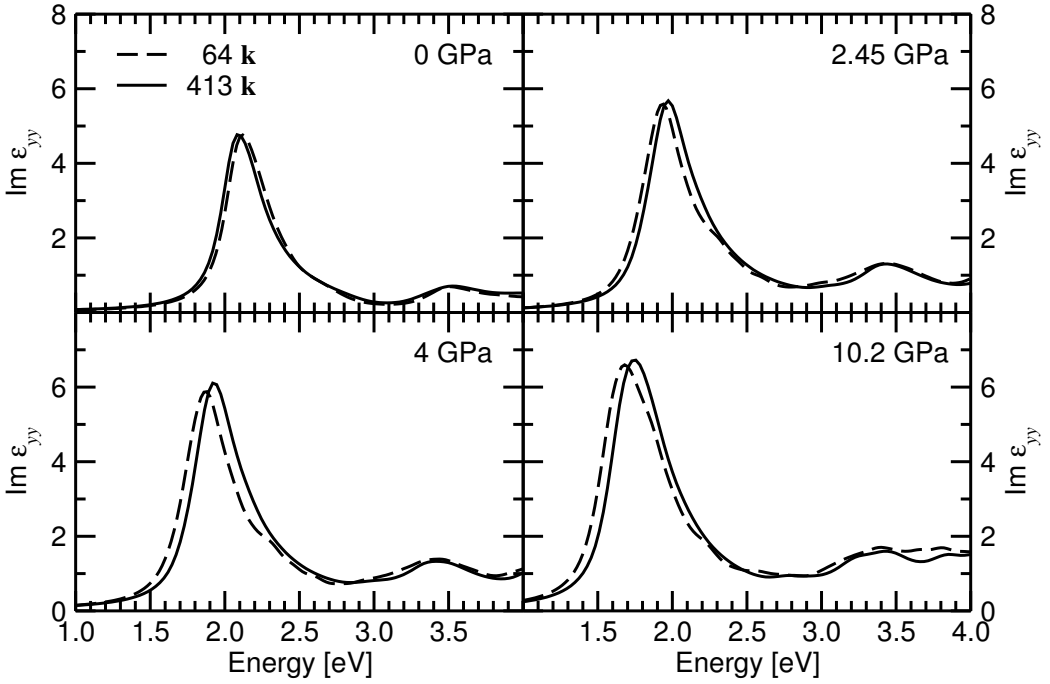

Figure B.1: The b-component of the imaginary part of the dielectric function at 0, 2.45, 4, and 10.2 GPa calculated on a grid of 64 $\mathbf{k}$-points (dashed line) and 413 $\mathbf{k}$-points (solid line), respectively. A life-time broadening of 0.1 eV has been included.

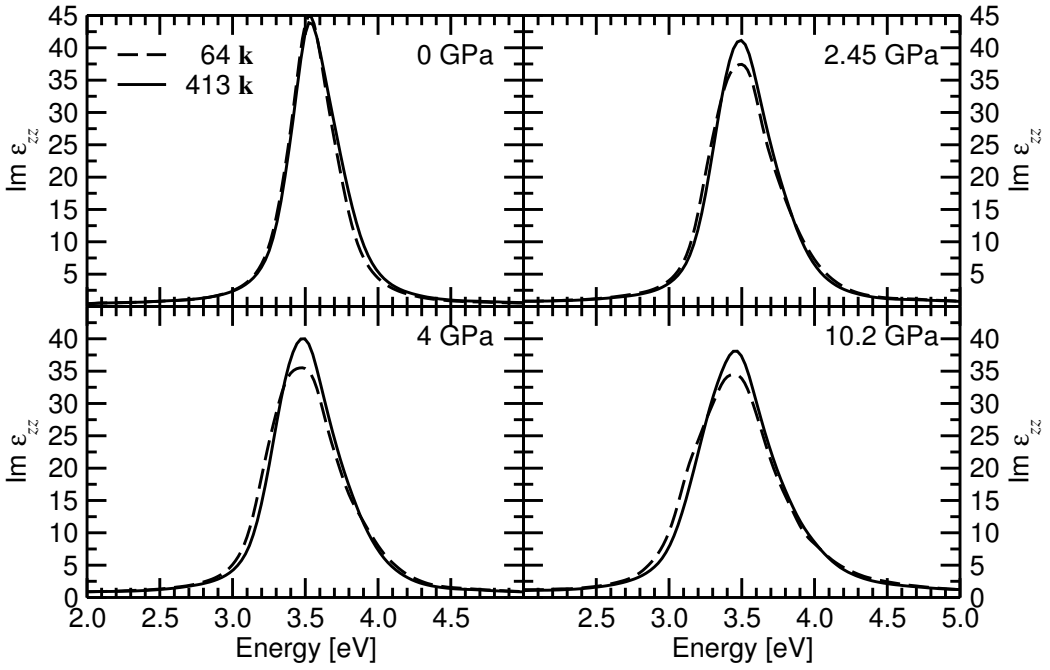

Figure B.2: Analogous to Fig. B.1, but the c-component is shown.

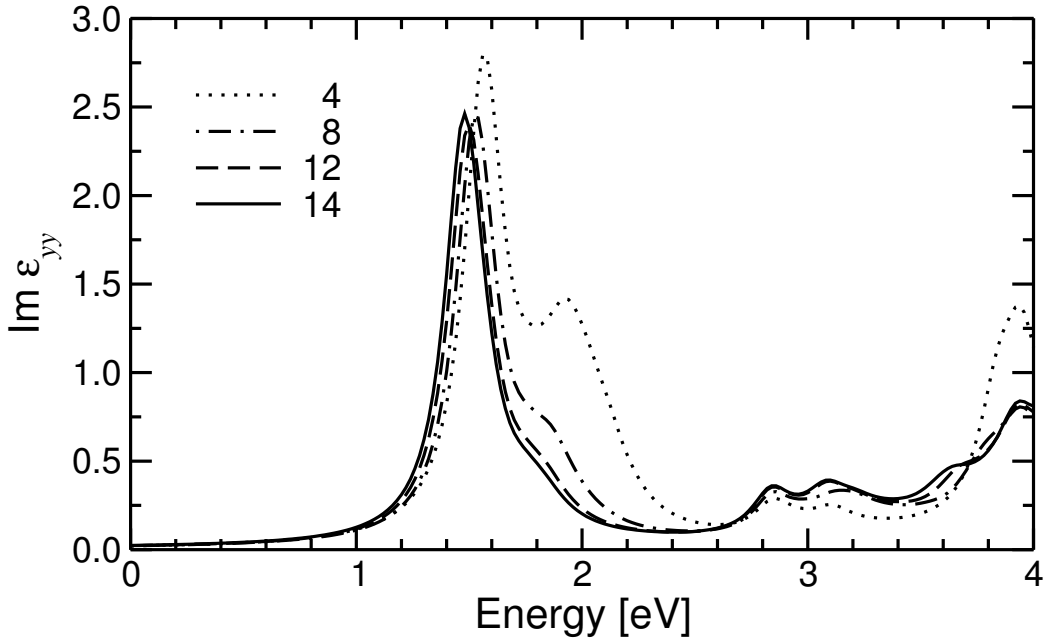

Figure B.3: The b-component of the imaginary part of the dielectric function at ambient pressure. The effective e-h Hamiltonian has been set up using 4, 8, 12, and 14 valence and the same number of conduction bands, respectively. A life-time broadening of 0.1 eV has been included.

B.3 Coulomb Screening

Further, the results obtained with the screening methods described in Sec. 4.2 are compared for this case. Figure B.4 illustrates that the b-component of the imaginary part of the dielectric function is significantly changed when the approximations for the screened interaction given by Eqs. (4.12) and (4.13) are utilized instead of the full matrix given in Eq. (4.11). The position of the lowest spin singlet exciton is found at 1.7 eV (diagonal part, constant tensor) or 1.5 eV (full matrix). Thus the approximations underestimate the exciton binding energy by 0.2 eV.

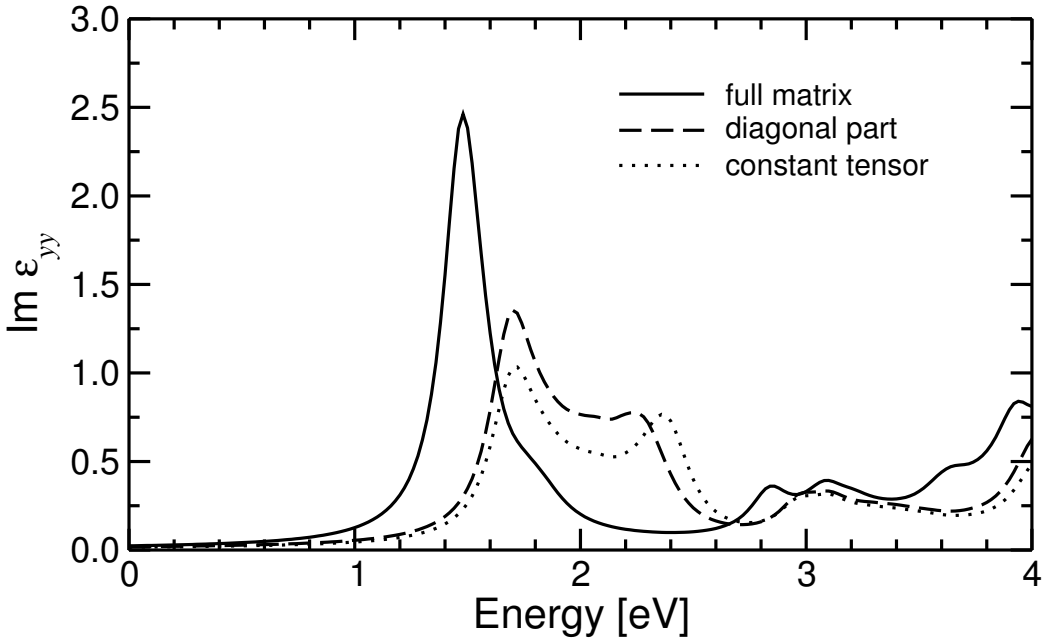

Figure B.4: The $Im\ \varepsilon_{bb}$ at ambient pressure. The results obtained by Eqs. (4.11), (4.12), and (4.13) for the screened Coulomb interaction are compared. A life-time broadening of 0.1 eV has been taken into account.

‖C More Structural Information

C.1 Experimental Data Sets

In order to test, whether the internal geometry optimization as described in Sec. 5.2 depends on the xc functional, both, the LDA and the GGA-PBE have been used to calculate the optimized angles θ, χ, and δ in the low pressure range. These computations were based on lattice constants observed by X-ray powder diffraction experiments with energy dispersive detection conducted at the *DESY Hasylab* in Hamburg [116]. Subsequently, experiments utilizing angle dispersive detection and a pressure medium additional to the sample powder in order to guarantee hydrostatic pressure conditions were performed up to 20 GPa at *Photon Factory* (PF KEK) in Tsukuba, Japan [88, 89]. The latter series of measurements turned out to be of excellent quality and more reliable. In particular, by comparison of DESY and PF data it was found that the pressure determination during the DESY experiments was inaccurate. For this reason, the PF data (pressure versus unit cell volume) were used to construct a fit equation, which in turn served for the re-evaluation of the pressure corresponding to the unit cell volume observed with the experiments conducted at DESY. I.e., the DESY lattice parameters were taken to calculated the volume. This volume has been plugged in the fit equation based on the PF data as shown in Fig. C.1. This procedure revealed, that the DESY data set covers the pressure region from 0 to approximately 4 GPa. The ongoing calculations up to 10 GPa have been solely based on PF lattice parameters as given in Tab. 5.2 in Sec. 5.1.2 and the LDA.

C.2 Enlarged Anthracene Structures

On the basis of the DESY data set, the internal structure optimization has been performed utilizing the LDA as well as the GGA. The analysis of corresponding total energies as a function of the unit cell volume yields the following: The LDA finds a theoretical equilibrium volume that is 11 % smaller than the experimen-

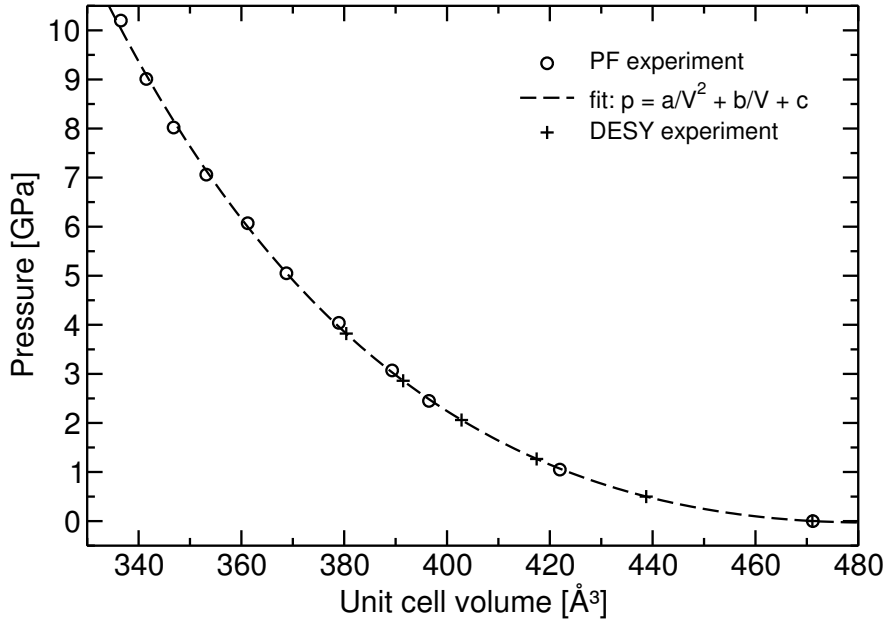

Figure C.1: The fit equation p = 53.58-51717.6/V+12472700/V^2 (dashed line) of the PF data set (open circles) used for the re-evaluation of the pressure corresponding to the unit cell volume obtained by the experiments at DESY (cross).

tal volume due to its well-known overbinding effect. In contrast, a parabolic fit of the GGA total energies corresponding to the contracted structures suggests an equilibrium volume larger than the experimental volume at ambient pressure. To verify this, the lattice parameters as given in Tab. 5.2 and the experimentally determined angles [88] specifying the internal geometry have been extrapolated in order to obtain good starting geometries for the expanded structures with unit cell volumes increased by 4, 7, 14, and 24%, respectively. The corresponding fits are shown in Figs. C.2 and C.3. The lattice parameters extracted from these fits are summarized in Tab. C.1.

Based on this structural data, θ, χ, and δ have been optimized for the expanded systems by the same procedure as for the contracted unit cells (see Sec. 5.2). The findings of this internal geometry optimization are shown in Fig. C.3 in addition to the initial fit for these angles, which agree reasonably with the trend of the fit function.

Table C.1: Anthracene lattice parameters a, b, c, β, the unit cell volume $V = a{\cdot}b{\cdot}c{\cdot}\sin\beta$, and the three angles, respectively, of the expanded structures obtained by fitting the experimental data from Ref. [88]. These angles have been used as initial guess for the internal structure optimization with the GGA.

a [Å]	b [Å]	c [Å]	β [deg]	V [Å^3]	θ [deg]	χ [deg]	δ [deg]
8.750	6.075	11.282	124.30	493.94	121.37	28.76	10.37
8.884	6.114	11.375	124.13	509.09	118.77	28.17	8.74
9.180	6.190	11.594	123.74	542.42	112.55	26.53	4.55
9.610	6.282	11.962	123.14	590.91	102.14	23.64	0.00

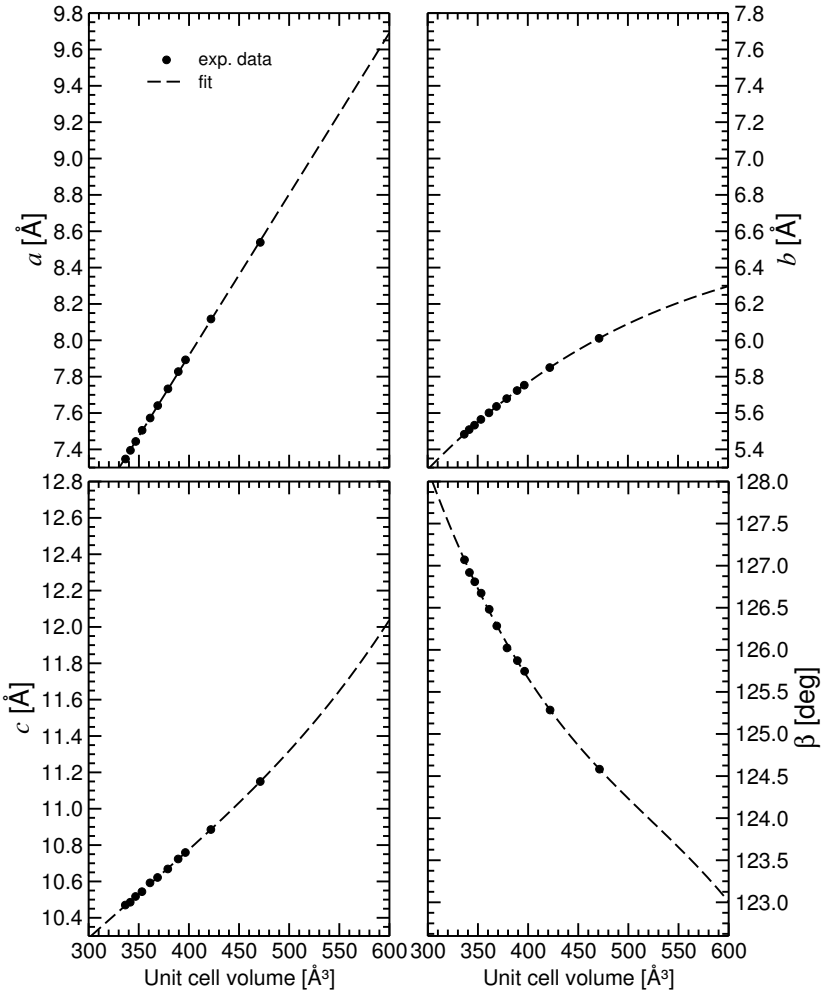

Figure C.2: The experimentally observed lattice parameters of anthracene as a function of volume (symbols) and the corresponding fits (dashed line).

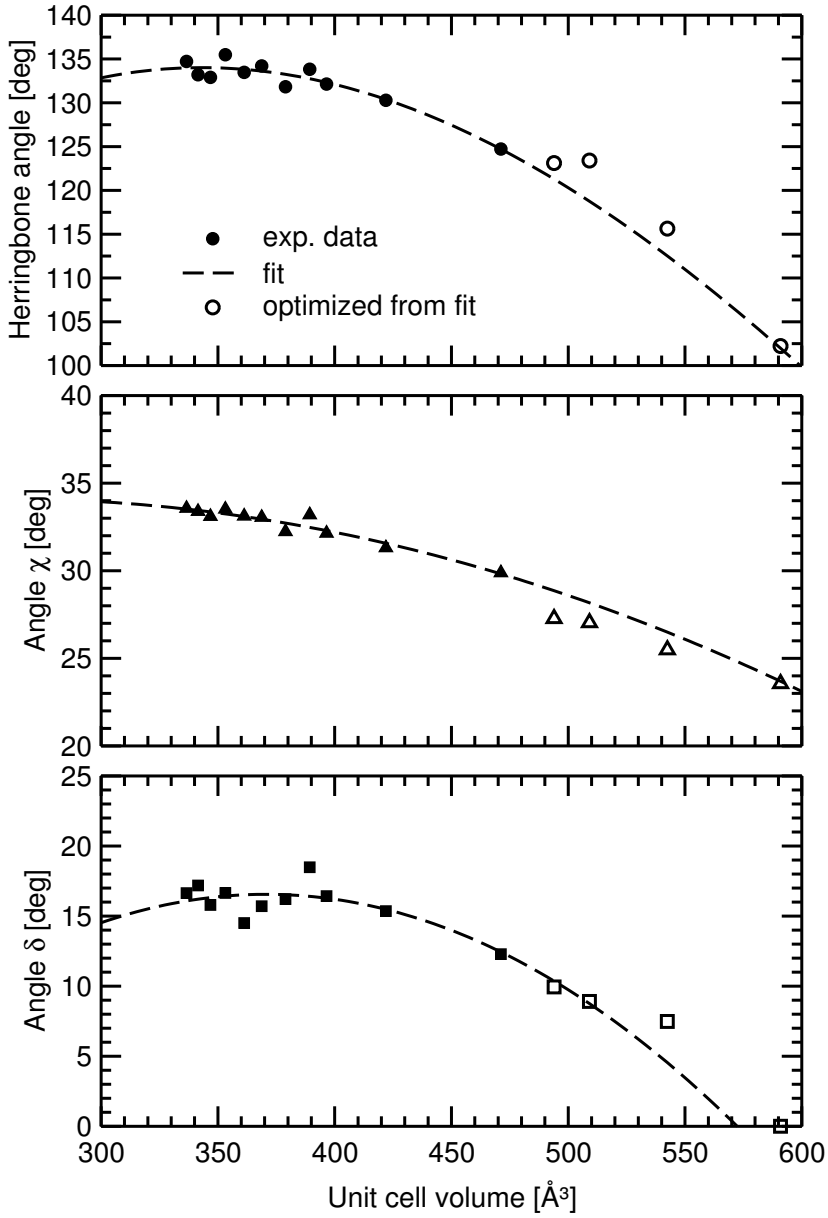

Figure C.3: The experimentally observed angles θ, χ, and δ of anthracene as a function of volume [88] (symbols) and the corresponding fit (dashed line). In addition, the calculated GGA values (open symbols) obtained from the internal geometry optimization described in Sec. 5.2.

Bibliography

[1] A. Kokalj, *J. Mol. Graphics Modelling* **17**, 176 (1999).

[2] H. Shirakawa, E. J. Louis, A. G. MacDiarmid, C. K. Chiang, A. J. Heeger, *J.C.S. Chem. Comm.* p. 578 (1977).

[3] C. K. Chiang, *et al.*, *Phys. Rev. Lett.* **39**, 1098 (1977).

[4] A. J. Heeger, *Synth. Met.* **125**, 23 (2002).

[5] R. Friend, *et al.*, *Nature* **397**, 121 (1999).

[6] H. Koezuka, A. Tsumura, T. Ando, *Synth. Met.* **18**, 699 (1987).

[7] F. Garnier, G. Horowitz, X. Peng, D. Fichou, *Adv. Mater.* **2**, 592 (1990).

[8] G. Horowitz, *Adv. Mater.* **10**, 365 (1998).

[9] F. Garnier, *Chem. Phys.* **227**, 253 (1998).

[10] N. S. Sariciftci, L. Smilowitz, A. J. Heeger, F. Wudl, *Science* **258**, 1474 (1992).

[11] M. Granström, *et al.*, *Nature* **395**, 257 (1998).

[12] C. W. Tang, S. A. VanSlyke, *Appl. Phys. Lett.* **51**, 913 (1987).

[13] D. Braun, A. J. Heeger, *Appl. Phys. Lett.* **58**, 1982 (1991).

[14] A. Dodabalapur, L. Torsi, H. E. Katz, *Science* **268**, 270 (1995).

[15] D. Kim, H. Cho, C. Y. Kim, *Prog. Polym. Sci.* **25**, 1089 (2000).

[16] A. N. Aleshin, *et al.*, *Thin Solid Films* **417**, 57 (2002).

[17] K. Pichler, R. H. Friend, D. Parker, W. J. Feast, *J. Phys. Cond. Mat.* **3**, 3007 (1991).

[18] P. Puschnig, C. Ambrosch-Draxl, *Phys. Rev. Lett.* **89**, 56405 (2002).

[19] D. M. Ivory, *et al.*, *J. Chem. Phys.* **71**, 1506 (1979).

[20] G. Grem, G. Leditzky, B. Ullrich, G. Leising, *Adv. Mater.* **4**, 36 (1992).

[21] C. Ambrosch-Draxl, J. A. Majewski, P. Vogl, G. Leising, *Phys. Rev. B* **51**, 9668 (1995).

[22] P. W. M. Blom, M. C. J. M. Vissenberg, *Mat. Science and Engineering* **27**, 53 (2000).

[23] D. A. Dos Santos, J. L. Brédas, *Synth. Met.* **67**, 315 (1994).

[24] E. Mulazzi, A. Ripamonti, J. Wery, B. Dulieu, S. Lefrant, *Phys. Rev. B* **60**, 16519 (1999).

[25] A. Ferretti, A. Ruini, E. Molinari, M. J. Caldas, *Phys. Rev. Lett.* **90**, 86401 (2003).

[26] A. Ruini, M. J. Caldas, G. Bussi, E. Molinari, *Phys. Rev. Lett.* **88**, 206403 (2002).

[27] C. Hosokawa, H. Higashi, T. Kusumoto, *Appl. Phys. Lett.* **62**, 3238 (1993).

[28] J. Cornil, D. Beljonne, J. L. Brédas, *J. Chem. Phys.* **103**, 834 (1995).

[29] P. Puschnig, C. Ambrosch-Draxl, *Phys. Rev. B* **60**, 7891 (1999).

[30] L. Torsi, A. Dodabalapur, L. J. Rothberg, A. W. P. Fung, H. E. Katz, *Science* **272**, 1462 (1996).

[31] K. Waragai, H. Akimichi, S. Hotta, H. Kano, H. Sakaki, *Phys. Rev. B* **52**, 1786 (1995).

[32] H. E. Katz, L. Torsi, A. Dodabalapur, *Chem. Mater.* **7**, 2235 (1995).

[33] S. F. Nelson, Y.-Y. Lin, D. J. Gundlach, T. N. Jackson, *Appl. Phys. Lett.* **72**, 1854 (1998).

[34] L. Torsi, *et al.*, *Sol. State Electronics* **45**, 1479 (2001).

[35] C. D. Dimitrakopoulos, S. Purushothaman, J. Kymissis, A. Callegari, J. M. Shaw, *Science* **283**, 822 (1999).

[36] S. Nelson, Y.-Y. Lin, D. J. Gundlach, T. N. Jackson, *Appl. Phys. Lett.* **72**, 1854 (1998).

[37] D. Moses, C. Soci, P. Miranda, A. J. Heeger, *Chem. Phys. Lett.* **350**, 531 (2001).

[38] Z. Shuai, D. Beljonne, R. J. Silbey, J. L. Brédas, *PRL* **84**, 131 (2000).

[39] J. S. Wilson, *et al.*, *Nature* **413**, 828 (2001).

[40] D. Moses, J. Wang, A. J. Heeger, N. Kirova, S. Brazovski, *Synth. Met.* **125**, 93 (2002).

[41] J.-W. van der Horst, P. A. Bobbert, M. A. J. Michels, G. Brocks, P. J. Kelly, *Phys. Rev. Lett.* **83**, 4413 (1999).

[42] G. R. Desiraju, A. Gavezzotti, *Acta Cryst. B* **45**, 473 (1989).

[43] P. Hohenberg, W. Kohn, *Phys. Rev.* **136**, B864 (1964).

[44] W. Kohn, L. J. Sham, *Phys. Rev.* **140**, A1133 (1965).

[45] P. Blaha, K. Schwarz, G. K. H. Madsen, D. Kvasnicka, J. Luitz, *WIEN2k, An Augmented Plane Wave + Local Orbitals Program for Calculating Crystal Properties* (Vienna University of Technology, Vienna, 2001).

[46] D. M. Ceperley, B. J. Alder, *Phys. Rev. Lett.* **45**, 566 (1980).

[47] J. P. Perdew, Y. Wang, *Phys. Rev. B* **45**, 13244 (1992).

[48] J. P. Perdew, *Phys. Rev. B* **33**, 8822 (1986).

[49] J. P. Perdew, *et al.*, *Phys. Rev. B* **46**, 6671 (1992).

[50] J. P. Perdew, K. Burke, M. Ernzerhof, *Phys. Rev. Lett.* **77**, 3865 (1996).

[51] A. van de Walle, G. Ceder, *Phys. Rev. B* **59**, 14992 (1999).

[52] E. J. Meijer, M. Sprik, *J. Chem. Phys.* **105**, 8684 (1996).

[53] P. Zische, S. Kurth, J. P. Perdew, *Comp. Mat. Science* **11**, 122 (1998).

[54] D. C. Patton, M. R. Pederson, *Phys. Rev. A* **56**, R2495 (1997).

[55] N. Kurita, H. Sekino, *Chem. Phys. Lett.* **348**, 139 (2001).

[56] E. Hult, Y. Andersson, B. I. Lundqvist, D. C. Langreth, *Phys. Rev. Lett.* **77**, 2029 (1996).

[57] E. Hult, H. Rydberg, B. I. Lundqvist, D. C. Langreth, *cond-mat/9805352 v1* (1998).

[58] J. P. Perdew, Y. Wang, *Phys. Rev. B* **45**, 13244 (1992).

[59] W. Kohn, *cit. at the conference ADFT2001, Vienna (Austria)* (2001).

[60] J. P. Perdew, M. Levy, *Phys. Rev. Lett.* **51**, 1884 (1983).

[61] L. J. Sham, M. Schlüter, *Phys. Rev. Lett.* **51**, 1888 (1983).

[62] R. O. Jones, O. Gunnarsson, *Rev. Mod. Phys.* **61**, 689 (1989).

[63] A. L. Fetter, H. D. Walecka, *Quantum Theory of Many-Particle Systems* (McGraw-Hill, 1971).

[64] L. Hedin, *Phys. Rev.* **139**, A796 (1965).

[65] L. Hedin, S. Lundquist, *Solid State Physics vol. 23* (Academic, New York, 1969).

[66] F. Aryasetiawan, O. Gunnarsson, *Rep. Prog. Phys.* **61**, 237 (1998).

[67] E. Runge, E. K. U. Gross, *Phys. Rev. Lett.* **52**, 997 (1984).

[68] I. V. Tokatly, O. Pankratov, *Phys. Rev. Lett.* **86**, 2078 (2001).

[69] R. W. Godby, M. Schlüter, L. J. Sham, *Phys. Rev. B* **37**, 10159 (1988).

[70] J. C. Slater, *Phys. Rev.* **51**, 846 (1937).

[71] O. K. Andersen, *Phys. Rev. B* **12**, 3060 (1975).

[72] D. J. Singh, *Planewaves, Pseudopotentials and the LAPW Method* (Kluwer Academic Publishers, Boston/Dordrecht/London, 1994). ISBN 0–7923–9412–7.

[73] D. Singh, *Phys. Rev. B* **43**, 6388 (1991).

[74] E. Sjöstedt, L. Nordström, D. J. Singh, *Sol. State Comm.* **114**, 15 (2000).

[75] G. K. H. Madsen, P. Blaha, K. Schwarz, E. Sjöstedt, L. Nordström, *Phys. Rev. B* **64**, 195134 (2001).

[76] L. Sham, T. Rice, *Phys. Rev.* **144**, 708 (1966).

[77] H. Ehrenreich, M. H. Cohen, *Phys. Rev.* **115**, 786 (1959).

[78] P. Puschnig, *Excitonic Effects In Organic Semi-Conductors* (Shaker-Verlag Aachen, Germany, 2002).

[79] M. S. Hybertson, S. G. Louie, *Phys. Rev. B* **34**, 5390 (1986).

[80] Z. H. Levine, D. C. Allen, *Phys. Rev. Lett.* **63**, 1719 (1989).

[81] R. DelSole, R. Girlanda, *Phys. Rev. B* **48**, 11789 (1993).

[82] P. Puschnig, C. Ambrosch-Draxl, *Phys. Rev. B* **66**, 165105 (2002).

[83] P. Puschnig, *et al.*, *Synth. Met.* **116**, 327 (2001).

[84] D. W. J. Cruickshank, *Acta Cryst.* **10**, 504 (1957).

[85] R. Mason, *Acta Cryst.* **17**, 547 (1964).

[86] J. M. Robertson, V. C. Sinclair, J. Trotter, *Acta Cryst.* **14**, 697 (1961).

[87] R. B. Campbell, J. M. Robertson, J. Trotter, *Acta Cryst.* **14**, 705 (1961).

[88] M. Oehzelt, R. Resel, A. Nakayama, *Phys. Rev. B* **66**, 174104 (2002).

[89] M. Oehzelt, *et al.*, *High Pressure Research* **22**, 343 (2002).

[90] M. Oehzelt, *et al.*, *Synth. Met.* **137**, 879 (2003).

[91] M. Oehzelt, *et al.*, *J. Chem. Phys.* **119**, 1078 (2003).

[92] E. A. Silinsh, *Organic Molecular Crystals* (Springer-Verlag Berlin Heidelberg New York, Germany, 1980).

[93] F. Birch, *J. Geophys. Res.* **83**, 1257 (1978).

[94] W. Häfner, W. Kiefer, *J. Chem. Phys.* **86**, 4582 (1987).

[95] A. S. Davydov, *Theory of Molecular Excitons* (Plenum Press, New York, USA, 1971).

[96] J. L. Katz, S. A. Rice, S.-I. Choi, J. Jortner, *J. Chem. Phys.* **39**, 1683 (1963).

[97] R. Silbey, J. Jortner, S. A. Rice, M. T. Vala, *J. Chem. Phys.* **42**, 733 (1965).

[98] R. Silbey, J. Jortner, S. A. Rice, M. T. Vala, *J. Chem. Phys.* **43**, 2925 (1965).

[99] P. Puschnig, K. Hummer, C. Ambrosch-Draxl, *Phys. Rev. B* **67**, 235321 (2003).

[100] S. Wiederhorn, H. G. Drickamer, *J. Phys. Chem. Sol.* **9**, 330 (1959).

[101] M. Kobayashi, K. Mizuno, A. Matsui, *J. Phys. Soc. Jap.* **58**, 809 (1989).

[102] S. Arnold, W. B. Whitten, A. C. Damask, *J. Chem. Phys.* **61**, 5162 (1974).

[103] D. W. Schlosser, M. R. Philpott, *Chem. Phys.* **49**, 181 (1980).

[104] R. Sonnenschein, K. Syassen, A. Otto, *J. Chem. Phys.* **74**, 4315 (1981).

[105] G. Brocks, P. J. Kelly, R. Car, *SYM* **57**, 4243 (1993).

[106] K. Hummer, P. Puschnig, C. Ambrosch-Draxl, *Phys. Rev. B* **67**, 184105 (2003).

[107] N. Karl, *Synth. Met.* **133-134**, 649 (2003).

[108] N. Karl, J. Marktanner, *Mol. Crys. and Liq. Crys.* **355**, 149 (2001).

[109] Z. Rang, *et al.*, *Appl. Phys. Lett.* **79**, 2731 (2001).

[110] Y. C. Cheng, *et al.*, *J. Chem. Phys.* **118**, 3764 (2003).

[111] Y. Isono, E. Morikawa, M. Kotani, *Chem. Phys. Lett.* **125**, 344 (1986).

[112] A. Niko, F. Meghdadi, C. Ambrosch-Draxl, P. Vogl, G. Leising, *Synth. Met.* **76**, 177 (1996).

[113] C. Ambrosch-Draxl, P. Puschnig, R. Resel, G. Leising, *Synth. Met.* **101**, 673 (1999).

[114] P. Puschnig, C. Ambrosch-Draxl, R. Resel, G. Leising, *Synth. Met.* **101**, 671 (1999).

[115] P. E. Blöchl, O. Jepsen, O. K. Andersen, *Phys. Rev. B* **49**, 16223 (1994).

[116] G. Heimel, *et al.*, *Mat.Res.Soc.Symp.Proc.* **665**, C5.8.1 (2001).

List of Figures

3.1 Partition of the unit cell into atomic spheres and interstitial region (hatched area) in the (L)APW method. 20

5.1 The anthracene (3A) molecule. The number of repeating phenyl rings is marked by n and equals 2, 3, 4, and 5, for naphthalene, anthracene, tetracene, and pentacene, respectively. 32
5.2 The projections of the anthracene crystal on the (ab)-plane (left) and the (ac)-plane (right) illustrate the herringbone stacking and the layered structure, respectively. The crystalline lattice constants are denoted by a, b, and c. 33
5.3 Three views of the crystal structure of anthracene illustrating the definition of the herringbone angle θ (left), the tilting angle χ, and δ (right), which served as the structure parameters for the internal geometry optimization. The crystalline axes are denoted with a, b, and c, respectively. 35
5.4 Variation of the herringbone angle in a window from 0 to 180 degrees. The sketches in the left and right corner illustrate the molecular arrangement in the (ab) plane, if θ equals 180 (left) and 0 (right) degrees, respectively. 36

6.1 FP-APW+lo results (full lines with filled symbols): the angles θ, χ and δ are compared to the values refined from experiment (dashed lines with open symbols) [88] as a function of pressure. 40
6.2 Total LDA energy as a function of δ calculated for monoclinic unit cells with c=11.162 Å (left), c=12.162 Å (middle), and c=13.162 Å (right panel), respectively. 41
6.3 The shortest intermolecular distances between end-hydrogen atoms and C (d_{CH}, triangles), respectively H atoms (d_{CH}, circles), as well as the largest CC (dashed line) and CH (full line) bond lengths as a function of pressure. 42

6.4 The pressure as a function of volume calculated by a fit (Eq. (6.2)) of the theoretical data set (full line) and the experimental data set (dashed line, Tab. 5.2) is shown in the left panel. In the right panel the isothermal bulk modulus versus volume for these two data sets resulting from the fit function is plotted. In the inset the focus is put on the region at the true equilibrium volume ($V_{exp} = 475.35$ Å^3). V_0^{LDA} marks the LDA equilibrium volume. 44
6.5 The calculated relative GGA energies [Ry] as a function of the unit cell volume [Å^3]. The full symbols denote the pressure data, whereas the open symbols correspond to hypothetical structures with a unit cell volume increased by 4, 7, 14, and 24%, respectively, obtained by extrapolating the lattice parameters as well as the angles θ, χ, and δ. The arrows indicate the LDA and the experimental equilibrium volume. 46
6.6 $\mathbf{k}$-path used for the band structure calculations of anthracene under pressure. The internal coordinates of these points Γ, Y, Z, A, B, and K in units of ($\frac{2\pi}{a}$, $\frac{2\pi}{b}$, $\frac{2\pi}{c}$) are (0,0,0), (0.5,0,0), (0,0,0.5), (0.5,0.5,0), (0,0.5,0), and (0.4,0,0.2), respectively. 48
6.7 Band structure E($\mathbf{k}$) (left) and DOS (right) of anthracene at ambient pressure and 1.1 GPa, respectively. In each case the Fermi level is indicated by a dashed line. 49
6.8 Band structure E($\mathbf{k}$) (left) and DOS (right) of anthracene at 2.5 and 4.0 GPa, respectively. In each case the Fermi level is indicated by a dashed line. 50
6.9 Band structure E($\mathbf{k}$) (left) and DOS (right) of anthracene at 6.1 and 10.2 GPa, respectively. In each case the Fermi level is indicated by a dashed line. 51
6.10 Band splitting of the highest VB (dots) and the lowest CB (diamonds) evaluated at Γ (left) and Z (right) as a function of pressure. 52
6.11 Band widths of CB_1, VB_1, and VB_2 evaluated in the directions $\overline{\Gamma Y}$, $\overline{\Gamma B}$, $\overline{\Gamma Z}$, and $\overline{\Gamma K}$ as a function of pressure. 53
6.12 Plot of the uncorrected LDA band gap $E_{\mathrm{g}}^{\mathrm{LDA}}$ of anthracene deduced from the band structure as a function of pressure. 56
6.13 The LDA 2D electron density plots of CB_1, VB_1, and VB_2 in the (ab)-plane calculated as sum over 40 $\mathbf{k}$-points along $\overline{\Gamma \mathrm{K} \mathrm{Z}}$ for different z-coordinates in units of c at ambient pressure and 10.2 GPa, respectively. The thin solid lines indicate the molecules to illustrate the herringbone arrangement in anthracene. The dark regions correspond to high density and vice versa. 57

6.14 GGA 2D electron density plots of CB_1, VB_1, and VB_2 in the (ab)-plane calculated as sum over 40 $\mathbf{k}$-points along $\overline{\Gamma\mathrm{KZ}}$ for different z-coordinates in units of c at ambient pressure and 10.2 GPa, respectively. The thin solid lines indicate the molecules to illustrate the herringbone stacking in anthracene. The dark regions correspond to high density and vice versa. 59
6.15 Imaginary part of the dielectric tensor computed at several pressure values up to 10.2 GPa separated in y-polarized (top panel) and z-polarized response (bottom panel). The self-energy correction Δ_c has been omitted. A life-time broadening of 0.1 eV has been included to smoothen the spectra. 61
6.16 y-component (left panels) and z-component (right panels) of the imaginary part of the dielectric tensor as a function of pressure calculated using the RPA (upper panels) compared to the solution of the BSE (lower panels). All optical absorption spectra have been corrected by the self-energy correction given in Tab. 6.7. A life-time broadening of 0.1 eV has been included. The arrows at 3.1 eV indicate the optical gap at ambient pressure. . . 63
6.17 The spin singlet exciton binding energy (left panel) and the major component of the dielectric screening (right panel) as a function of pressure. 64
6.18 The 2D electron distribution $|\psi_{c\mathbf{k}}(\mathbf{r}_e)|$ with respect to the hole at a fixed position (dark cross) calculated at ambient pressure for S (left panels) and FE (right panels), respectively. The unit cell is indicated by dashed rectangles, the molecules therein by thin solid lines. These (ab)- [(ac)-] maps represent slides at $z = 0.3$ [$y = 0.3$] with the hole located at $z = 0$ [$y = 0$] in units of c [b]. The dark regions correspond to high density. 68
6.19 Analogous to Fig. 6.18, but evaluated at 10.2 GPa. 69

7.1 The $\mathbf{k}$-path used for the band structure calculations of 2A, 3A, 4A, and 5A. The coordinates of the high symmetry points Γ, Y, Z, A, B, C, D, and E in units of $(2\pi/a,\ 2\pi/b,\ 2\pi/c)$ are (0,0,0), (0.5,0,0), (0,0,0.5), (0.5,0.5,0), (0,0.5,0), (0,0.5,-0.5), (0.5,0.5,-0.5), and (0.5,0,-0.5), respectively. The point K in 2A and 3A corresponds to (0.4,0,0.2). In case of pentacene the coordinates of E and K are (0.5,0.01,-0.53) and (0.47,0.01,0.14). . . . 72
7.2 The band structures E($\mathbf{k}$) of the monoclinic 2A and 3A. The coordinates of the high symmetry points are specified in Fig. 7.1. The Fermi level is indicated by the dashed line. 73
7.3 The band structures E($\mathbf{k}$) of the triclinic systems 4A and 5A. The coordinates of the high symmetry points are specified in Fig. 7.1. The Fermi level is indicated by the dashed line. 74

7.4 The band splitting of the highest occupied VB (left) and the lowest unoccupied CB (right) at high symmetry points in the IBZ as a function of the oligomer length. 75
7.5 The band widths of CB_1, VB_1, and VB_2 evaluated in high symmetry directions as a function of oligomer length. Note that $\overline{\Gamma Y}$ ($\overline{\Gamma B}$) is parallel to the crystalline a-axis (b-axis), and $\overline{\Gamma Z}$ corresponds to the c-direction, which is approximately the long molecular axis. 76
7.6 The GGA energy gap E_g^{GGA} compared to data available in literature [92, 111] as a function of the oligomer length n (left) as well as a function of the inverse oligomer length $1/n$ (right). 77
7.7 y-component (left panels) and z-component (right panels) of the imaginary part of the dielectric tensor calculated using the RPA (upper panels) compared to the solution of the BSE (lower panels) for 2A, 3A, 4A, and 5A. A life-time broadening of 0.1 eV has been included. 78
7.8 RPA peak position of $Im\ \varepsilon_{yy}$ and $Im\ \varepsilon_{zz}$ as a function of $1/n$, respectively. 80

A.1 Pentacene: The Cartesian diagonal elements of the imaginary part of the dielectric tensor and their transformations into the components along the crystalline axes. 95

B.1 The b-component of the imaginary part of the dielectric function at 0, 2.45, 4, and 10.2 GPa calculated on a grid of 64 $\mathbf{k}$-points (dashed line) and 413 $\mathbf{k}$-points (solid line), respectively. A life-time broadening of 0.1 eV has been included. 98
B.2 Analogous to Fig. B.1, but the c-component is shown. 98
B.3 The b-component of the imaginary part of the dielectric function at ambient pressure. The effective e-h Hamiltonian has been set up using 4, 8, 12, and 14 valence and the same number of conduction bands, respectively. A life-time broadening of 0.1 eV has been included. 99
B.4 The $Im\ \varepsilon_{bb}$ at ambient pressure. The results obtained by Eqs. (4.11), (4.12), and (4.13) for the screened Coulomb interaction are compared. A life-time broadening of 0.1 eV has been taken into account. 100

C.1 The fit equation p = 53.58-51717.6/V+12472700/V^2 (dashed line) of the PF data set (open circles) used for the re-evaluation of the pressure corresponding to the unit cell volume obtained by the experiments at DESY (cross). 102

C.2 The experimentally observed lattice parameters of anthracene as a function of volume (symbols) and the corresponding fits (dashed line). 103
C.3 The experimentally observed angles θ, χ, and δ of anthracene as a function of volume [88] (symbols) and the corresponding fit (dashed line). In addition, the calculated GGA values (open symbols) obtained from the internal geometry optimization described in Sec. 5.2. 104

List of Tables

5.1 Lattice parameters of the oligo-acenes: Naphthalene (2A) [84], anthracene (3A) [85], tetracene (4A) [86], and pentacene (5A) [87]. 34
5.2 Monoclinic lattice parameters a, b, c, β and the unit cell volume $V = a \cdot b \cdot c \cdot \sin\beta$ of anthracene as a function of pressure p. At ambient pressure the values have been taken from Ref. [85], the pressure data are from Ref. [88]. 35

6.1 Calculated angles θ, χ, and δ in degrees as a function of pressure p. The lattice parameters as summarized in 5.1.2 served as input parameters for these calculations. 40
6.2 Calculated angles θ, χ, and δ in degrees as a function of pressure p. The underlying lattice parameters up to 4 GPa originate from a different experimental data set as explained in Sec. C.1. . 43
6.3 Calculated band widths [meV] of the bands close to the Fermi level (CB_1, VB_1, and VB_2) analyzed in the directions $\overline{\Gamma\mathrm{Y}}$, $\overline{\Gamma\mathrm{B}}$, $\overline{\Gamma\mathrm{Z}}$, and $\overline{\Gamma\mathrm{K}}$ as a function of pressure [GPa]. 53
6.4 The uncorrected LDA band gap $E_{\mathrm{g}}^{\mathrm{LDA}}$ of anthracene extracted from the band structure as a function of pressure. 55
6.5 y-polarized response: The peak positions (maxima) of the RPA result, the spin singlet (S), and triplet (T) e-h pair, as well as the spin singlet (triplet) exciton binding energy SBE (TBE) and the singlet-triplet (S-T) splitting as a function of pressure. 64
6.6 z-polarized response: Analogous to Tab. 6.5, but only the peak positions and the splitting between FE and T (FE-T) are listed. . 65
6.7 Calculated and experimentally observed optical energy gaps, Δ_{g} and $\Delta_{\mathrm{g}}^{\mathrm{exp}}$ [101], respectively, the resulting self-energy correction Δ_{c}, and the ratio between Δ_{g} and $\Delta_{\mathrm{g}}^{\mathrm{exp}}$ as a function of pressure. 66

7.1 The total band dispersion of 2A, 3A, 4A, and 5A for CB_1, VB_1, and VB_2. 74
7.2 The ab-initio energy gaps $E_{\mathrm{g}}^{\mathrm{GGA}}$ of 2A, 3A, 4A, and 5A compared to experimentally observed values [92, 111]. 76

7.3 y- and z-polarized response of crystalline 2A, 3A, 4A, and 5A: The peak positions (maxima) of the RPA result, the position of spin singlet (S), and triplet (T) e-h pair, as well as the spin singlet (triplet) exciton binding energy SBE (TBE) and the singlet-triplet (S-T) splitting as a function of the oligomer length. Experimental data concerning the lowest transitions in these material have been taken from Ref. [92] to determine the experimental SBE, TBE and the S-T included for comparison. Note that none of the calculated spectra has been scissors corrected. 79

A.1 **WIEN2k** specific parameters for the oligo-acenes: naphthalene, anthracene, tetracene, and pentacene. R_{MT}, $R_{\mathrm{MT}}K_{\max}$, and $G_{\max}$ denote the muffin tin radius, the plane wave cut off, and the energy cut off for the Fourier expansion of the potential and the charge density, respectively. 92

C.1 Anthracene lattice parameters a, b, c, β, the unit cell volume $V = a \cdot b \cdot c \cdot \sin\beta$, and the three angles, respectively, of the expanded structures obtained by fitting the experimental data from Ref. [88]. These angles have been used as initial guess for the internal structure optimization with the GGA. 103

List of Publications

The publications summarized below, emerged from the work during my PhD studies. They are all related to the high pressure studies on the structural, electronic and optical properties of anthracene.

[P–1] G. Heimel, E. Zojer, R. Resel, P. Puschnig, K. Weinmeier, and C. Ambrosch-Draxl, "Structural Properties of Conjugated Molecular Crystals under High Pressure", *Mat. Res. Soc. Symp. Proc.* **665** (2001)

[P–2] K. Weinmeier, P. Puschnig, C. Ambrosch-Draxl, G. Heimel, E. Zojer, and R. Resel "High Pressure Studies of Polyaromatic Molecular Crystals: Optical and Electronic Properties from First Principles", *Mat. Res. Soc. Symp. Proc.* **665** (2001)

[P–3] P. Puschnig, G. Heimel, K. Weinmeier, R. Resel, and C. Ambrosch-Draxl, "High Pressure Studies on the Optical and Electronic Properties of para-Terphenyl", *High Pressure Research* **22**,105-109 (2002)

[P–4] M. Oehzelt, K. Weinmeier, G. Heimel, P. Puschnig, R. Resel, Ambrosch-Draxl, F. Porsch, and A. Nakayama, "Structural Properties of Anthracene under High Pressure", *High Pressure Research* **22**, 343-347 (2002)

[P–5] M. Oehzelt, R. Resel, K. Hummer, P. Puschnig, C. Ambrosch-Draxl, and A. Nakayama, "X-ray diffraction study of anthracene under high pressure", *Synth. Met.* **137**, 879 (2003)

[P–6] K. Hummer, P. Puschnig, C. Ambrosch-Draxl, M. Oehzelt, G. Heimel, and R. Resel, "Calculated Optical Absorption of Anthracene under High Pressure" *Synth. Met.* **137**, 935 (2003)

[P–7] K. Hummer, P. Puschnig, and C. Ambrosch-Draxl, "Ab-initio study of anthracene under high pressure", *Phys. Rev. B* **67**, 184105 (2003)

[P–8] P. Puschnig, K. Hummer, C. Ambrosch-Draxl, G. Heimel, M. Oehzelt, and R. Resel, "Electronic, optical and structural properties of oligo-phenylene molecular crystals under high pressure: an ab-initio investigation", *Phys. Rev. B* **67**, 235321 (2003)

[P–9] G. Heimel, P. Puschnig, M. Oehzelt, K. Hummer, B. Koppelhuber-Bitschnau, F. Porsch, C. Ambrosch-Draxl, and R. Resel, ”Chain length dependent intermolecular packing in polyphenylenes: A high pressure study”, *J. Phys.: Cond. Mat.* **15**, 3375 (2003)

[P–10] M. Oehzelt, G. Heimel, R. Resel, P. Puschnig, K. Hummer, C. Ambrosch-Draxl, K. Takemura, and A. Nakayama, ”High Pressure X-ray Study on Anthracene”, *J. Chem. Phys.* **119**, 1078 (2003)

[P–11] K. Hummer, P. Puschnig, and C. Ambrosch-Draxl, ”Excitonic Effects in Anthracene under High Pressure from First Principles”, *Phys. Scripta A* (2003) (in print)

[P–12] K. Hummer, P. Puschnig, and C. Ambrosch-Draxl, ”On the Lowest Optical Excitations in Molecular Crystals: Bound Excitons versus Free Electron-Hole Pairs in Anthracene”, *Phys. Rev. Lett.* (2003) (submitted)